Applied Computational Electromagnetics Society Journal

December 2024
Vol. 39 No. 12
ISSN 1054-4887

The ACES Journal is abstracted in INSPEC, in Engineering Index, DTIC, Science Citation Index Expanded, the Research Alert, and to Current Contents/Engineering, Computing & Technology.

The illustrations on the front cover have been obtained from the ARC research group at the Department of Electrical Engineering, Colorado School of Mines

Published, sold and distributed by: River Publishers, Alsbjergvej 10, 9260 Gistrup, Denmark

DECEMBER 2024 REVIEWERS

Kent Chamberlin
Peiyao Chen
Vinh Dang
Tanmaya Kumar Das
Jogesh Chandra Dash
Dileepan Dhanasekaran
Tijana Dimitrijevic
Valiyollah Ghazanfari
Alfredo Gomes Neto
Bernhard J. Hoenders
Taha Imeci
Pankaj Jha
Lihua Li
Gang Liu
Durga Prasad Mishra
Maria Evelina Mognaschi
Michel M. Ney
Antonio Orlandi
Andrew Peterson
Bojana Petkovic
S. Ramesh
Avisankar Roy
Giovanni Maria Sardi
Manthan Shah
Rakesh Sinha
Wei-Chung Weng

THE APPLIED COMPUTATIONAL ELECTROMAGNETICS SOCIETY JOURNAL

Vol. 39 No. 12 December 2024

TABLE OF CONTENTS

Circularly Polarized Plane Wave Source Implementation in Time-domain Electromagnetic Simulations

Jake W. Liu

Graduate Institute of Photonics and Optoelectronics
National Taiwan University, Taipei 10617, Taiwan
jwliu@ntu.edu.tw

Abstract **–** A unified framework for implementing circularly polarized plane wave sources in time-domain electromagnetic simulations is presented. Unlike traditional approaches that require separate settings for the orthogonal components as different sources, our method integrates circular polarization states represented in frequency domain seamlessly into time-domain simulations. We also studied the effectiveness of the approach when broadband sources are used. This framework is applicable to both finite-difference time-domain (FDTD) and pseudospectral time-domain (PSTD) methods.

Index Terms **–** Circular polarization, finite-difference time-domain (FDTD), pseudospectral time-domain (PSTD).

I. INTRODUCTION

Electromagnetic (EM) wave propagation is a fundamental aspect of numerous scientific and engineering applications, including optical device design, wireless communication, antenna design, metasurfaces and nanomaterials [1–9]. A critical feature of these waves is their polarization, which significantly affects their interaction with materials, their propagation characteristics, and their performance in various applications. As compared to linear polarization, circular polarizations are also important due to their unique properties and practical advantages. However, despite their significance, the documentation and detailed methodologies for implementing circular polarization in time-domain EM simulations, such as the finite-difference time-domain (FDTD) method and the pseudospectral time-domain (PSTD) method, remain sparse [10–14].

The FDTD method, a widely used numerical technique for solving Maxwell's equations in the time-domain, is a powerful tool for simulating complex EM phenomena. However, incorporating circular polarization into these time-domain simulations poses specific challenges. These include accurately representing the phase relationships and amplitude ratios of the orthogonal components of the electric field, ensuring numerical stability, and maintaining computational efficiency. While there is extensive literature on the general application of FDTD, there is a noticeable gap when it comes to practical, detailed guidance on simulating circularly polarized waves.

Modeling circular polarization accurately in EM simulations is crucial for several reasons. Firstly, these polarization states are often used in modern communication systems, where they can enhance signal quality and reduce interference [3]. Secondly, in remote sensing and radar applications, the ability to accurately simulate these polarizations can improve the detection and characterization of various targets and materials [2]. Lastly, in antenna design, understanding the behavior of circularly and elliptically polarized waves can lead to more efficient and effective antenna configurations [4–6].

This paper aims to address the gap in the current literature by providing a comprehensive methodology for implementing circular polarization in time-domain simulations using the collocated Fourier PSTD method, particularly with the introduction of plane wave sources by the total-field scattered-field (TFSF) formulation. The proposed method aims to achieve accuracy within 1% error when comparing the average radius of the electric field intensity to the reference radius. The reason we chose Fourier PSTD over FDTD is in its collocated grid-nature in field calculation, which is much easier for us to verify our results. However, the proposed method is applicable for both FDTD and PSTD simulations. We will explore the theoretical foundations of these polarization states, detail the numerical implementation steps, and validate the approach through various simulations.

II. THEORETICAL BACKGROUND

In this section, we first confine our study to monochromatic EM waves, as circular polarizations are predominantly represented and analyzed in the frequency domain. This focus allows us to leverage the well-established theoretical frameworks and mathematical representations of polarization states for single-frequency waves. A subsequent framework is developed in the next section to seamlessly incorporate the frequency-domain representation into time-domain

Submitted On: September 21, 2024
Accepted On: December 18, 2024

https://doi.org/10.13052/2024.ACES.J.391201

simulation, and further discussion on expanding the method to broadband sources are also discussed.

Polarization describes the orientation of the electric field vector of an EM wave as it propagates through space. It is a fundamental property that significantly influences the wave's interaction with materials, reflection and transmission characteristics, and reception by antennas. The three primary types of polarization are linear, circular, and elliptical:

(1) **Linear polarization**: The electric field vector maintains a constant direction as the wave propagates.

(2) **Circular polarization**: The electric field vector rotates in a circular motion, making one complete revolution per wavelength. It can be right-hand circularly polarized (RHCP) or left-hand circularly polarized (LHCP), depending on the rotation direction and also the definition. Suppose we have a wave propagating in the z-direction, the phasor representation of a circular polarized electric field at a fix point can be represented by:

$$\mathrm{E}(t) = \Re(E_0 e^{i\omega t}\widehat{\mathrm{x}} \pm E_0 i e^{i\omega t}\widehat{\mathrm{y}}), \tag{1}$$

where $\Re(\cdot)$ denotes taking the real part of its argument, E_0 denotes the amplitude of the electric field, ω being the angular frequency, and $\widehat{\mathrm{x}}$ and $\widehat{\mathrm{y}}$ are orthogonal unit vectors. By further calculations, (1) can be written in a pure time-domain representation as:

$$\mathrm{E}(t) = E_0\cos(\omega t)\,\widehat{\mathrm{x}} \pm E_0\cos(\omega t - \pi/2)\,\widehat{\mathrm{y}}. \tag{2}$$

Here the same wave function (cosines) is used for both $\widehat{\mathrm{x}}$ and $\widehat{\mathrm{y}}$ components. This is better for understanding time-domain implementations, since a single pre-defined waveform can be employed for both orthogonal components of the fields by properly introducing a time delay.

(3) **Elliptical polarization**: This can be viewed as a generalization of circular polarization where the electric field vector traces an ellipse. It is characterized by the ellipticity (ratio of the minor axis to the major axis) and the orientation angle of the ellipse. The mathematical representation of an elliptically polarized wave is:

$$\mathrm{E}(t) = E_{0x}\cos(\omega t + \delta_x)\,\widehat{\mathrm{x}} \pm E_{0y}\cos(\omega t + \delta_y)\,\widehat{\mathrm{y}}. \tag{3}$$

Comparing with circular polarizations, two things can be observed from the formulation: (i) the amplitudes can be different in $\widehat{\mathrm{x}}$ and $\widehat{\mathrm{y}}$ components and (ii) the phase delays (or advances) $\delta_x, \delta_y \in \mathbb{R}$ do not need to have a difference of $\pi/2$.

The polarization state of an EM wave can be represented using Jones vectors or Stokes parameters. For simplicity, we focus on Jones vectors in this paper. A Jones vector is a column vector that represents the amplitude and phase of the orthogonal components of the electric field. For an elliptically polarized wave, the Jones vector is represented by:

$$\mathrm{J} = \begin{pmatrix} E_{0x}e^{i\delta_x} \\ E_{0y}e^{i\delta_y} \end{pmatrix}. \tag{4}$$

In our implementation, by specifying the two orthogonal components of the electric field, representation similar to the Jones vector can be utilized to introduce the circularly polarized plane wave sources.

III. METHOD

In this section, the detailed method of implementing circular polarizations in time-domain simulations is outlined. Extending the method to the application of broadband sources is also discussed. It is noted that the method mentioned above is not restricted to the TFSF formulation; it is also applicable to the pure scattered field (SF) formulation if only the scattered field from the circularly polarized plane wave is of interest.

A. Circularly polarized plane wave implementation

In this section, the aim is to develop a framework that incorporates Jones vector representations, as shown in (4), into time-domain simulations without the need to set up two sources. Following the TFSF settings, the first step is to define the incident angles of the plane wave, followed by the field strength. Traditionally, the fields are real-valued. However, we aim to set them as complex-valued. Specifically, the far-field incident electric field in spherical coordinate system takes the general complex form of:

$$\begin{cases} E_\theta = E_{0\theta}e^{i\delta_\theta} \\ E_\phi = E_{0\phi}e^{i\delta_\phi} \end{cases}, \tag{5}$$

where $E_{0\theta},\ E_{0\phi}, \delta_\theta, \delta_\phi \in \mathbb{R}$. One can easily transform this into the x-y-z components by the following:

$$\begin{cases} E_x = \cos\theta_i\,\cos\phi_i\,E_\theta - \sin\phi_i\,E_\phi \\ E_y = \cos\theta_i\,\sin\phi_i\,E_\theta + \cos\phi_i\,E_\phi \\ E_z = -\sin\theta_i\,E_\theta \end{cases}, \tag{6}$$

where θ_i and ϕ_i are the incident angles in spherical coordinate system. Similar relationship for the magnetic field components can be acquired accordingly.

Note that the values in (5) are now complex-valued and thus are not directly applicable in time-domain simulations. A certain adaptation similar to (2) needs to be constructed in order to seamlessly incorporate the definitions in (4) into time-domain simulations. The key lies in the time-shifting properties of the Fourier transform: $g(t - t')$ corresponds to $e^{-i2\pi f t'}G(f)$. The additional phase factor $e^{-i2\pi f t'}$ in frequency domain represents a time shift t' in the time-domain.

For each complex field value F_η, where $F \in E, H$ and $\eta \in x, y, z$, a set of preliminary amplitude $A(F_\eta)$ and time delay $\Delta(F_\eta)$ can be derived by the following:

$$\begin{cases} A(F_\eta) = \text{abs}(F_\eta) \\ \Delta(F_\eta) = \text{ang}(F_\eta)/2\pi f_c \end{cases}, \tag{7}$$

where abs$(\cdot)$ denotes the absolute operator and ang$(\cdot)$ computes the phase angle in radians in the interval $(-\pi, \pi]$. f_c is the frequency of the monochromatic wave.

If $\Delta(F_\eta) < 0$, then a flip in amplitude and a shift in time delay will be employed as a correction:

$$\begin{cases} A'(F_\eta) = -A(F_\eta) \\ \Delta'(F_\eta) = \Delta(F_\eta) + 1/2f_c \end{cases}. \tag{8}$$

Otherwise $A'(F_\eta) = A(F_\eta)$ and $\Delta'(F_\eta) = \Delta(F_\eta)$. The reason to employ this correction is to preserve the in-phase relationship between the orthogonal components of the E, H pair. Thus, the updating equation for the injected circularly polarized wave source can be represented by the following form:

$$F_\eta^{inc}(t) = A'(F_\eta) \cdot w[t - \Delta'(F_\eta)], \tag{9}$$

where $w(\cdot)$ represents the waveform function (for example, a ramped sine wave). By employing (9) in the time-marching loop, one can successfully create a circularly polarized plane wave in time-domain simulations, and assignment of the incident plane wave source takes the form as in (5).

B. Discussion on extension to broadband sources

The method described earlier utilizes a time shift between the two orthogonal components to create a circularly polarized monochromatic plane wave. Specifically, the waveform functions in (9) are typically sinusoidal. However, it is also of interest to extend this method to broadband sources, such as Gaussian or differential Gaussian pulses. It should be noted that the time shift $\Delta(F_\eta)$ introduced in (7) is dependent on a center frequency f_c. Consequently, if a broadband source is implemented, only the field at the center frequency will be circularly polarized. At frequencies other than the center frequency, the wave will be elliptically polarized. This can be demonstrated by the following analysis.

Consider a plane wave source with orthogonal components:

$$\text{J} = \begin{pmatrix} G(f) \\ G(f)e^{-i2\pi f t'} \end{pmatrix}, \tag{10}$$

where $G(f)$ is the Fourier transform of the time-domain waveform function. If the second component in (10) is time-shifted in the time-domain by an amount of $t' = 1/4f_c$, when $f = f_c$, (10) reduces to J $= (G(f),\ e^{-i\pi/2}\, G(f))$, which represents a circularly polarized source. However, at frequencies other than the center frequency, a factor of $e^{-i\pi f/2f_c}$ is introduced, causing the resulting wave to become elliptically polarized.

IV. NUMERICAL RESULTS

In the numerical examples, we choose the TFSF technique as our method to introduce plane wave sources, since it is easy to use the TFSF technique to study various wave propagation phenomena. However, the proposed method can also be implemented in pure SF formulation. The TFSF used for collocated Fourier PSTD contains certain modifications: a connected region between the TF region and SF region is required in order to eliminate the artifacts caused by the field abruptions [15].

The collocated field calculations in the PSTD formulation facilitate the verification of numerical results. The simulation uses a 51×51×51 grid, with a 10-cell thick convolutional perfectly matched layer (CPML) to eliminate unwanted waves leaking from the TFSF region (though the leakage is relatively small enough compared to the amplitude of the incident wave, below 0.1%). The TFSF connecting region has a thickness of 8 cells, as proposed in [15], and starts 10 cells away from the PML. The grid size is 50 nm in all three directions and the time step is set to 0.06 fs. The programs are written in Julia.

A. Circular polarization simulation of monochromatic waves

For the circular polarization simulation of the monochromatic wave, the center frequency is set to 600 THz, and a ramping sine function is defined as the following to serve as the waveform function used in (9):

$$w(t) = T(t)\sin(2\pi f_c t), \tag{11}$$

where $T(t)$ is a turn-on function. In our implementation, we use a shifted sigmoid function as the turn-on function for smooth transitions: $T(t) = 1/[1 + \exp(\frac{-t + l \cdot dt}{p \cdot dt})]$. l and p are parameters to determine the delay and width of the ramping and is set to 40 and 10 respectively in the simulation. The time difference dt in the simulation is 0.06 fs. The total time step is set to 400. The plane wave introduced by the TFSF method is set to propagate in the $+z$-direction (i.e. $(\theta_i,\ \phi_i) = (0,\ 0)$ towards the origin, in this case, setting in (6) reduces to $E_x = E_\theta$, $E_y = E_\phi$).

We first consider the case where J $= (1,\ e^{i\pi/2})$, meaning $E_x = 1$ and $E_y = i$. The initial step to verify that the plane wave is truly circularly polarized is to place a detector at the center of the simulation space and record the total squared field strength $E^2 = E_x^2 + E_y^2 + E_z^2$. The value should be constant (in this case, 1) once the steady state is reached. The result is shown in Fig. 1. Before reaching the steady state, certain jitters exist because the wave function (11) is not purely monochromatic. However, after 10 fs, when the steady state is achieved, the value remains constant.

We then plotted the Lissajous figure, which is a projected harmonic-motion trace, for time steps ranging from 201 to 250. The result is shown in Fig. 2. One can observe that the projected trace does fit on the unit circle, indicating that the plane wave is circularly polarized. We calculate the average electric field intensity over this time

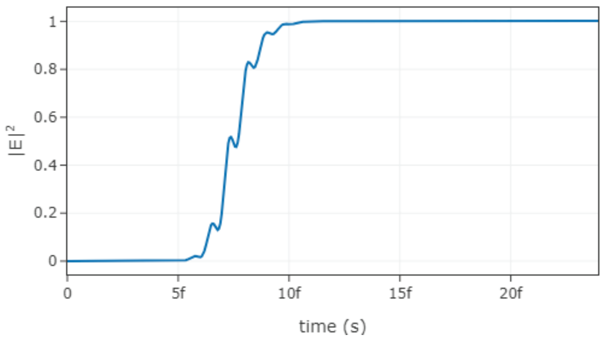

Fig. 1. Record of $E^2 = E_x^2 + E_y^2 + E_z^2$ at the center of the simulation space. This plot shows the time evolution of the squared electric field magnitude at the origin. Initially, the field magnitude is zero, indicating no electric field presence. As the simulation progresses, the electric field strength increases, exhibiting transient oscillations before stabilizing. After reaching the steady state (around 10 fs), the field magnitude remains constant at 1, confirming the successful generation of a circularly polarized plane wave. This verification step ensures that the wave retains its polarization characteristics throughout the simulation.

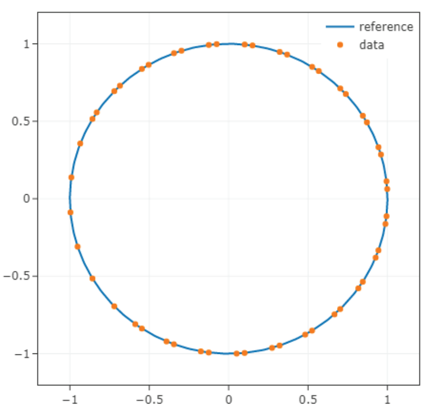

Fig. 2. Lissajous figure for time steps ranging from 201 to 250, showing the projected traces fitting perfectly on the unit circle, indicating that the plane wave is circularly polarized. The reference circle and data points demonstrate the accuracy of the simulation.

frame and obtain a value of 0.9978, indicating an error of less than 1% compared to the unity radius reference.

Finally, the 2D electric field at the center of the domain is plotted for time steps ranging from 201 to 250. For the case where the source is $\mathrm{J} = (1,\ e^{i\pi/2})$, the result is displayed in Fig. 3 (a). Additionally, we modeled the case with $\mathrm{J} = (1,\ e^{-i\pi/2})$, and the corresponding result is presented in Fig. 3 (b). As expected, the direction of polarization is reversed between these two cases, which confirms the expected behavior of the electric field under opposite phase shifts. The results clearly illustrate how the phase shift between the orthogonal components of the source influences the polarization direction of the resulting wave.

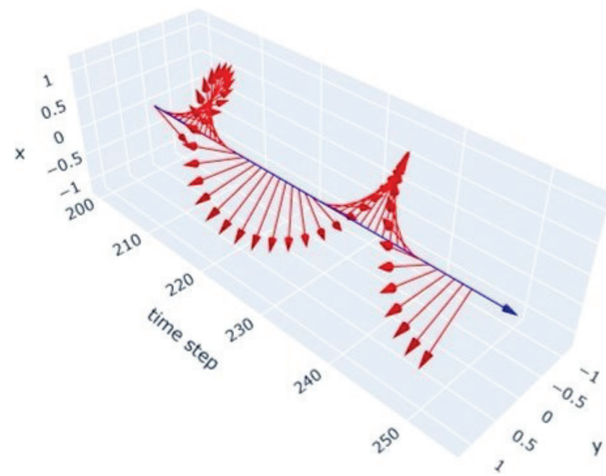

(a)

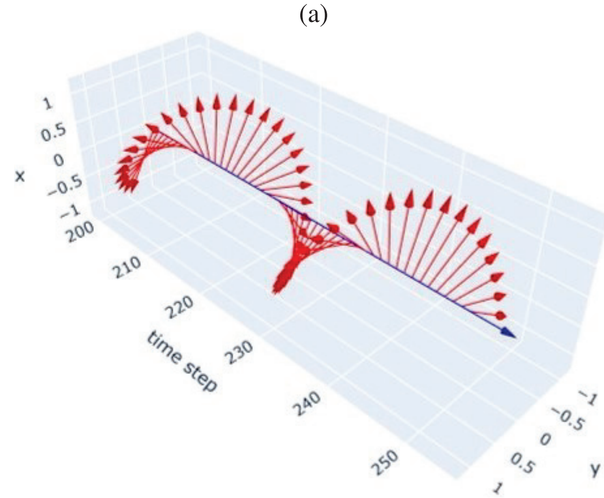

(b)

Fig. 3. 2D electric field at the center of the simulation space for time steps ranging from 80 to 120: (a) the case where the source is $\mathrm{J} = (1,\ e^{i\pi/2})$, showing the electric field rotating from the positive y-axis toward the positive x-axis and (b) the case where the source is $\mathrm{J} = (1,\ e^{-i\pi/2})$, with the electric field rotating from the negative y-axis toward the positive x-axis.

B. Broadband sources simulation

In the broadband simulation, a Gaussian pulse is used as the excitation:

$$w(t) = e^{-(t-t_0)^2/\tau^2}, \tag{12}$$

where $\tau = \sqrt{2.3}\,/\,2\pi f_c = 0.4022$ fs and $t_0 = 4.5\ \tau = 1.81$ fs.

Similar to Fig. 3, Fig. 4 shows the 2D electric field at the center of the simulation space for time steps ranging

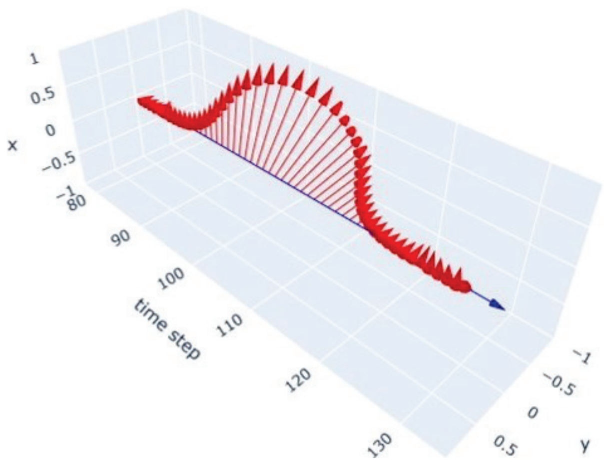

(a)

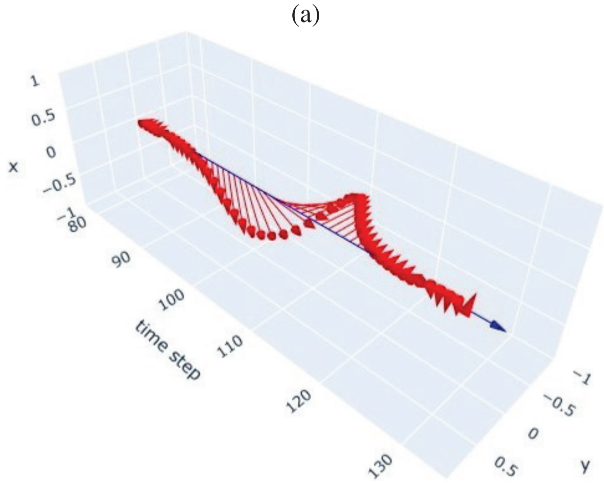

(b)

Fig. 4. 2D electric field simulation results for time steps ranging from 80 to 120: (a) simulation with J $= (1,\ e^{i\pi/2})$ showing the expected circular polarization and (b) simulation with J $= (1,\ e^{-i\pi/2})$ illustrating the reversed polarization direction. These results demonstrate the effectiveness of the TFSF technique in accurately modeling circularly polarized plane waves. The time evolution of the electric field is clearly depicted, highlighting the distinct polarization characteristics for each case.

from 80 to 120, for the cases where the source is J $=(1,\ e^{i\pi/2})$ and J $=(1,\ e^{-i\pi/2})$. It can be observed that the Gaussian pulse exhibits a twist in both cases, but in opposite directions. In Fig. 4 (a), the electric field rotates from the positive y-axis toward the positive x-axis, while in Fig. 4 (b), the electric field rotates from the negative y-axis toward the positive x-axis.

It is also of particular interest to compute the axial ratio (AR) as a function of frequency. In ideal circular polarization, AR is exactly 1, indicating equal amplitude components in orthogonal directions. An increase in AR represents a deviation towards elliptical polarization, which can affect signal quality in communication systems. In these systems, maintaining low AR values is essential for minimizing cross-polarization and ensuring consistent signal reception. A shift in AR from 1 to 1.5 (which is normally the threshold value) represents an increasingly elliptical polarization, which can lead to a mismatch between the transmitted and received signals and reduce the effective power transferred to the receiver.

In the second simulation, we retained the parameters of the Gaussian pulse as mentioned previously and tested various time shifts. The recorded electric field at the center is subjected to a discrete Fourier transform (DFT) across various frequencies, ranging from 300 THz to 800 THz with a spacing of 10 THz. After obtaining the frequency-domain field of the orthogonal components, AR is then calculated by dividing the length of the long axis a by the length of the short axis b, with:

$$a=\sqrt{\frac{E_{0x}^2+E_{0y}^2+\sqrt{\left(E_{0x}^2-E_{0y}^2\right)^2+4E_{0x}^2E_{0y}^2\cos^2\delta}}{2}}, \tag{13}$$

$$b=\sqrt{\frac{E_{0x}^2+E_{0y}^2-\sqrt{\left(E_{0x}^2-E_{0y}^2\right)^2+4E_{0x}^2E_{0y}^2\cos^2\delta}}{2}}, \tag{14}$$

where $\delta=\delta_x-\delta_y$. By retaining the parameters of the Gaussian pulse, center frequencies $f_c = 500,\ 600,\ 700$s THz are tested with J $=(1,\ e^{i\pi/2})$, and the results are shown in Fig. 5. It can be observed that at the center frequencies, the calculated AR values are equal to 1, indi-

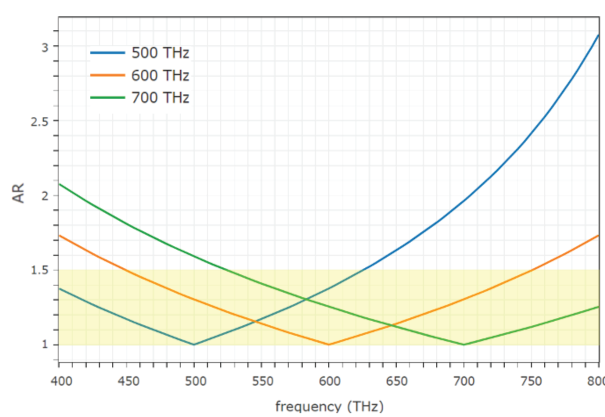

Fig. 5. Axial ratio (AR) as a function of frequency for Gaussian pulses with center frequencies $f_c = 500,\ 600,\ 700$ THz. AR is calculated using J $=(1,\ e^{i\pi/2})$. At the center frequencies, AR equals 1, indicating circular polarization. As the frequency deviates from the center, AR increases, demonstrating a transition to elliptical polarization. For $f_c = 600$ THz, AR remains below the threshold 1.5 over a total bandwidth of 300 THz.

cating that the waves are circularly polarized. AR values gradually increase and become elliptically polarized as the frequency moves away from the center frequency. For $f_c = 600$ THz, the total bandwidth where AR<1.5 is 300 THz.

It is important to note that AR curves for broadband sources are independent of the waveform function and are solely determined by the factor $e^{-i\pi f/2f_c}$, as analyzed in section 3B. The simulated results are consistent with the analytical predictions obtained using the Jones vector $\mathrm{J} = (1,\ e^{-i\pi f/2f_c})$.

V. CONCLUSION

In this study, we have developed a comprehensive method for incorporating circular polarizations into time-domain EM simulations using the Fourier PSTD method. Our simulations verified the accuracy and stability of the proposed approach, as evidenced by the consistent field strength and accurate Lissajous figures. In addition to monochromatic sources, we also tested our method to accommodate broadband sources, such as Gaussian pulses, and analyzed AR across a wide frequency range. Analysis of AR demonstrated that while circular polarization is maintained at the center frequency, the polarization gradually transitions to elliptical as the frequency deviates from the center. This result is consistent with the expected behavior based on the frequency-dependent phase shift. Future work includes extending the polarization analysis from wave propagation to scattering in both simple and complex structures.

REFERENCES

[1] Y. Lee, H. Kim, and C. Kim, "Rigorous optical modeling of circularly polarized light-emitting devices: Interaction of emitters with device geometries," *ACS Photonics*, vol. 10, no. 9, pp. 3283-3290, 2023.

[2] L. Yan, Y. Li, V. Chandrasekar, H. Mortimer, J. Peltoniemi, and Y. Lin, "General review of optical polarization remote sensing," *International Journal of Remote Sensing*, vol. 41, no. 13, pp. 4853-4864, 2020.

[3] B. Y. Toh, R. Cahill, and V. F. Fusco, "Understanding and measuring circular polarization," *IEEE Transactions on Education*, vol. 46, no. 3, pp. 313-318, 2003.

[4] M. Sahal and V. Tiwari, "Review of circular polarization techniques for design of microstrip patch antenna," in *Proceedings of the International Conference on Recent Cognizance in Wireless Communication & Image Processing: ICRCWIP-2014*, pp. 663-669, 2016.

[5] G. Bogdan, P. Bajurko, and Y. Yashchyshyn, "Time-modulated antenna array with dual-circular polarization," *IEEE Antennas and Wireless Propagation Letters*, vol. 19, no. 11, pp. 1872-1875, Nov. 2020.

[6] J. Feng, Z. Yan, S. Yang, F. Fan, T. Zhang, X. Liu, X. Zhao, and Q. Chen, "Reflect-transmit-array antenna with independent dual circularly polarized beam control," *IEEE Antennas and Wireless Propagation Letters*, vol. 22, no. 1, pp. 89-93, Jan. 2023.

[7] R. Dutta, J. Ghosh, Z. Yang, and X. Zhang, "Multiband multi-functional metasurface-based reflective polarization converter for linear and circular polarizations," *IEEE Access*, vol. 9, pp. 152738-152748, 2021.

[8] N. Hussain, M.-J. Jeong, A. Abbas, T.-J. Kim, and N. Kim, "A metasurface-based low-profile wideband circularly polarized patch antenna for 5G millimeter-wave systems," *IEEE Access*, vol. 8, pp. 22127-22135, 2020.

[9] S. Jiang and N. A. Kotov. "Circular polarized light emission in chiral inorganic nanomaterials," *Advanced Materials,* vol. 35, no. 34, p. 2108431, 2023.

[10] A. Taflove and S. C. Hagness, *Computational Electrodynamics: The Finite-Difference Time-Domain Method*, 3rd ed. Norwood: Artech House, 2005.

[11] A. Taflove, A. Oskooi, and S. G. Johnson, *Advances in FDTD Computational Electrodynamics: Photonics and Nanotechnology*. Norwood: Artech House, 2013.

[12] Q. H. Liu, "The PSTD algorithm: A time-domain method requiring only two cells per wavelength," *Microwave and Optical Technology Letters*, vol. 15, no. 3, pp. 158-165, 1997.

[13] Q. H. Liu, "Large-scale simulations of electromagnetic and acoustic measurements using the pseudospectral time-domain (PSTD) algorithm," *IEEE Transactions on Geoscience and Remote Sensing*, vol. 37, no. 2, pp. 917-926, 1999.

[14] J. W. Liu, Y.-S. Hsu, and S. H. Tseng, "Extracting field information embedded within a coarse pseudospectral time-domain simulation," *IEEE Antennas and Wireless Propagation Letters*, vol. 17, no. 8, pp. 1488-1491, 2018.

[15] X. Gao, M. S. Mirotznik, and D. W. Prather, "A method for introducing soft sources in the PSTD algorithm," *IEEE Transactions on Antennas and Propagation*, vol. 52, no. 7, pp. 1665-1671, 2004.

Jake W. Liu was born in Hualien, Taiwan, in 1995. He received the B.S. degree in Electrical Engineering from National Taiwan University, Taipei, Taiwan, in 2017, and the Ph.D. degree from Graduate Institute of Communication Engineering in 2022. His research interests include antenna measurement theory, calibration of phased array of antennas at millimeter wave frequencies, and computational electromagnetics. He is currently conducting his postdoctoral research at the Graduate Institute of Photonics and Optoelectronics, National Taiwan University.

Outdoor Wi-Fi Dual-band Dual-polarized Base Station Antenna Design

Yida Fan[1], Lijuan Li[1,2], Ravi K. Arya[2], Xianghua Ma[3], Shiyuan Kong[2], and Junwei Dong[2]

[1]School of Optoelectronic Engineering
Changchun University of Science and Technology, Changchun, Jilin, 130022, China
FanYD_cust@outlook.com, custjuan@126.com

[2]Xiangshan Laboratory
Zhongshan Institute of Changchun University of Science and Technology, Zhongshan, Guangdong, 528437, China
custjuan@126.com, raviarya@cust.edu.cn, 184217177@qq.com, dongjunwei@163.com

[3]EMed Technology Co. Ltd
EMed Technology Co. Ltd, Zhongshan, Guangdong, 528437, China
18666980616@163.com

Abstract – In this manuscript, a dual-band and dual-polarized coupled patch array antenna operating at 2.45 GHz and 5.8 GHz for outdoor Wi-Fi applications is proposed. Two sets of antenna arrays made of four-element stacked patches act as main radiators. The height of this antenna is $0.04\lambda_0$, which is much smaller than the general size of other low-profile antennas. The arrays are fed by two feed ports which are used to separately feed vertical and horizontally polarized signals with stable port isolation. The antenna structure also employs a duplex filter to filter 2.4-2.484 GHz and 5.1-5.9 GHz operating band frequencies. The measured impedance bandwidths of the prototype antenna structure are 2.41-2.484 GHz and 5.1-5.9 GHz, respectively. The isolation between the two ports is greater than 20 dB, and the cross-polarization level is better than 20 dB in the operating bands. In addition, the average gain of the prototype antenna is approximately 13 dBi in horizontal and vertical polarization. Overall, because of the stable structure, high reliability, small size, and light weight of the patch antenna, the outdoor base station antenna has a huge potential market value, this antenna is a good candidate for commercial outdoor Wi-Fi applications.

Index Terms – Access point, antenna array, dual-band, dual-polarized patch antenna, low profile.

I. INTRODUCTION

With the popularity of 4G communication technology and the rise of 5G communication, Wi-Fi technology has been widely used. Wi-Fi is a superset of the IEEE 802.11 standards for communication of local area networked devices spanning over several tens of meters [1]. Commercial Wi-Fi antennas demand different features such as low cost, small size, easy manufacturability, and good performance. However, attaining all these features in a single antenna demands good engineering skills.

A dual-band dual-polarized antenna is a kind of antenna that has been widely used in base station communications in recent years. It can not only integrate the signal transmission capability of the two frequency bands into one structure for size reduction, but also has many advantages such as wide broadband, strong anti-interference ability, low power consumption, and great channel capacity, which are desired features for commercial Wi-Fi applications.

The main antenna structures used for dual polarization include cross dipole antenna, slot antenna, and patch antennas [2–6]. Cross-dipole antennas have high cross-isolation and good broadband performance. Still, the design of such antennas occupies more space, which is not conducive to the miniaturization of antennas [7–9]. The slot antenna, on the other hand, has the advantages of planar feed structure, wideband, and high isolation, but has poor cross-polarization properties [10–12].

Compared with the above antennas, the patch antenna has a small footprint, low cost, and can achieve wideband and better port isolation by stacking patch antennas [13, 14], so it is a good candidate as an array antenna element. For example, it is proposed [15] that the antenna realizes the dual-band dual-polarization antenna and has a high degree of isolation between ports.

The design of dual-polarized 4-unit array antenna with 1-4 power dividers provided in [6] and [10] serves as a reference for the antenna design. According to the standard of Wi-Fi frequency band, this manuscript designs a new low-profile dual-polarized coupled patch antenna unit and a low-passband stop filter, and realizes

Submitted On: April 24, 2024
Accepted On: December 4, 2024
https://doi.org/10.13052/2024.ACES.J.391202

the dual-frequency dual-polarized patch array antenna for outdoor Wi-Fi base stations. High isolation and low cross polarization are obtained in the operating frequency band. To validate the design model, a prototype antenna was fabricated and measured. The simplified block diagram of the antenna structure is shown in Fig. 1 where HF means high-frequency and LF means low-frequency. The antenna elements and arrays are discussed in detail below.

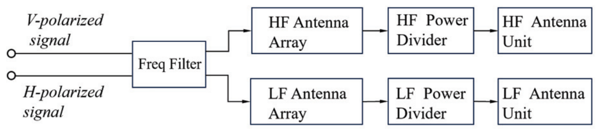

Fig. 1. Antenna structure block diagram.

II. DESIGN OF DUAL-POLARIZATION ANTENNA UNIT

The design of patch antenna must first determine the substrate material used and the operating frequency. According to the definition of Wi-Fi operating frequency band, this manuscript designs the patch antenna with operating frequency of 2.4-2.48 GHz and 5.1-5.8 GHz, respectively, using substrate materials with thickness of 0.74 mm, $\varepsilon_r = 2.45$, $\tan\delta = 0.001$. The length and width of the rectangular patch can be calculated by some numerical formulas:

$$W = \frac{c}{2f_0\sqrt{\frac{(\varepsilon_r+1)}{2}}}, \tag{1}$$

where c is the speed of light, ε_r is dielectric constant, f_0 is resonant frequency.

The effective dielectric constant (ε_{eff}) is calculated according to the substrate material height (h), dielectric constant (ε_r) and the calculated width (W) of the patch antenna:

$$\varepsilon_{eff} = \frac{\varepsilon_r+1}{2} + \frac{\varepsilon_r-1}{2}\left[1+12\frac{h}{W}\right]^{-\frac{1}{2}}. \tag{2}$$

The actual length of the patch antenna is calculated by (3):

$$L = \frac{c}{2f_0\sqrt{\varepsilon_{eff}}} - 0.824h\left(\frac{(\varepsilon_{eff}+0.3)\left(\frac{W}{h}+0.264\right)}{(\varepsilon_{eff}-0.258)\left(\frac{W}{h}+0.8\right)}\right). \tag{3}$$

The patch antenna works in dual polarization mode, its dimension is constrained to equal side length. Due to the small thickness of the substrate material, the upper layer element is used as a coupled antenna with a dimension of $0.36\lambda \times 0.36\lambda$ to expand the bandwidth of the antenna. Finally, through simulation and optimization, the following low-frequency antenna array structure is obtained.

Figure 2 shows the low-frequency antenna element of the proposed antenna. The low-frequency antenna element operates at a frequency of 2.41-2.484 GHz. The antenna primarily consists of two layers: upper and lower patches separated by a 5 mm gap. The upper patch measures 43.5 mm × 43.5 mm, while the lower patch measures 36.5 mm × 36.5 mm. Both patches are linked by a common support column, with foam material inserted between them to stabilize the antenna unit. The two feed ports of the antenna have a 90 ° angle so that port 1 inputs

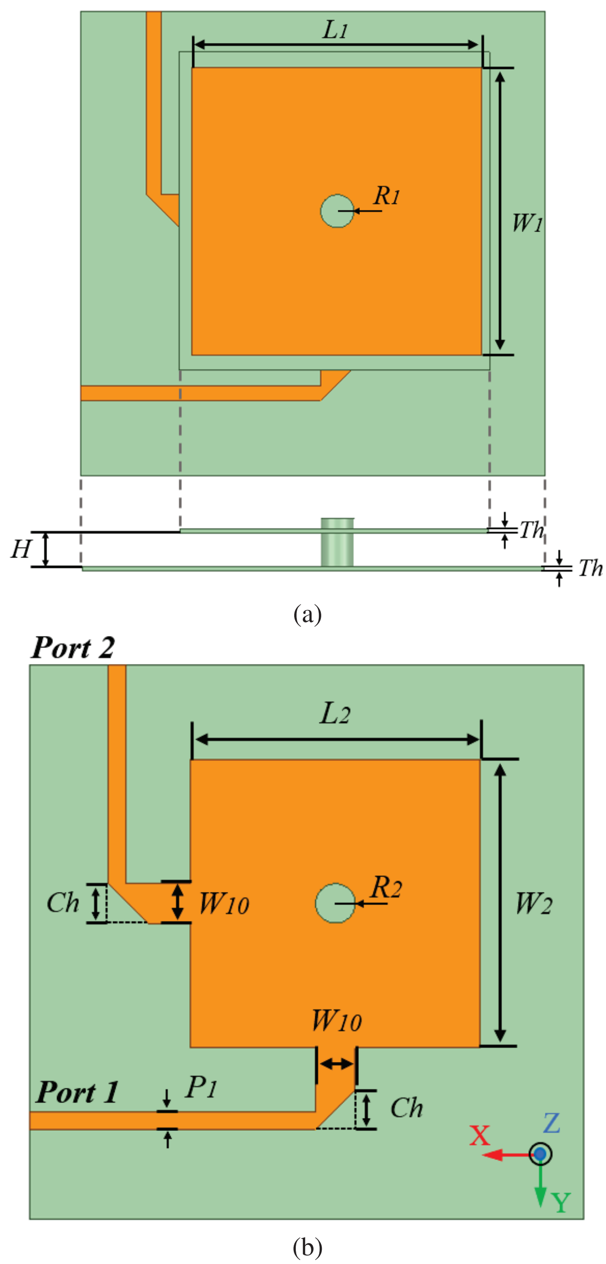

Fig. 2. Low-frequency antenna element: (a) top structure and (b) bottom structure.

a vertically polarized signal and port 2 inputs a horizontally polarized signal. The parameter values defined in Fig. 2 are as follows (unit: mm) : $L_1 = W_1 = 43.5$, $R_1 = R_2 = 1.2$, $P_1 = 2.2$, $W_{10} = 5$, $L_2 = W_2 = 36.5$, $Ch = 5$, $H = 5$, $Th = 0.74$.

All antenna simulations were conducted utilizing CST Studio Suite. Hexahedral meshing is applied to the antenna, and the number of meshing for each wavelength is adjusted so that the details in the structure are included. The performance of the antenna is simulated by using a time-domain solver Finite Integration Technique. In Fig. 3, the simulated S-parameter of the antenna element is depicted. The frequency range exhibiting a return loss exceeding 10 dB spans from 2.41 GHz to 2.484 GHz, satisfying the criteria for the low-frequency band. Moreover, the isolation between the two ports surpasses 25 dB.

Figure 4 shows the simulated co-planar polarization and cross-polarization of the low-frequency antenna element at the $\phi = 0°$ and $\phi = 90°$ cuts. These plots show that port 1 and port 2 have good cross-isolation.

According to equations (1) and (3), the basic size of the high frequency patch antenna can be calculated. The lower patch of the high-frequency antenna is arranged with inward-facing grooves for adjusting the feed position. The grooves can also expand the bandwidth and reduce the impedance mismatch through reasonable parameter optimization.

Figure 5 shows the high-frequency antenna element of the proposed design, operating within the frequency range of 5.1 GHz to 5.9 GHz. The overall size of the antenna is 52 mm × 52 mm, and the substrate is 0.74 mm thick. The antenna element consists of two layers of patches, the upper layer of patch antenna size is 19 mm × 19 mm while the lower base size is 16.83 mm × 17.325 mm, separated by a 2 mm gap. The coupled upper

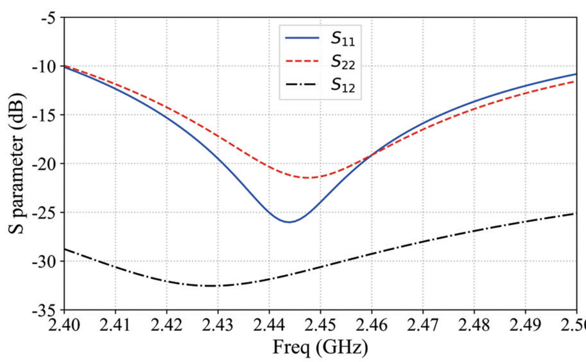

Fig. 3. Low-frequency antenna S-parameter.

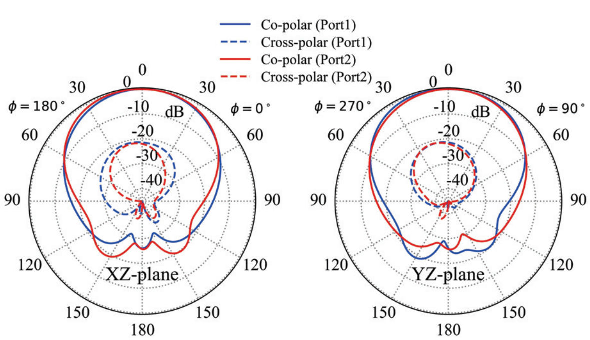

Fig. 4. Low-frequency antenna element radiation pattern at 2.45 GHz.

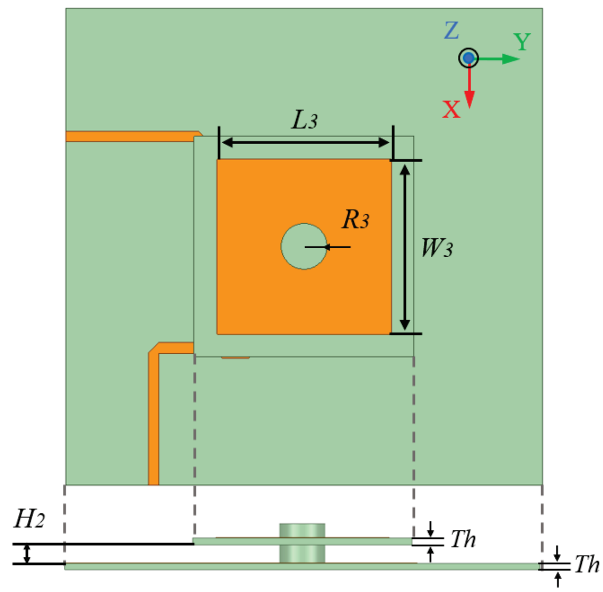

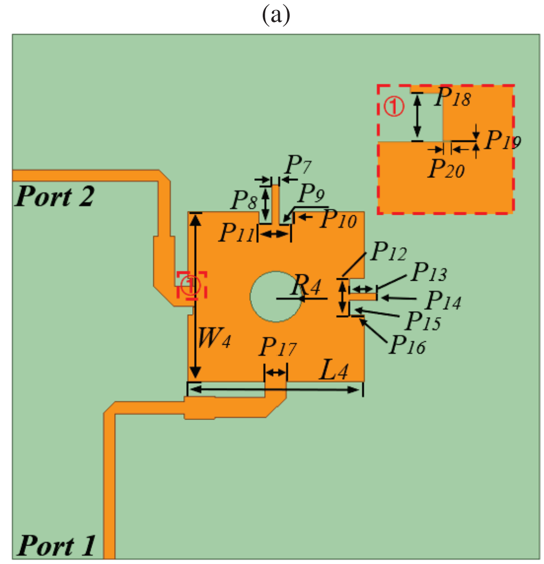

Fig. 5. High-frequency antenna unit: (a) top structure and (b) bottom structure.

and lower patches in this manner help to expand the bandwidth effectively. The parameter values defined in Fig. 5 are as follows (units: mm) :$L_3 = W_3 = 19$, $R_3 = R_4 = 1.2$, $H_2 = 2$, $Th = 0.74$, $W_4 = 16.83$, $L_4 = 17.325$, $P_7 = 0.63$, $P_8 = 3.876$, $P_9 = 1.2768$, $P_{10} = 1.224$, $P_{11} = 3.18$, $P_{12} = 3.57$, $P_{13} = 2.73$, $P_{14} = 0.612$, $P_{15} = 1.479$, $P_{16} = 1.4175$, $P_{17} = 2$, $P_{18} = 0.78$, $P_{19} = 0.02$, $P_{20} = 0.1168$.

Figure 6 shows the simulated S-parameter of the antenna element. The return loss of the antenna in the range of 5.1-5.9 GHz is greater than 9 dB. It meets the requirements of the high-frequency operating band, the isolation between the two ports exceeds 20 dB, demonstrating satisfactory performance characteristics.

The radiation pattern of port 1 and port 2 of the antenna at 5.1-5.9 GHz is simulated, which has a good cross isolation. The co-planar and cross-polarization of the simulated antenna radiation pattern at the $\phi = 0°$ and $\phi = 90°$ sections are shown in Fig. 7.

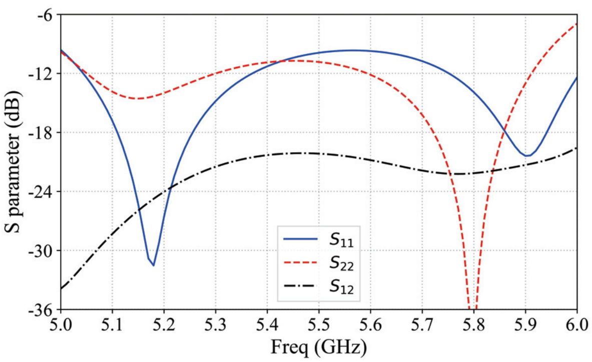

Fig. 6. High-frequency antenna S parameter.

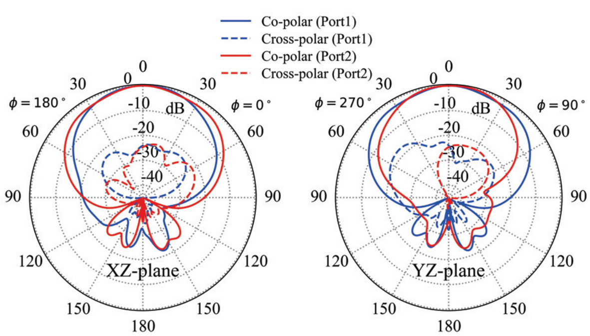

Fig. 7. High-frequency antenna radiation pattern at 5.8 GHz.

III. DUAL-POLARIZED DUAL-BAND ANTENNA ARRAY

Base station antennas typically require a narrower beam and higher gain. Based on the antennas proposed in section II, the low-frequency four-element dual-polarized antenna array and the high-frequency four-element dual-polarized antenna array are designed, constructed, and measured. Each of these antenna arrays is fed by two 1-to-4 power dividers. Each polarized port provides simultaneous signal distribution in the 2.41-2.484 GHz and 5.1-5.9 GHz bands via a frequency selector. The antenna geometry including the low-frequency antenna array, high-frequency antenna array, power divider, and frequency selector is shown in Fig. 8.

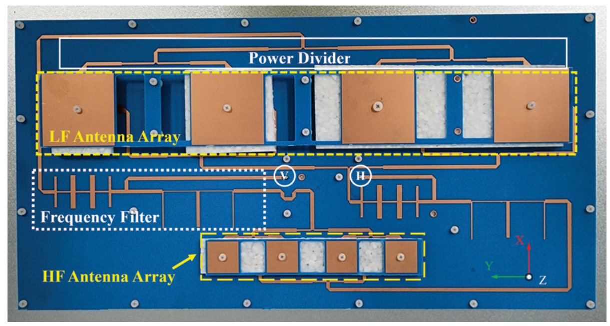

Fig. 8. Prototype of the dual-frequency dual-polarization antenna.

Figures 9 (a) and 9 (b) show the simulated S-parameters of the power divider for low and high frequencies attached to its geometry. Only the combination of T-junction and 1/4 wavelength converter is used through the cascade of two power splitters to divide the energy into four equal parts in the structure. The impedance of each part of the power divider can be calculated from (4):

$$\begin{gathered}\frac{1}{Z_0} = \frac{1}{Z_1} + \frac{1}{Z_2}, \\ Z_L = \sqrt{Z_0 Z_1},\end{gathered} \tag{4}$$

where Z_1 is impedance of T-junction 1 output port, Z_2 is impedance of T-junction 2 output port, Z_0 is impedance of the T-junction input port, Z_L is characteristic impedance of 1/4 wavelength converter.

The parameter values defined in Fig. 9 (a) are as follows (unit: mm) : $W_{d1} = 2.2$, $W_{d2} = 19.9$, $W_{d3} = 67.9$, $L_{d1} = 1.25$. The parameter values defined in Fig. 9 (b) are as follows (unit: mm) :$W_{d5} = 2.2$, $W_{d6} = 8.4$, $L_{d5} = 1.16$, $L_{d6} = 2.2$.

To optimize the efficiency of the dual-band antenna and make the single port provide the matching signal frequency to the low-frequency antenna array and the high-frequency antenna array at the same time, a duplex filter is designed in this work. The filter consists of a low-pass filter and a band-stop filter.

The filter for sorting the low-frequency signal is a step-impedance low-pass filter. The passband cutoff

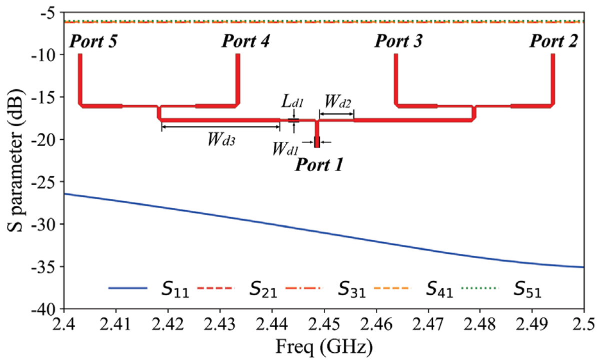

(a)

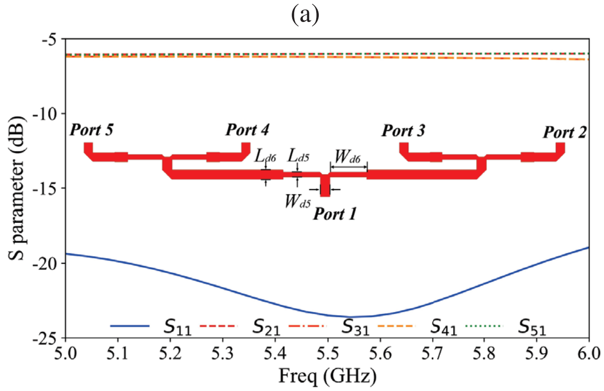

(b)

Fig. 9. Simulated S-parameters of power divider: (a) simulated S-parameters of the low-frequency power divider and (b) simulated S-parameters of the high-frequency power divider.

frequency is 2.6 GHz. According to the value table of the prototype components of the low-pass filter, it can be found that $g_1 = 3.5182$, $g_2 = 0.7723$, $g_3 = 4.6386$, $g_4 = 0.8039$, $g_5 = 4.6386$, $g_6 = 0.7723$, $g_7 = 3.5182$. According to the short transmission line approximate equivalent circuit theory, the length of inductance and capacitance section is calculated by (5):

$$\beta l = \frac{LR_0}{Z_h}, \qquad \beta l = \frac{CZ_l}{R_0}, \tag{5}$$

where R_0 is the filter impedance, and L and C are the normalized component values (g_k) of the low-pass prototype. Z_h is a microstrip line high impedance, Z_l is a microstrip line low impedance.

Under the constraint of (6):

$$\beta l < \pi/4, \qquad \frac{Z_h}{Z_l} \to \infty, \tag{6}$$

the reference values of microstrip line impedance and length can be obtained. The structure in Fig. 10 can be obtained by further simulation.

The filter for sorting the high frequency signal is a truncated band-stop filter with a cutoff frequency of 2.45 GHz. The filter prototype is transformed into a truncated microwave filter by using the Richard transform and Koloda identity relation, and its structure is shown in the Fig. 10. The structure ensures that the low-frequency signal of 2.41-2.484 GHz is correctly fed into the low-frequency antenna array while the high-frequency signal of 5.1-5.9 GHz is correctly fed into the high-frequency antenna array, and the signal can pass almost without loss within the matched frequency. Low-frequency signals and high-frequency signals are highly isolated. Figure 10 shows the structure of the duplex filter, and the parameter values defined in the figure are as follows (unit: mm): $W_{f2} = 3$, $W_{f3} = 35$, $W_{f4} = 1.5$, $W_{f5} = 0.8$, $W_{f6} = 44$, $W_{f7} = 2$, $L_{f1} = 19$, $L_{f2} = 20.5$, $L_{f3} = 1$, $L_{f4} = 1.5$, $L_{f5} = 21.7$, $L_{f6} = 0.6$, $L_{f7} = 22.7$.

As shown in Fig. 10, port 1 serves as the signal input port, while port 2 and port 3, respectively, function as the high-frequency and low-frequency signal outputs. The S-parameters of the duplex filter within the frequency band of 2.41-2.484 GHz and 5.1-5.9 GHz are shown in Fig. 11. It can be seen in Fig. 11 that the return loss of the duplex filter is greater than 10 dB in the dual frequency bands, and the high-frequency and low-frequency signals are separated smoothly after passing through the duplex filter and are transmitted to the matching port.

After optimization, the optimized distance between the low-frequency antenna elements is set to be 0.75λ (λ is the wavelength at 2.5 GHz) while the distance between the high-frequency antenna elements is set to be 0.65λ

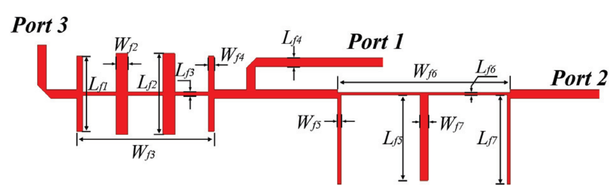

Fig. 10. Geometry of the duplex filter.

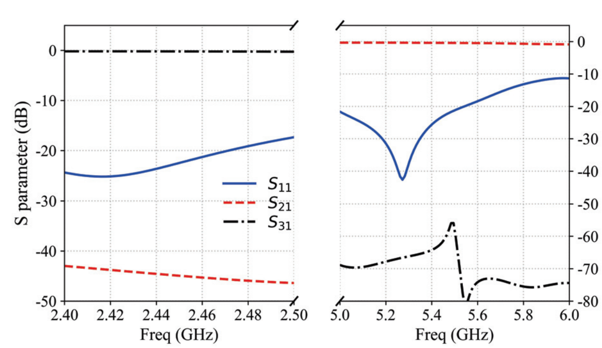

Fig. 11. Simulated S-parameters of the duplex filter.

(λ is the wavelength at 5.45 GHz). The current distribution of the antenna is shown in the Fig. 12. The signal leads to different antenna array elements according to different frequencies, the surface of the patch has a stable current distribution.

The measured and simulated S-parameters of the proposed outdoor Wi-Fi antenna are shown in Fig. 13. It is observed that the dual-frequency dual-polarized antenna achieves bandwidths of 2.41-2.484 GHz and 5.1-5.9 GHz. Furthermore, the isolation between the two ports remains consistently superior to 20 dB across the entire operational bandwidth.

The proposed antenna was measured by a robotic far-field measurement system. The simulated and measured results of co-planar polarization and cross-

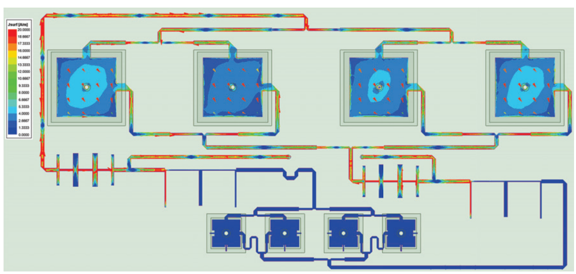

(a)

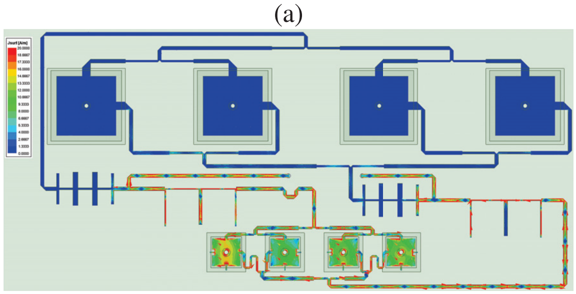

(b)

Fig. 12. Current distribution of antenna: (a) currents at 2.45 GHz and (b) currents at 5.8 GHz.

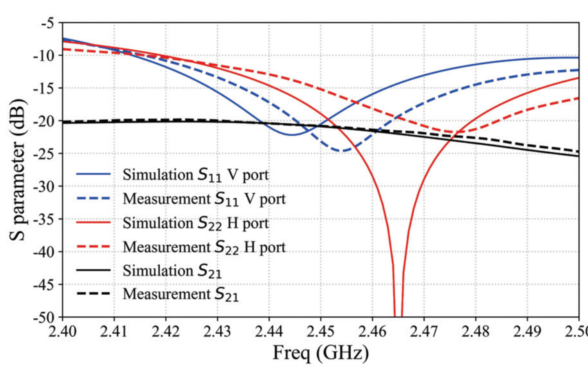

(a)

Fig. 13. *Continued*

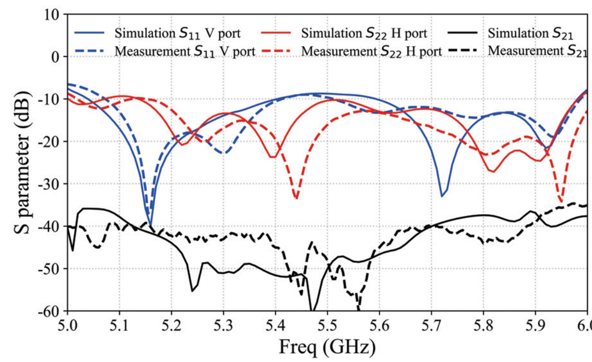

(b)

Fig. 13. S-parameters of the proposed antenna: (a) low-frequency band and (b) high-frequency band.

polarization of two polarizations are shown in Fig. 14. The gain of the proposed antenna is shown in Fig. 15 (a).

Table 1 shows the performance of this antenna compared with other dual-polarized antennas. [11], [15] has a higher isolation, but limited gain and a higher profile of $0.12\lambda_0$. The proposed patch antenna has a high isolation of 35 dB in the high frequency band and a low profile of $0.04\lambda_0$. In the case of similar gain, the height of the

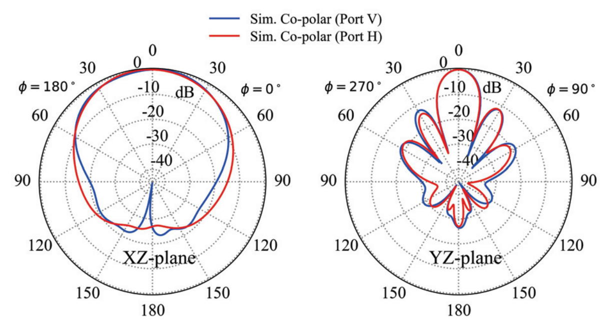

(a)

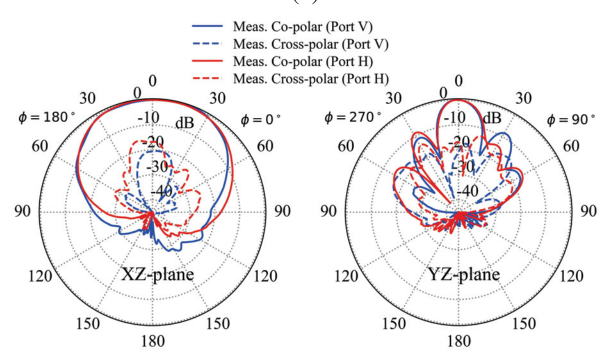

(b)

Fig. 14. Simulated and measured radiation patterns of the proposed antenna: (a) simulated radiation pattern at 2.45 GHz and (b) measured radiation pattern at 5.8 GHz.

Table 1: Comparison of proposed and reference antenna

Ref.	Frequency (GHz)	Number of Unit	Dimension (λ_0)	Height (λ_0)	Substrate Thickness (mm)	Gain (dB)	Isolation (dB)
[11]	3.14-3.81	1	0.45×0.45	0.12	0.8	8.1	>43
[15]	1.71-2.1; 3.3-3.8	1	0.54×0.54	0.13	0.8	>6; >9	>30
[6]	0.82-0.99; 1.68-2.86	4	3.06×0.94	0.11	1	13.8; 16.7	>25
[10]	1.69-2.5	4	3.17×1.12	0.13	1	13.9	>27
Proposed	2.4-2.48; 5.1-5.9	4	2.6×1.4	0.04	0.74	13.6±0.7; 13.2±0.3	>20; >35

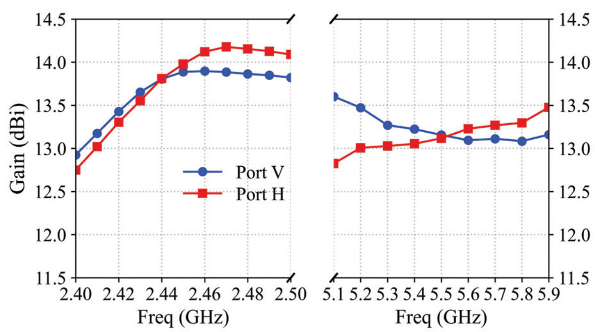

(a)

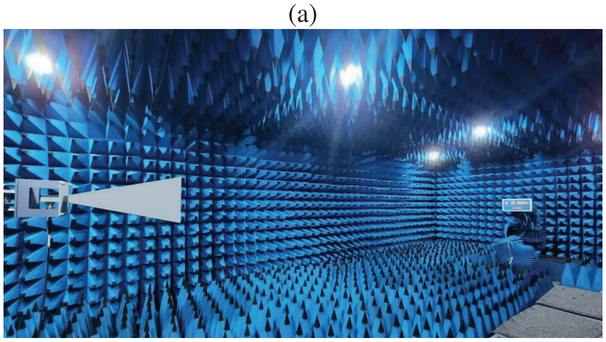

(b)

Fig. 15. Measured gains for the proposed antenna: (a) measured gains for port V and port H and (b) antenna measured in chamber.

antenna proposed in this manuscript is much smaller than the design of the literature [6], [10]. More importantly, the substrate of this design is thinner and smaller in size, and it has excellent isolation. Therefore, such antennas are preferable in applications requiring low profile and lightweight miniaturization.

IV. CONCLUSION

A novel outdoor Wi-Fi antenna with dual-band and dual-polarization capability is proposed in the manuscript. This proposed antenna uses the coupling of the upper and lower layers of two patch antennas to extend the working bandwidth of the antenna, so that it can meet the working requirements of 2.4 GHz and 5 GHz band Wi-Fi. The substrate used in the design is a kind of self-developed blue flexible material, which has the characteristics of light weight and low cost, and the thickness of the substrate material used is less than that of the general material. The fabricated prototype antenna achieves operation in the 2.41-2.484 GHz and 5.1-5.9 GHz range, and maintains isolation of better than 20 dB (2.4 GHz band) and 35 dB (5 GHz band) between its two ports. For vertical polarization, the antenna gain is 13.88 dBi at 2.45 GHz and 13.08 dBi at 5.8 GHz, while the horizontal polarization provides a gain of 13.97 dBi at 2.45 GHz and 13.29 dBi at 5.8 GHz, the proposed antenna achieves stable and high gain in both polarization cases. The height of this antenna is $0.04\lambda_0$, which is much smaller than the general size of other low-profile antennas. Such antennas are preferable in applications requiring low profile and lightweight miniaturization, and has a huge potential market value.

ACKNOWLEDGMENT

This work is supported by the Major Science and Technology Project of Zhongshan City, under grant No. (2022A1012).

REFERENCES

[1] Z. N. Chen, X. Qing, T. S. P. See, and W. K. Toh, "Antennas for WiFi connectivity," *Proceedings of the IEEE*, vol. 100, no. 7, pp. 2322-2329, 2012.

[2] W. Zhou, S. Abdullah, J. Labossiere, N. Javanbakht, J. Shaker, G. Xiao, and R. E. Amaya, "Impact of amplitude and phase imbalance on dual differential fed patch antenna with high isolation," *IEEE Open Journal of Antennas and Propagation*, vol. 3, pp. 1227-1233, 2022.

[3] J. Chen, M. Berg, K. Rasilainen, Z. Siddiqui, M. E. Leinonen, and A. Pärssinen, "Broadband cross-slotted patch antenna for 5G millimeter-wave applications based on characteristic mode analysis,"

IEEE Transactions on Antennas and Propagation, vol. 70, no. 12, pp. 11277-11292, 2022.

[4] Y. Sun, P. Liu, and S. Zhang, “A wideband low-profile dual-polarized antenna with transmission characteristics,” in *2023 IEEE-APS Topical Conference on Antennas and Propagation in Wireless Communications (APWC)*, pp. 125-127, 2023.

[5] X. Qin and Y. Li, “Dual-wideband dual-polarized gridded patch antenna array for 5G millimeter-wave systems,” in *2022 International Symposium on Antennas and Propagation (ISAP)*, pp. 55-56, 2022.

[6] L. Y. Nie, X. Q. Lin, Y. J. Chen, J. Zhang, B. Wang, Z. Q. Yang, and Y. Fan, “A low-profile coplanar dual-polarized and dual-band base station antenna array,” *IEEE Transactions on Antennas and Propagation*, vol. 66, no. 12, pp. 6921-6929, 2018.

[7] M. Milijic and B. Jokanovic, “Dual polarized crossed slot antennas proposed for IoT applications,” in *2023 10th International Conference on Electrical, Electronic and Computing Engineering (IcETRAN)*, pp. 1-6, 2023.

[8] P. Gao, Y. Xu, H. Ma, C. Wang, C. Sun, and J. Tong, “Design of a dual-polarized antenna with PPW and dipole for 5G application,” in *2022 IEEE MTT-S International Microwave Workshop Series on Advanced Materials and Processes for RF and THz Applications (IMWS-AMP)*, pp. 1-2, 2022.

[9] Z. Bao, Z. Nie, and X. Zong, “A novel broadband dual-polarization antenna utilizing strong mutual coupling,” *IEEE Transactions on Antennas and Propagation*, vol. 62, no. 1, pp. 450-454, 2014.

[10] R. Lian, Z. Wang, Y. Yin, J. Wu, and X. Song, “Design of a low-profile dual-polarized stepped slot antenna array for base station,” *IEEE Antennas and Wireless Propagation Letters*, vol. 15, pp. 362-365, 2016.

[11] Y. Liu, S. Wang, X. Wang, and Y. Jia, “A differentially fed dual-polarized slot antenna with high isolation and low profile for base station application,” *IEEE Antennas and Wireless Propagation Letters*, vol. 18, no. 2, pp. 303-307, 2019.

[12] A. Llanga-Vargas, M. Cabedo-Fabrés, M. Ferrando-Bataller, and C. R. Peñafiel-Ojeda, “Multiport broadband 5G MIMO antenna with very high isolation,” in *2021 IEEE International Symposium on Antennas and Propagation and USNC-URSI Radio Science Meeting (APS/URSI)*, pp. 767-768, 2021.

[13] W. C. Mok, S. H. Wong, K. M. Luk, and K. F. Lee, “Single-layer single-patch dual-band and triple-band patch antennas,” *IEEE Transactions on Antennas and Propagation*, vol. 61, no. 8, pp. 4341-4344, 2013.

[14] J. Anguera, G. Font, C. Puente, C. Borja, and J. Soler, “Multifrequency microstrip patch antenna using multiple stacked elements,” *IEEE Microwave and Wireless Components Letters*, vol. 13, no. 3, pp. 123-124, 2003.

[15] Z.-X. Meng and Q.-X. Chu, “A low profile dual band dual-polarization shared-aperture base station antenna,” in *2022 IEEE 10th Asia-Pacific Conference on Antennas and Propagation (APCAP)*, pp. 1-2, 2022.

Yida Fan graduated with a bachelor’s degree from Changchun University of Science and Technology in 2021, and in the same year, he began a direct Ph.D. program at the same university. He is currently based at the Xiangshan Laboratory of Zhongshan Institute of Changchun University of Science and Technology, where his research focuses on antenna design, array antenna pattern synthesis, and computational electromagnetics.

Lijuan Li is a doctoral supervisor at the School of Optoelectronic Engineering, Changchun University of Science and Technology, and the Dean of the Zhongshan Institute of Changchun University of Science and Technology. Her primary research interests include optoelectronic precision measurement and digital twin assembly evaluation technology, terahertz non-destructive testing and evaluation technology for composite materials, and structural health monitoring and evaluation technology.

Ravi Kumar Arya received his Ph.D. from Pennsylvania State University (USA) in August 2017. He is currently an associate professor at the Zhongshan Institute of Changchun University of Science and Technology. His research has long been focused on electromagnetic theory, antenna engineering, computational electromagnetics, and microwave engineering.

Xianghua Ma is an antenna engineer of EMed Technology Co. Ltd. She has been engaged in electromagnetic simulation and engineering design of antenna for a long time, and has rich experience in antenna design.

Shiyuan Kong received her Master's degree from Changchun University of Science and Technology. She is an administrator and quality engineer at the Xiangshan Laboratory of Zhongshan Institute of Changchun University of Science and Technology. Her work involves radar calibration technology, terahertz imaging technology research, as well as laboratory system certification and laboratory quality control.

Junwei Dong obtained his Ph.D. from Virginia Polytechnic Institute and State University (Virginia Tech), USA, in September 2009. He is an adjunct professor at the Zhongshan Institute of Changchun University of Science and Technology, as well as an expert receiving a special government allowance. His primary focus is on radar and sensor systems, computational electromagnetics, antennas and RF components, wireless communication technologies, microwave testing, and automation.

Design of a Miniaturized Symmetrical E-shaped MIMO Antenna with Low Coupling

Xuemei Zheng[1], Ziwei Zhao[2], Yuwen Pan[3], and Tongchao Zhang[2]

[1]Key Laboratory of Modern Power System Simulation and Control and Renewable Energy Technology
Ministry of Education, Northeast Electric Power University, Jilin, China
zhengxuemei@neepu.edu.cn

[2]Northeast Electric Power University
Jilin, China 2202200370@neepu.edu.cn, 1559514836@qq.com

[3]Sainty-tech Communications Ltd.
Nanjing, China
peter.pan@sainty-tech.com

Abstract **–** In order to meet the demand of contemporary 5G mobile communication for miniaturized MIMO antenna systems, this paper proposes a symmetric E-shaped patch antenna. It is mainly realized by digging out the simple rectangular radiation patch, and etching four rectangular slots at the ground plane to widen the working bandwidth. The overall size of the antenna is 20 mm × 40 mm. However, there is current mutual coupling between the two radiation patches closely arranged up and down, which greatly affects the radiation effect of the antenna. Therefore, in order to reduce the coupling degree between each other, a 1 × 3 metamaterial (MTM) array structure is added between the two patches, in which the structure of the MTM unit is similar to a "concave" character. Simulation and real measurement of antennas using 3D electromagnetic simulation software HFSS and vector network analyzer, and the test results show that the proposed antenna is S_{11} <-10 dB in 5.32-6.02 GHz (relative bandwidth of 12.35%), the isolation degree S_{21} is above -18 dB throughout the operating frequency band, and the overall Envelope correlation coefficient (ECC) is less than 0.02 in the working band, which further confirms that the designed MIMO antenna has good isolation. The radiation pattern of the antenna is good, which is suitable for the basic requirements of 5G WLAN band.

Index Terms **–** E-shaped patch, high isolation, metamaterial (MTM), MIMO antenna array, miniaturization.

I. INTRODUCTION

With the development of data coding technology, wireless communication has achieved a fast data transmission rate. However, in complex propagation environments, transmitted signals are limited by multipath fading and interference[1]. A single antenna unit can no longer meet the development needs of the communication spectrum, and MIMO antennas[2] come into being. As a new type of MIMO, it can ensure that the network bandwidth remains unchanged under the premise of exponentially increasing the capacity of the communication system and spectrum utilization[3] and, at the same time, can effectively overcome the impact of multipath and improve the communication quality and reliability of the network[4].

In recent years, character-shaped antennas have been proposed, which greatly increases the types of antennas and have a wide range of application scenarios. Back-to-back U-shaped monopole antenna [5] has a large polarization bandwidth, and some E-shaped patches have been designed. For example, an easy-to-fabricate E-shaped compact patch antenna with broadband and multi-band capabilities [6], and a triple-band E-shaped patch antenna applied to the 4G communication band [7]. However, these character antennas mentioned above are in the form of a single antenna, which cannot meet the demands of contemporary 5G communications, so the aim of this paper is to design a two-element MIMO array antenna to meet the requirements of contemporary mobile communications. In addition, current MIMO antennas focus more on performance indicators such as low coupling and high gain, while paying less attention to the miniaturization of antennas. With the continuous development of 5G wireless communication devices towards miniaturization and slimmer designs, the internal space of these devices is limited. However, miniaturized MIMO antennas[8, 9] can be better integrated into these compact devices.

Submitted On: June 8, 2024
Accepted On: December 4, 2024
https://doi.org/10.13052/2024.ACES.J.391203

Although the MIMO antenna has advantages that cannot be matched by a single antenna, it also has its own biggest drawback, that is, as a multi-input and multi-output antenna, it will produce a strong electromagnetic mutual coupling phenomenon, which will lead to the deterioration of the impedance, gain, direction diagram and other characteristics of the antenna array. How to reduce the coupling degree of the antenna while maintaining the miniaturization of the antenna is an important problem to be solved. At present, domestic and foreign scholars have put forward a variety of methods to reduce the degree of coupling, such as: adding decoupled branches, or adding artificial materials. The isolation of the miniaturized MIMO antenna by at least 10dB is improved by adding two branches to the ground and placing the MIMO antenna vertically [10]. A pair of open branch [11] was used as a decoupling network to reduce the coupling degree between the elevated antennas. Another method is to use artificial materials with special properties, such as electromagnetic band gap (EBG) [12] and metasurface [13], as decoupling structures.

Metamaterials (MTMs) are novel artificial materials that can be embedded between radiation units to improve the isolation without increasing the size and complexity of the antenna system. Literature [14–16] all uses MTM structures as decoupling structures to solve the electromagnetic coupling problem of MIMO antennas. In addition to the method introduced in this paper, the design of microstrip devices based on DMS (Defected Microstrip Structure)[17, 18] is also very common. It is in this context that this paper provides the design, simulation, and testing of a small-size, high-gain and low-coupling MIMO antenna based on MTM. In the proposed design, the improvement of isolation degree is achieved by loading a kind of "concave" shaped MTM structure. The radiating patch reduces the area of the radiating patch by digging slots, and four rectangular slots of equal length are etched on the floor to further broaden the antenna bandwidth. At this time, there is a strong electromagnetic coupling phenomenon between the two closely arranged radiating patches, in order to weaken the electromagnetic mutual coupling between the two, a certain number of MTM unit structures are added to the middle of the array. Simulation and measurement results show that the isolation of the antenna in the operating band reaches more than - 18 dB after loading the MTM structure, and decoupling is achieved across the entire bandwidth after loading the MTM structure. The overall Envelope correlation coefficient (ECC) is less than 0.02 in the working band, which further confirms that the designed MIMO antenna has good isolation.The peak gain is reached at around 6 dBi. In addition, the loading of MTMs reduces the influence of sidelobe radiation of the antenna, which indicates that the antenna's radiating performance has been optimized and enhanced with the addition of MTMs.

II. SYMMETRIC ANTENNA DESIGN PROCESS

Figure 1 shows the geometry of the two-cell compact E-shaped MIMO antenna proposed in this paper. Both patches are printed on a FR4 (dielectric constant of 4.4, dielectric loss angle tangent of 0.02) substrate with a volume of 20 mm × 40 mm × 1.6 mm. And the overall size of the antenna is very small. The antenna structure is firstly to etch the corresponding number of rectangular slots on the single rectangular patch and on the floor respectively so that the proposed single structure achieves the purpose of miniaturization of the antenna patch unit and expansion of its operating bandwidth, and finally, the single radiating patch unit is closely arranged in a symmetric way to form the MIMO two-cell antenna array structure, and the overall design steps are shown in Fig. 2. This is also the difference between the structure proposed in this paper and the previous character-based structure. During the antenna design process, the antenna structure dimensions are modeled and optimized using HFSS electromagnetic simulation sofeware, and the final determined antenna parameters are summarized in Table 1.

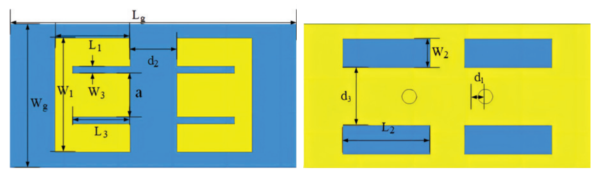

(a) (b)

Fig. 1. The geometry of the E-shaped MIMO antenna: (a) front view and (b) back view.

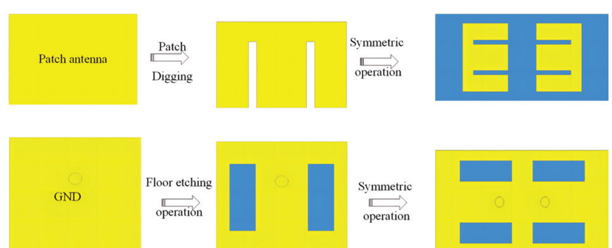

Fig. 2. Steps of the antenna design.

Table 1: Dimensions of the optimized antenna structure (unit: mm)

Parameter	Numerical Value	Parameter	Numerical Value
W_g	20	L_g	40
W_1	15.7	L_1	10.4
W_2	4	L_2	12
W_3	2.6	L_3	2
d_1	2	d_2	6.5
d_3	8	a	6

III. MTM UNIT DESIGN AND ANALYSIS

A. MTM cell design

The electromagnetic properties of artificial MTMs mainly depend on their structure and dimensions, and by designing their structure and dimensions, the metallic ohmic loss and dielectric loss near the resonance frequency can be adjusted to realize the absorption of incident electromagnetic waves. In this paper, we design a MTM unit structure that can exhibit special electromagnetic resonance characteristics near 5.8 GHz, as shown in Fig. 3. The overall size of the designed MTM structure is very small, and the parameters optimized after simulation are a = 5.5 mm, c = t = t_1 = 0.4 mm, g_1 = 0.6 mm, c_1 = c_3 = 0.7 mm, c_2 = 2 mm.

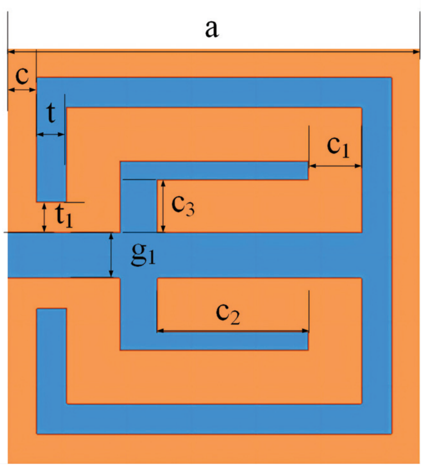

Fig. 3. MTM unit structure diagram.

In order to verify the electromagnetic characteristics of the designed MTM unit, the electromagnetic simulation software HFSS is used for detailed analysis. Open resonant circular and square rings are placed on the upper and lower surfaces of FR4 dielectric substrate with thickness of h = 1.6 mm, and the whole is placed in an air box. In the simulation, the upper and lower surfaces perpendicular to the z-axis are set as wave-port excitation, the front and rear surfaces perpendicular to the x-axis are set as ideal magnetic conductors (Perfect H), and the left and right surfaces perpendicular to the y-axis are set as ideal electric conductors (Perfect E). At this time, the magnetic field is perpendicular to the surface of the MTM cell, which is used to simulate the generation of the magnetic resonance when the magnetic field passes through the cell, as shown in Fig. 4.

B. Simulation analysis

The MTM is characterized by a normally incident X-polarized wave and a scattering parameter extracted from a single unit cell with periodicity. In order to obtain

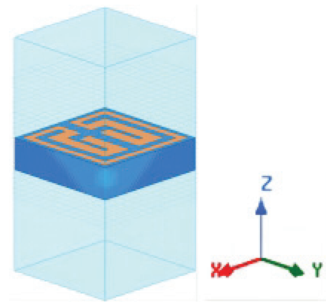

Fig. 4. A 3D view of the MTM cell structure.

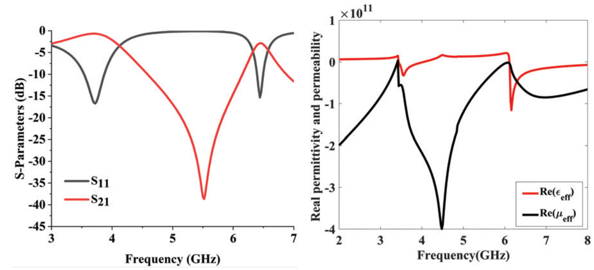

(a) (b)

Fig. 5. (a) Plot of the S-parameter structure and (b) plot of the extracted equivalent parameter values.

the characteristic parameters of the MTM, the S parameter inversion method [19, 20] is needed. Figures 5 (a) and (b) show the magnitude of the S-parameter of the MTM cell structure and the equivalent parameter values of its permeability and permittivity, respectively. From the results, it can be seen that the value of its equivalent magnetic permeabilityμ at 5-6 GHz is negative, and the value of the equivalent permitivity ε is positive, which can indicate that the MTM is an electronegative material. It can be observed from the transmission and reflection characteristics that the MTM has a determined suppression bandwidth between 5-6 GHz, especially a transmission stop band due to magnetic resonance near the center frequency point 5.8 GHz. It can be used to suppress the propagation of coupling current from one antenna element to another to improve isolation between antenna array elements.

IV. ANALYSIS OF THE OVERALL MIMO ANTENNA STRUCTURE AND THE EXPERIMENTAL RESULTS

The purpose of decoupling is achieved by loading the 1 × 3 MTM array structures between the two radiation patches, and the overall antenna structure is shown in Fig. 6. To make the measurements comparable, the original and loaded MTM antennas adopt the same structural dimensions, where d_3 = 0.4 mm, d_4 = 0.5 mm.

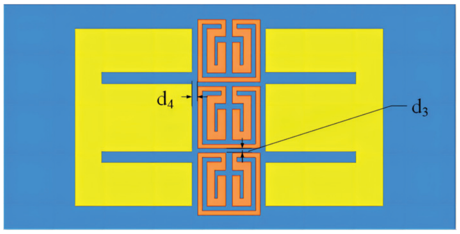

Fig. 6. Front view of the integral MIMO antenna loaded with MTMs. (Blue is the dielectric substrate, the radiation patch is yellow and the MTM structure on the same surface as the radiation patch is orange).

A. S-parameter simulation analysis

Figure 7 is a comparison diagram of the antenna S-parameters obtained by the HFSS software simulation. Figure 7 (a) shows that the central working frequency of the MIMO antenna loaded with MTMs is slightly shifted to the low frequency, but the overall deviation of the working frequency band is not large. It can be seen from Fig. 7 (b) that by loading MTMs, the coupling coefficient S_{21} obtained a substantial decrease of the MIMO antenna in the entire working frequency band. Compared with the original antenna, the coupling degree not only achieves the minimum requirement of the MIMO antenna but also achieves a maximum of 10 dB decoupling, and the coupling reduction effect is remarkable.

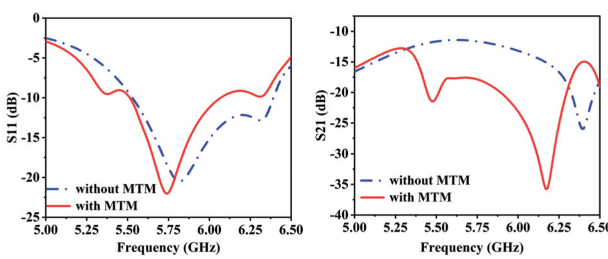

(a) (b)

Fig. 7. S-parameter plot of the antenna: (a) S_{11} and (b) S_{21}.

B. 2D radiation pattern

Figure 8 shows a comparison of the two-dimensional far-field radiation pattern of the antenna before and after loading the MTM structure in the E-plane and H-plane at 5.8 GHz. As can be seen from the comparison figures, compared with the ordinary MIMO antenna, the directional map of two-dimensional far-field radiation in the H-plane of the MIMO array antenna loaded with MTMs is unchanged, indicating that the introduction of the MTMs does not damage the far-field radiation characteristics of the antenna. In addition, it can be seen from Fig. 8 (a) that adding MTM enhances the main flap radiation of the far-field radiation of the antenna's E-plane more obviously. That is, the MIMO antenna without MTM produces large side lobe radiation between 120 and 180 degrees. Instead, the MIMO antenna with MTM produces strong main lobe radiation in the direction of 150 degrees. The side lobe radiation at this time is very small, which further indicates that the MTM structure has a significant role in improving the performance of the MIMO antenna.

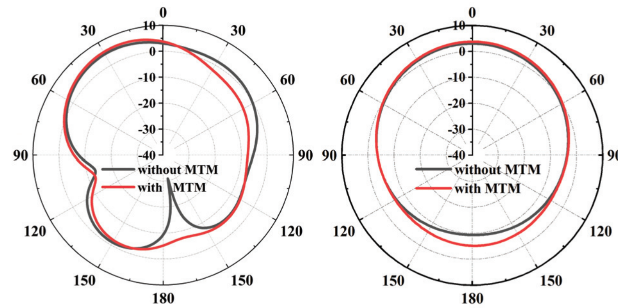

(a) (b)

Fig. 8. Radiation pattern of the antenna with and without MTM: (a) E-plane and (b) H-plane.

C. Antenna surface current distribution

In order to understand the decoupling principle of the loaded MTM antenna more intuitively, the surface current distribution of the antenna before and after the loading of the MTM is analyzed at the center frequency point of 5.8 GHz, and the comparison results are shown in Fig. 9. In order to make a visual comparison, the same current intensity scale has been chosen for both figures, with darker colors (red) indicating a denser distribution of current intensity on the surface, and lighter colors (blue) indicating a sparser distribution of current intensity on the surface, where the left figure is the case not based on MTMs, and the right figure is the case based on MTMs. From the comparative analysis of the left and right figures, it can be seen that the surface current strength distribution on the antenna array element in the left figure is denser, which can produce stronger coupling to the neighboring antenna array elements, whereas in the right figure, after the addition of the MTM structure in the middle of the two antenna units, the surface current strength distribution on the following antenna array element becomes obviously sparse, which further indicates that the designed MTMs can effectively weaken the electromagnetic mutual coupling between two closely spaced antenna elements.

D. 3D radiation gain direction map of the antenna

A comparison of the 3D radiation gain directional map of the antenna at the center frequency point 5.8 GHz

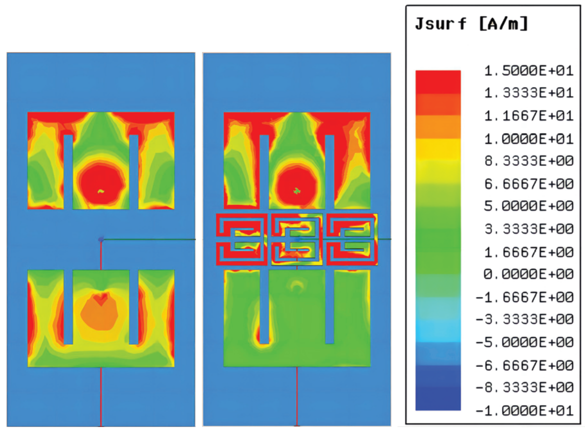

Fig. 9. Surface current map at 5.8 GHz: (a) without MTMs, (b) with MTMs and (c) current intensity distribution.

generated in the electromagnetic simulation software is shown in Fig. 10. From the figure, it can be seen that the addition of the MTM has an effect on the antenna gain, that is, it increases the antenna gain by a small amount, with an overall increase of 1.05 dB. From the 3D radiation gain direction map, the highest gain of the antenna reaches 5.89 dB, which meets the range requirements of 5G mobile communication antennas for high gain.

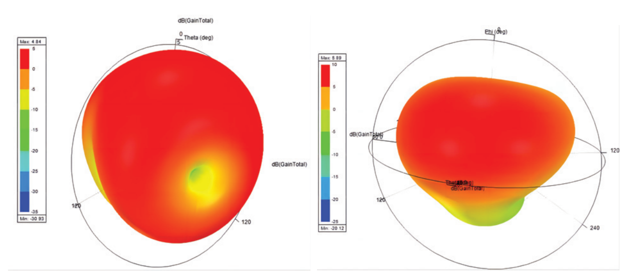

Fig. 10. 3D gain orientation diagram: (a) without MTMs and (b) with MTMs.

E. Gain and efficiency of proposed antenna

Figure 11 shows the resulting plot of the gain and efficiency of the MIMO antenna after loading the MTM. We can see from the figure that the peak gain ranges from 4.08 dBi to 5.95 dBi. The radiation efficiency ranges from 66% to 80% in the entire operating frequency band, and the radiation efficiency at the center frequency of 5.8 GHz is about 80%. The maximum gain is 5.95 dBi at 5.9 GHz and the minimum gain is 4.08 dBi at 5.36 GHz.

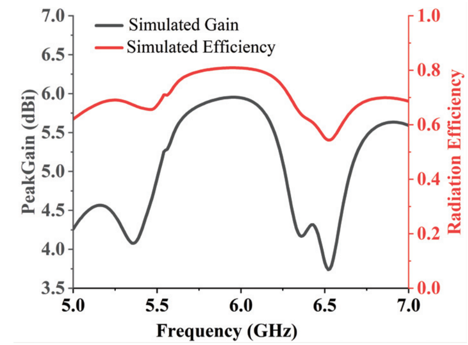

Fig. 11. Gain and efficiency of proposed antenna.

F. The MIMO antenna diversity characteristics

ECC and diversity gain are the two most important parameters to show the diversity characteristics of MIMO antenna. Figure 12 presents the simulated ECC and diversity gain diagram of MIMO antenna. It can be seen from the figure that the ECC value meets the minimum requirements of the ideal value in the entire working band, and the overall ECC is less than 0.02 in the working band. This confirms that the designed MIMO antenna has good isolation and the best performance under a multipath fading environment. Moreover, in the working frequency band, the proposed MIMO antenna achieves a diversity gain of 10 dBi with good diversity characteristics.

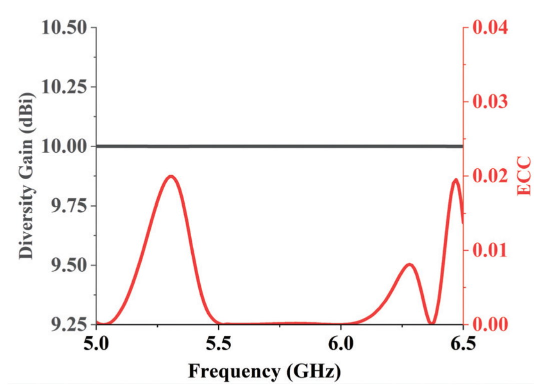

Fig. 12. Gain and efficiency of proposed antenna.

G. Comparative analysis of antenna array elements

The MIMO antenna arrays presented in Table 2 have similarities in shape, and their performance is compared in this section. Compared with [21–23], the structure in this paper has advantages in isolation and gain although the bandwidth is relatively narrower. Although the design has disadvantages in isolation compared with [24–26], the operating bandwidth is relatively wider. Compared with these four antenna arrays,

Table 2: Comparison between the proposed antenna and other antennas

Ref	Electrical Dimensions	Center Frequency Point (GHz)	Bandwidths (GHz)	Isolation (GHz)	Gain (GHz)
[21]	$0.57\lambda_0 \times 0.385\lambda_0$	6, 8, 10	5.2-10.6 (68.35%)	<-15	5.7
[22]	$1.07\lambda_0 \times 1.07\lambda_0 \times 0.01\lambda_0$	2.3, 2.5, 2.65	2.22-2.75 (21.3%)	<-18	5.5
[23]	$0.44\lambda_0 \times 0.5\lambda_0$	3.5	3.22-4.36 (30.07%)	Not Given	5.2
[24]	$0.81\lambda_0 \times 0.5\lambda_0 \times 0.02\lambda_0$	2.45	2.449-2.456 (0.29%)	<-22	6.68
[25]	$0.4\lambda_0 \times 0.61\lambda_0 \times 0.01\lambda_0$	2.77	2.73-2.85 (4.3%)	<-50	Not Given
[26]	$0.84\lambda_0 \times 1.01\lambda_0$	3.5	3.5-3.55 (1.42%)	<-20	Not Given
This paper	$0.66\lambda_0 \times 0.33\lambda_0 \times 0.02\lambda_0$	5.8	5.32-6.02 (12.35%)	<-18	5.89

the antenna structure has a greater advantage in terms of small size, which is better able to meet the demand of modern mobile devices on the antenna miniaturization. In addition, the comparison of the electrical dimensions of the antennas is more reflective of the smaller dimensions of the proposed antennas. Therefore, the design can meet the most basic requirements of the antenna in high isolation, small size, broadband and high gain.

V. ANTENNA FIELD MEASUREMENT AND RESULT

To validate the proposed design, an antenna prototype was made and measured. The antenna was simulated using ANSYS HFSS. The antenna made according to the above parameters is shown in Fig. 13, and the S parameter of the antenna was measured using the Network Analyzer (NA). The measured and simulated values of the S parameters are shown in Fig. 14. Comparing the simulation results and the measured results, we find that there is a small frequency shift. This may be due to factors such as SMA connector loss, cable loss, and radiation boundary during measurement. The measured results show that the measured frequency band of the proposed MIMO antenna of S_{11} <-10 dB is basically unchanged and S_{21} <-20 dB. And the measured and simulation results are generally moderate.

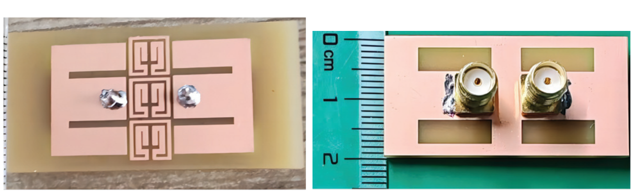

(a) (b)

Fig. 13. Physical representation of an antenna loaded with MTMs: (a) front view and (b) back view.

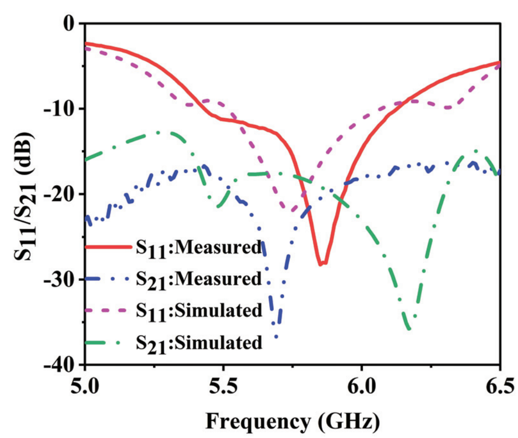

Fig. 14. Measured and simulated S-parameters of the designed MIMO antenna.

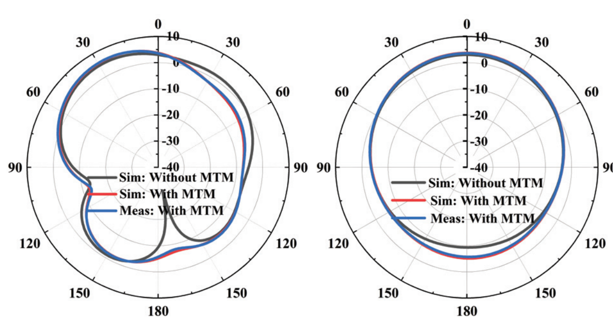

(a) (b)

Fig. 15. Measured and simulated radiation pattern(with or without MTMs) at 5.8 GHz: (a) Phi = 0 °C and (b) Phi = 90 °C.

Next, the radiation characteristics of MIMO antenna in both cases (with or without MTMs) were further studied. Figure 15 shows the simulation and measured radiation pattern of the main plane azimuth (Phi = 0 °C) and pitch (Phi = 90 °C) at 5.8 GHz, which shows that the introduction of the MTM has a slight effect on the deviation of the radiation pattern.

VI. CONCLUSION

In this paper, a symmetric "E-shaped" MIMO dual-cell array antenna for 5G WLAN band is proposed by combining the character-shaped radiating patch and MIMO technology to optimize the shortcomings of a single patch antenna, such as low spectrum utilization. A kind of "concave" shaped MTM cell structure is proposed to improve the isolation degree between two antenna cells, which is mainly placed between two radiating patches in a 1 × 3 arrangement. The distance from the MTM array structure to the two patch cells can be adjusted to reduce the coupling degree between the MIMO antenna array cells. Comparison of the measured and simulated results shows that the introduction of MTM improves the impedance matching characteristics of the antenna array compared with the original antenna and steadily improves the gain of the antenna. Although the gain improves less, the overall gain meets the minimum requirements of high gain. Meanwhile, the isolation degree is above -18 dB throughout the operating frequency band, and achieves a maximum of 10 dB decoupling compared to the antenna array without MTM. Compared with the same type of antenna, the antenna has some advantages in terms of miniaturization, gain and isolation. Therefore, the proposed MIMO antenna system is suitable for the field of miniaturized MIMO dual array antennas with high isolation.

ACKNOWLEDGMENT

This research was funded by the doctoral research startup fund of Northeast Electric Power University, and project number is BSIXM-2021207. This paper was funded by the National Natural Science Foundation of China (61803356).

REFERENCES

[1] G. J. Foschini, "Layered space-time architecture for wireless communication in a fading environment when using multi-element antennas," *Bell Labs Technical Journal*, vol. 1, no. 2, pp. 41–59, 1996.

[2] A. J. Paulraj, D. A. Gore, R. U. Nabar, and H. Bolcskei, "An overview of MIMO communications - a key to gigabit wireless," *Proceedings of the IEEE*, vol. 92, no. 2, pp. 198–218, 2004.

[3] J. Kulkarni, A. Desai, and C. Y. D. Sim, "Wideband Four-port MIMO antenna array with high isolation for future wireless systems," *AEU: Archiv fur Elektronik und Ubertragungstechnik: Electronic and Communication*, vol. 128, p. 153507, 2021.

[4] T. Jiang, T. Jiao, and Y. Li, "Array mutual coupling reduction using L-loading E-shaped electromagnetic band gap structures," *International Journal of Antennas and Propagation*, vol. 2016, no. pt.2, pp. 6731014.1–6731014.9, 2016.

[5] Y. Q. Zheng and M. Gao, "A wideband back-to-back U-shaped monopole antenna," *Microwave and Optical Technology Letters*, vol. 61, no. 7, pp. 1815–1820, 2019.

[6] A. G. Koutinos, D. E. Anagnostou, R. Joshi, S. K. Podilchak, G. A. Kyriacou, and M. T. Chryssomallis, "Modified easy to fabricate E-shaped compact patch antenna with wideband and multiband functionality," *IET Microwaves Antennas & Propagation*, vol. 12, no. 3, pp. 326–331, 2017.

[7] K. Yu, Y. Li, X. Luo, and X. Liu, "A modified E-shaped triple-band patch antenna for LTE communication applications," in *IEEE International Symposium on Antennas and Propagation*, pp. 295–296, 2016.

[8] H. Cao, Y. Z. Xie, and Y. Y. Wu, "A miniaturized MIMO antenna with polarization converter for reduction of RCS and mutual coupling," in *2024 IEEE MTT-S International Wireless Symposium (IWS)*, 2024.

[9] A. A. Khan, S. A. Naqvi, M. S. Khan, and B. Ijaz, "Quad port miniaturized MIMO antenna for UWB 11 GHz and 13 GHz frequency bands," *AEU - International Journal of Electronics and Communications*, p. 153618, 2021.

[10] L. Liu, S. W. Cheung, and T. I. Yuk, "Compact MIMO antenna for portable devices in UWB applications," *IEEE Transactionson Antennas and Propagation*, vol. 61, no. 8, pp. 4257–4264, 2013.

[11] W. J. Liao, S. H. Chang, J. T. Yeh, and B. R. Hsiao, "Compact dual-band WLAN diversity antennas on USB dongle platform," *IEEE Transactionson Antennas and Propagation*, vol. 62, no. 1, pp. 109–118, 2014.

[12] G. Saxena, P. Jain, and Y. K. Awasthi, "High isolation EBG based MIMO antenna for X-band applications," *2019 6th International Conference on Signal Processing and Integrated Networks (SPIN)*, pp. 97–100, 2019.

[13] M. F. Ismail, M. K. A. Rahim, N. A. Samsuri, N. A. Murad, and A. A. Pramudita, "High isolation MIMO antenna using electromagnetic band gap - EBG structure," *2021 International Symposium on Antennas and Propagation (ISAP)*, pp. 1–2, 2021.

[14] M. A. Abdalla and A. A. Ibrahim, "Compact and closely spaced metamaterial MIMO antenna

with high isolation for wireless applications," *IEEE Antennas & Wireless Propagation Letters*, vol. 12, pp. 1452–1455, 2013.

[15] B. A. F. Esmail and M. SlawomiKoziel, "Design and optimization of metamaterial-based dual-band 28/38 GHz 5G MIMO antenna with modified ground for isolation and bandwidth improvement," *IEEE Antennas and Wireless Propagation Letters*, vol. 22, pp. 1069–1073, 2023.

[16] C. Abdelhamid, M. Daghari, H. Sakli, and C. Hamrouni, "High isolation with metamaterial improvement in a compact UWB MIMO multi-antennas," in *2019 16th International Multi-Conference on Systems, Signals & Devices (SSD),* Istanbul, Turkey, pp. 514-517, 2019.

[17] X. Zheng, T. Jiang, H. Lu, and Y. Wang, "Double-layer microstrip band stop filters etching periodic ring electromagnetic band gap structures," *Electronics*, vol. 9, no. 8, p. 1216, 2020.

[18] X. Zheng and T. Jiang, "Triple notches bandstop microstrip filter based on archimedean spiral electromagnetic bandgap structure," *Electronics*, vol. 8, no. 9, pp. 964–, 2019.

[19] X. Chen, T. M. Grzegorczyk, B. I. Wu, J. Pacheco, and J. A. Kong, "Robust method to retrieve the constitutive effective parameters of metamaterials," *Physical Review E*, vol. 70, 2004.

[20] A. B. Numan and M. S. Sharawi, "Extraction of material parameters for metamaterials using a full-wave simulator [Education Column]," *IEEE Antennas & Propagation Magazine*, vol. 55, pp. 202–211, 2013.

[21] W. Li, W. Xue, and Y. Li, "A wideband Zhong-shaped MIMO antenna," *2021 IEEE International Workshop on Electromagnetics: Applications and Student Innovation Competition (iWEM)*, pp. 1–2, 2021.

[22] J. Jianfeng, "Design and research of wideband MIMO antenna based on meta-materials," *Harbin: Harbin Engineering University*, pp. 43–56, 2021.

[23] R. Kumar, N. Nasimuddin, and R. K. Chaudhary, "A new dual C-shaped rectangular dielectric resonator based antenna for wideband circularly polarized radiation," *International Journal of RF and Microwave Computer-Aided Engineering*, vol. 29, no. 6, pp. e21672.1–e21672.12, 2019.

[24] Z. Niu and H. Zhang, "Isolation enhancement in Chinese character antenna array using simple defect ground structure," *International Journal of RF and Microwave Computer-Aided Engineering*, vol. 29, no. 11, 2019.

[25] S. Luo, Y. Li, and X. Mao, "Isolation enhancement of a two-element MIMO antenna array using rotated E-shaped resonators," in *2017 Progress in Electromagnetics Research Symposium - Fall (PIERS - FALL)*, pp. 262–265, 2018.

[26] X. M. Yang, X. G. Liu, X. Y. Zhou, and T. J. Cui, "Reduction of mutual coupling between closely packed patch antennas using waveguided metamaterials," *IEEE Antennas and Wireless Propagation Letters*, vol. 11, pp. 389–391, 2012.

Xuemei Zheng Ph.D., Associate Professor and Master's Supervisor in Information and Communication Engineering at Northeast Electric Power University. Main research directions: MIMO antennas, microstrip device design, array antennas, high isolation microstrip antennas, antenna beamforming technology, electromagnetic compatibility analysis, and other aspects.

Ziwei Zhao received the B.S. degree from the Inner Mongolia University of Technology in 2022. She is currently pursuing the M.S. degree in Information and Communication Engineering at Northeast Power University. Her research interests include multi-input multi-output antennas, microstrip antennas, array antennas, and high isolation microstrip antennas.

Yuwen Pan Nanjing Sainty-tech Communications Ltd., microstrip device testing and analysis.

Tongchao Zhang received his B.E. degree from the Shenyang Institute of Engineering in 2023. He is currently pursuing his M.S. degree in information and communication engineering at Northeast Power University. His main research areas include MIMO antennas, microstrip antennas, array antennas, highisolation microstrip antennas, and antenna decoupling technology.

A Novel Design for Four-port Metamaterial SRR-loaded MIMO Antenna for 5G and Wireless Communication Applications

M. Rajakumar and M. Meena

Department of Electronics and Communication Engineering
Vels Institute of Science, Technology & Advanced Studies, Tamil Nadu 600117, India
raj998779@gmail.com, meena.se@velsuniv.ac.in

Abstract – In this paper, a new high-polarization metamaterial structure design for a multiple-input, multiple-output (MIMO) antenna with robust isolation is introduced. The antenna design satisfies the requirements of C-band and S-band wireless communication networks up to sub-6 GHz 5G applications. The novel design of the antenna gets three frequency bands—5.8 GHz, 3.4 GHz, and 2.57 GHz—to be taken into consideration. After the integration of metamaterial components and without use of any further decoupling techniques, high isolation of more than 20 dB is achieved. By suppressing the propagation of surface waves, low-band resonators can reduce the mutual coupling between two higher bands. Ultimately, the initial coupling is canceled out using a split-ring resonator (SRR) to minimize coupling in the low band. The stated MIMO antenna has a maximum return loss of -13, -18, and -21 dB and a mutual coupling of -13, -18, and -21 dB. It covers the 2.5, 3.4, and 5.8 GHz bands, which are used for WLAN, LTE, and 5G. Within acceptable bounds, the envelope correlation coefficient is less than 0.01 and the total active reflection coefficient is less than -10 dB. The performance of MIMO antennas is observed practically and reported.

Index Terms – 5G, meta material structure, MIMO design, unit cell, wireless applications.

I. INTRODUCTION

Multiband antennas capable of operating in many frequency bands are becoming increasingly important as mobile communication networks such as WLAN and WiMAX evolve. To make it easier to integrate the antennas with other system parts, they should also have a broad bandwidth and low profile. One effective way to meet the prior requirements is to use printed antennas. Various methods have been explored in the literature to accomplish multi-band properties. In order to produce various resonance frequencies, the most common method involves acting on the radiating element by etching holes or adding conducting strips [1–4]. The metamaterials utilized significantly lessen multi-antenna coupling. The introduction of these materials, known as split-ring resonators (SRR), has boosted S parameters, transmission effectiveness, diversity gain (DG), radiation characteristics, and envelope correlation coefficients (ECC) along the antenna patch plane [5–6].

Low radiative losses show that the separation between the two patch antennas may be increased by up to 20 dB without affecting the impedance bandwidth [6–8]. To meet the demand for multiple frequency bands, a number of strategies have been employed in the literature to produce dual-band or multi-band antennas, including a novel antenna constructed from metamaterial and with a spiral structure to act as a complementary SRR [9–12].

If the multiple-input, multiple-output (MIMO) only functions in one frequency band, it will be unable to fully utilize its inherent benefits and will squander frequency band resources. As a result, one of the fundamental technological problems confronting current wireless terminals and systems is developing an antenna for wireless applications that can handle dual-band or multi-band operations while maintaining acceptable performance [13–14].

The literature has also reported on a number of other MIMO antenna technologies for use in 5G smart phone applications. When it comes to channel capacity, ECC, and isolation, these systems excel. Many strategies, including spatial diversity, can be used to improve isolation between antenna sections [15–16]. Every antenna part must be tiny, well decoupled, and positioned on the phone (PCB or rim) with care. The suggested antenna material carries effectively on a lossy fr-4 substrate. In MIMO systems, proper port fielding and decoupling are required in order to provide uncorrelated channels. For a smooth integration with the increasing popularity of 5G connections, 5G devices must make room for 2G, 3G, and 4G MIMO/diversity antennas [17–18].

II. ANTENNA STRUCTURE AND DESIGN

The dimensions of the proposed antenna's rectangular array are 70 $\times$ 65 mm (width $\times$ length). It is intended to be used as a tri-band MIMO antenna. Thus, a 4-port MIMO antenna with an SRR construction is designed. The 1:7 metamaterial SRR is meant to enhance

Submitted On: July 12, 2024
Accepted On: December 15, 2024
https://doi.org/10.13052/2024.ACES.J.391204

the MIMO system's performance. The outer and inner rings are positioned between the MIMO antennas after achieving lower coupling loss.

The suggested antenna is made using a cheap FR-4 substrate that has a 1.6 mm dielectric constant ($\mu r = 4.3$). To build and optimize the suggested antenna construction, EM Simulator CST Studio Suite was utilized. In Fig. 1, the antenna diagram is displayed.

Figure 2 shows that simulated reflection coefficients perform the highest return loss and radiate 90% of the power with a combination of metamaterial structure. Two concentric metallic rings engraved on a dielectric substrate in the form of a circle or square make up the SRR.

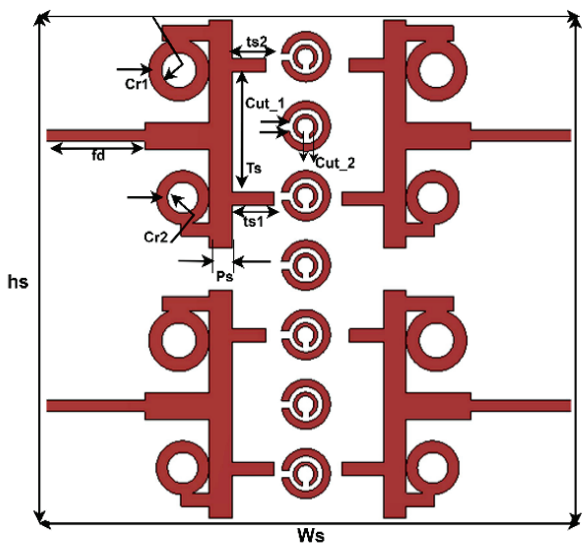

Fig. 1. Proposed antenna structure.

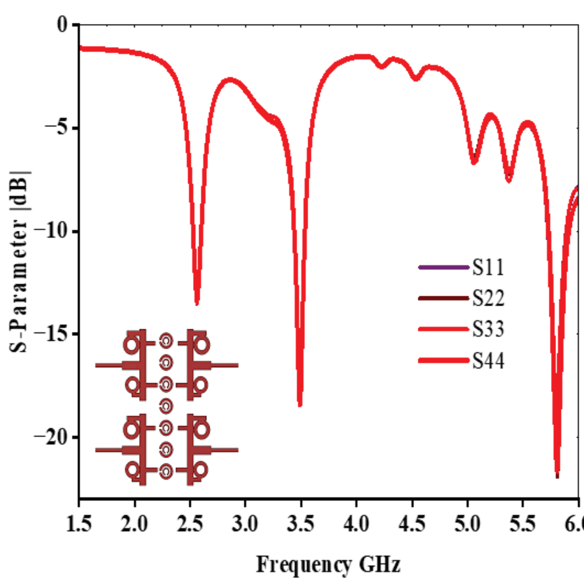

Fig. 2. Reflection coefficient of four antennas.

A. MIMO antenna design

In MIMO systems, contact between the antenna components via surface and space waves creates mutual coupling. As little as -10 dB is the reported gap between MIMO components 1 and 4. The high interaction between antennas 1 and 3 in space and surface waves is the reason for this poor isolation. The suggested MIMO system achieves a maximum gain of 4.4 dBi. The isolation and gain of the MIMO antenna must be improved to reduce the decoupling technique. Two metallic rings that are concentric on the dielectric substrate and etched in the shape of a circle or square make up the SRR. Their opposite ends are divided or have gaps. The MIMO antenna ECC measures the channel correlation between the antennas. The channel capacitance of a MIMO antenna increases the performance of the 4-port antenna as broad-band applications by providing strong mutual coupling between the antennas. The MIMO antenna channel capacitance of M and N Rx and Tx is:

$$c = BW log_2 \left(det \left(I_N + \frac{P_T}{\sigma^2 M} H H^H \right) \right) . \quad (1)$$

The equation for a highly efficient and lossless antenna is based on channel capacitance c and S parameters.

Figure 3 illustrates how the coupled power between two adjacent components is measured using the antenna isolation's reflection coefficient (|S21|). A low-level matched load terminates the antenna output, and S11 is the input reflection coefficient. Forward transmission (from port 1 to port 2), reverse transmission (from port 2 to port 1), and output reflection

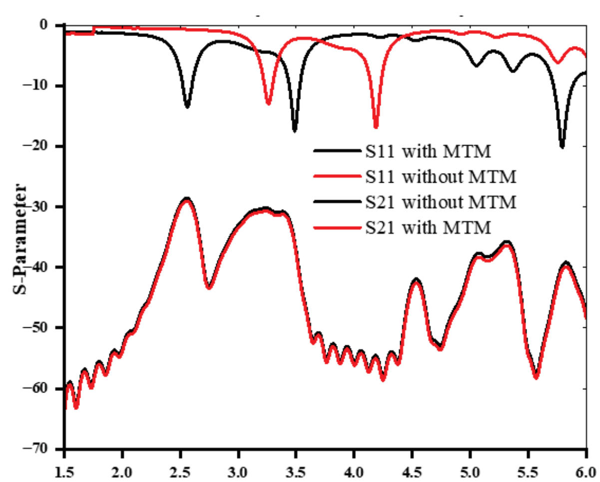

Fig. 3. Transmission coefficient S_{21} and reflection coefficient S_{11}.

coefficient (S22) are represented as S21, S21, and S12, respectively.

Figure 4 shows the reflection coefficients (S11 and S22) that were calculated and measured. With and without metamaterial structure, the planned MIMO systems show similar -15 dB impedance bandwidths. The 5G sub-6 GHz NR bands are still sufficiently covered, notwithstanding a little operational frequency modification brought on by metamaterial effects. After employing the metamaterial, the measured impedance for the originally intended MIMO antenna is BW 2.57 GHz (2.5-5.8 GHz).

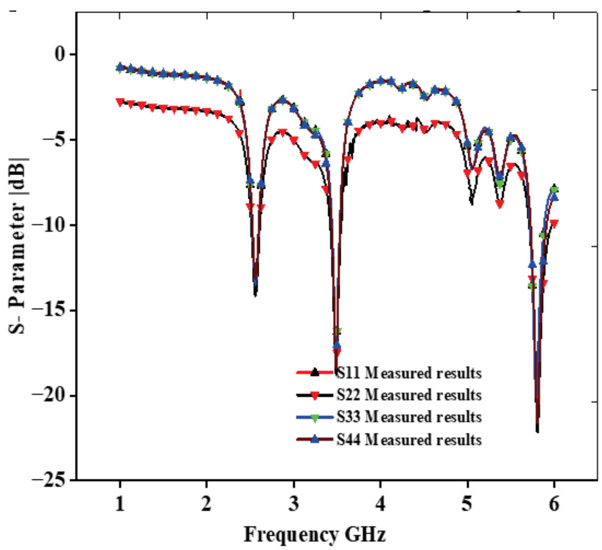

Fig. 4. Reflection coefficient without metamaterial.

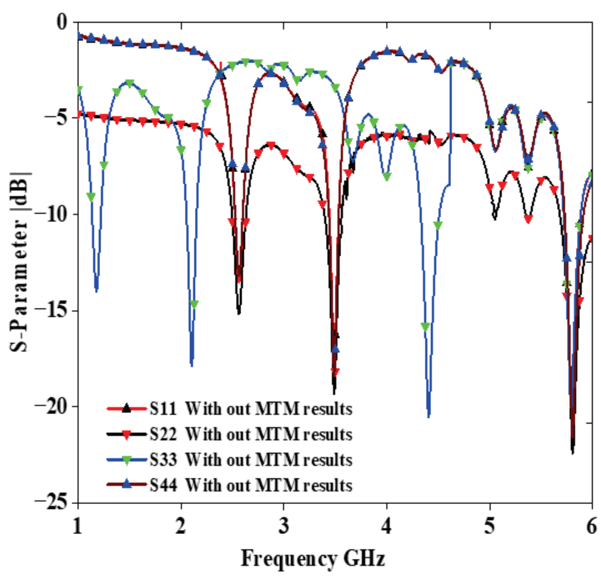

Fig. 5. Refection coefficient with metamaterial (MTM).

Figure 5 shows the simulation results of the reflection coefficientwithout using metamaterial.

The integration of unit cell design into a MIMO system improves the isolation between the antennas. The effects of near-field coupling between the antennas are lessened when the proposed metamaterial is positioned close to the MIMO system, as seen in the isolation plots in Fig. 6. In the 5G NR bands, isolation between the opposing antennas (S12/S21) and the nearby antennas (S31/S41) increases by at least 3.5 dB. Maximum volume is less than 20 decibels.

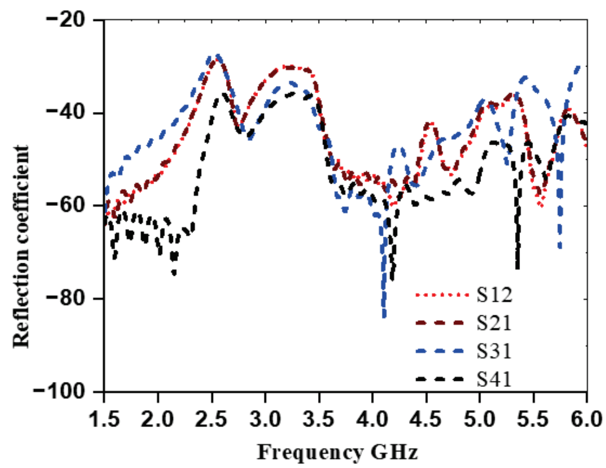

Fig. 6. Transmission coefficients.

III. UNIT CELL DESIGN

Since the primary goal of the metamaterial design is to access wideband 5G spectrums, the suggested structure's anticipated beginning dimensions are chosen to be at the frequency of 2.57 GHz, 3.5 GHz, and 5.8 GHz. At the intended frequencies of 2.57 to 5.8 GHz, the compact unit cell size (L) of 14 mm indicates $Lu = \lambda L/6.52$ (see Table 1). This is sufficiently tiny to meet the metamaterial sub-wavelength criterion, enabling the achievement of the metamaterial effective response.

Figure 7 shows that the unit cell design substrate is twenty micrometers thick on both sides. Characterizing materials in the low-GHz spectrum is another objective of the investigation. Because of this, the SRR dimensions are thought to have measurement applications at frequencies close to 6 GHz. In this instance, the exterior ring's length is $l = 20$ mm, the gap's width is $g = 1.5$ mm, the rings' width is $w = 20$ mm, and the distance between them is $c = 1.5$ mm. The geometrical layout of the SRR cell is displayed in Fig. 7, showing the low-cost, accessible proposed antenna aim of this project. With a dissipation factor of around 0.02 and a relative permittivity of $\varepsilon r = 4.4$, we select a FR-4 substrate thus. The copper metallic substrate has a thickness of 1.6 mm.

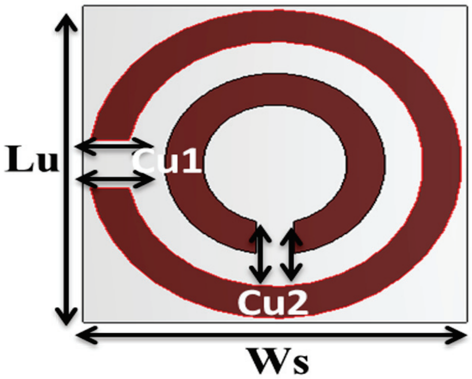

Fig. 7. SRR unit cell design.

Table 1: Unit cell parameters

S.No	Parameter	Value
1	Lu	20 mm
2	Ws	20 mm
3	Cut_1	1.5 mm
4	Cut_2	1.5 mm

A novel resonator with a modest size of 0.11λmin 0.02λmin at 3.4 GHz is produced utilizing 1.6 mm height low-cost FR-4 printed material (εr = 4.3 and tan δ = 0.025). Figure 8 depicts the optimized unit cell geometry, which consists of two linked circle-shaped complementary split rings enclosed by double rings. Figure 8 depicts metamaterial reflector design specs, an enlarged image of a unit cell, and a sneak peek at the finished prototype. An adaptive tetrahedral mesh-based frequency domain solution is used on the EM simulator platform, CST Studio Suite, to analyze the unit cell. During the simulation process, the electric and magnetic fields are parallel to the unit cell structure.

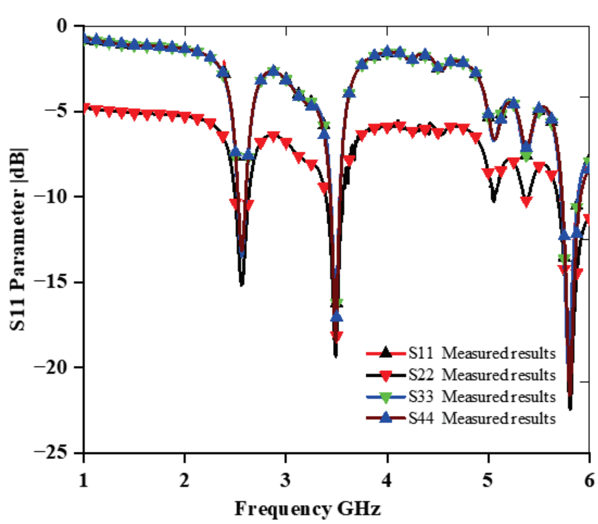

Fig. 8. Reflection coefficient measured results.

The produced MMR confirms the epsilon negative (ENG) and mu-near-zero (MNZ) properties by displaying a near-zero positive permeability value (actual) over the indicated antenna operating spectrum. This material's near-zero characteristics reduce the near-field coupling between magnetic and electric fields. The suggested antenna 4×4 compact design meets the condition modeling and measured results of the metamaterial structure employing a MIMO antenna.

In terms of technological merit, this approach has the following advantages over previous mutual decoupling techniques applied to MIMO antennas. The technique of integrating the SRR with metamaterial is proposed in this paper, wherein a circle stub design of structure operating at 2.57, 3.4, and 5.8 GHz is initially investigated, and then it is transformed into a metamaterial substance to further identify its mutual decoupling ability (see Table 2).

Table 2: Isolation from other antennas

Ref.	Size	Freq. Band (GHz)	Isolation (dB)
[1]	35×35	45629	≤20
[2]	38.5×38.5	3.08-11.08	≤20
[3]	48×48	2.5-12	15
[6]	30×35	2.78-12.3	-
[7]	55×100	1.85-11.9	≤17.2
[8]	23×39.8	45628	≤20
This work	70×65	2.57-5.8	≤23

1. An innovative SRR design that enhances impedance matching in MIMO antennas without utilizing any decoupling techniques suggests mutual coupling reduction.
2. Split-ring resonators optimize resonance frequency wireless applications with minimal radiative losses.
3. Reduced radiative losses of SRRs are a benefit. Their negative effective permeability at frequencies nearer the resonance frequency has led to the creation of left-handed media with a negative refractive index.
4. It is possible to convert this work into a low mutual coupling massive MIMO antenna since the edge-to-edge spacing between two selected antenna array parts can be as tiny as 0.037λ0.

IV. RESULTS AND DISCUSSION

For experimental examination, the constructed MIMO prototype is placed, as shown in Fig. 9, above the metamaterial reflector using two rings placed between the four antennas with 0.5 mm distance. During the reflection coefficient measuring technique, one to one antenna is activated. A 50 Ω terminator is used to close the remaining two ports while the two MIMO system antennas are activated concurrently for the isolation measurement.

Calculated and observed reflection coefficients (S11 and S22), with and without metamaterial structure, the planned MIMO systems show similar -15 dB impedance bandwidths. The 5G sub-6 GHz NR bands are still sufficiently covered, notwithstanding a little operational frequency modification brought on by metamaterial effects. After employing the metamaterial, the measured impedance for the originally intended MIMO antenna is BW 2.57 GHz (2.5-5.8 GHz). Simulated and observed isolation curves for the built-in MIMO antenna (with and without metamaterial), Fig. 10 shows antenna connected to VNA chamber to measure fabricated antenna.

Figure 11 shows the far-field results of the antenna as measured and simulated.

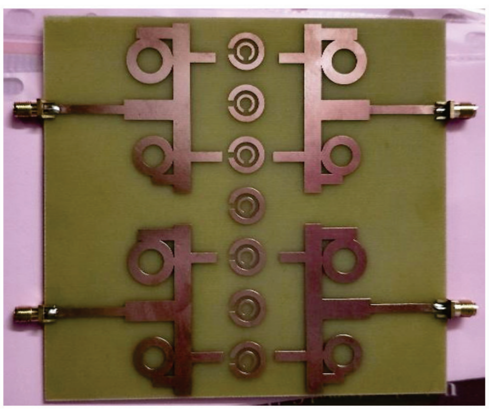

Fig. 9. Fabrication of the antenna.

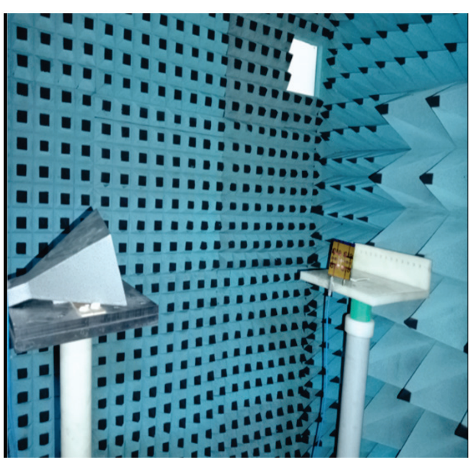

Fig. 10. Antenna connected to VNA chamber.

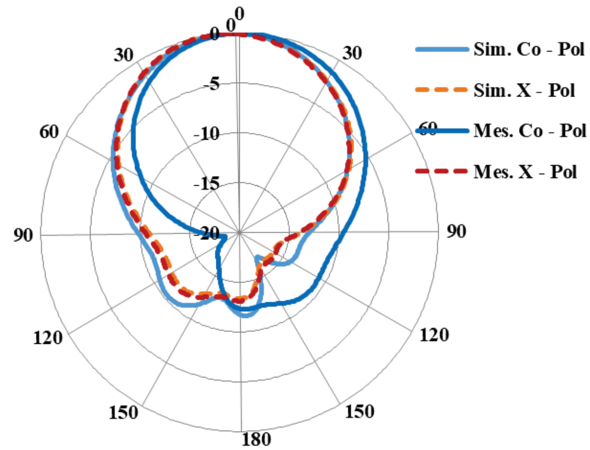

(a)

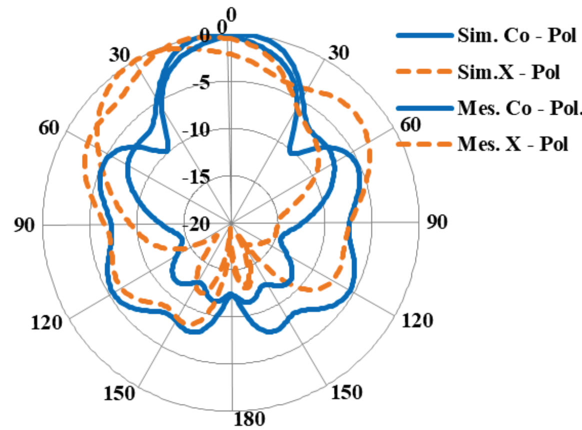

(b)

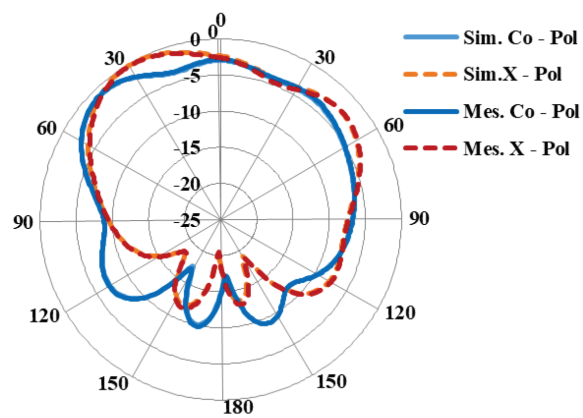

(c)

Fig. 11. (a) 2.57 GHz, (b) 3.4 GHz, and (c) 5.8 GHz normalized co- and cross-polarized radiation pattern simulated and measured results.

V. CONCLUSION

Here we present the four-port MIMO antenna for 5G and wireless applications and the created MIMO antenna, operating frequency ranges 2.57, 3.5 GHz to 5.8 GHz spectrum, covering the 5G NR n77/n78/n79 bands The wideband metamaterial reflector is added to the MIMO system to improve gain and isolation between two adjacent antenna radiators. The suggested antenna achieves a maximum gain of 8.1 dBi and an isolation of 20 dB, with a 4.2 dBi increase, demonstrating the metamaterial structural contribution to the specified MIMO system. After being made and tested, the suggested MIMO antenna experimental verification is good.

REFERENCES

[1] L. C. Tsai, "Design of triple-band T-U-shaped CPW-FED slot antennas," *Microw. Opt. Technol. Lett.*, vol. 56, no. 4, pp. 844-848, Apr. 2014.

[2] J. Park, M. Jeong, N. Hussain, S. Rhee, P. Kim, and N. Kim, "Design and fabrication of triple-band folded dipole antenna for GPS/DCS/WLAN/WiMAX applications," *Microw. Opt. Technol. Lett.*, vol. 61, no. 5, pp. 1328-1332, 2019.

[3] P. Wang, G. J. Wen, Y. J. Huang, and Y. H. Sun, "Compact CPW fed planar monopole antenna with distinct triple bands for WiFi/WiMAX applications," *Electron. Lett.*, vol. 48, no. 7, pp. 357-359, Nov. 2012.

[4] Y.-D. Wang, J.-H. Lu, and H.-M. Hsiao, "Novel design of semi-circular slot antenna with triple-band operation for WLAN/WIMAX communication," *Microw. Opt. Technol. Lett.*, vol. 50, no. 6, pp. 1531-1534, June 2008.

[5] H. Sakli, C. Abdelhamid, C. Essid, and N. Sakli, "Metamaterial-based antenna performance enhancement for MIMO system applications," *IEEE Access*, vol. 9, pp. 38546-38556, 2021.

[6] Z. Wang, W. Mu, M. Yang, and C. Li, "Design of compact multiband MIMO antenna based on ground neutralization line decoupling," *Applied Computational Electromagnetics Society (ACES) Journal*, vol. 37, no. 6, June 2022.

[7] S. Luo, Y. Li, C.-Y.-D. Sim, Y. Xia, and X. Liu, "MIMO antenna based on metamaterial frequency selective surface," *Applied Computational Electromagnetics Society (ACES) Journal*, vol. 36, no. 4, Apr. 2021.

[8] Y. Fan, J. Huang, T. Chang, and X. Liu, "A miniaturized four-element MIMO antenna with EBG for implantable medical devices," *Electromagn., RF and Microw. in Med. and Biol.*, vol. 2, no. 4, pp. 226-233, Dec. 2018.

[9] A. Iqbal, M. Al-Hasan, I. B. Mabrouk, and M. Nedil, "Scalp-implantable MIMO antenna for high-data-rate head implants," *IEEE Antennas Wireless Propag. Lett.*, vol. 20, no. 12, pp. 2529-2533, Dec. 2021.

[10] M. S. Singh, J. Ghosh, S. Ghosh, and A. Sarkhel, "Miniaturized dual-antenna system for implantable biotelemetry application," *IEEE Antennas and Wireless Propagation Letters*, vol. 20, no. 8, pp. 1394-1398, May 2021.

[11] S. M. A. Shah, M. Zada, J. Nasir, O. Owais, A. Iqbal, and H. Yoo, "Miniaturized four-port MIMO implantable antenna for high-data rate wireless-capsule-endoscopy applications," *IEEE Trans. Antennas Propag.*, vol. 71, no. 4, pp. 3123-3133, Mar. 2023.

[12] A. Iqbal, M. Al-Hasan, I. B. Mabrouk, and M. Nedil, "A compact implantable MIMO antenna for high-data-rate biotelemetry applications," *IEEE Trans. Antennas Propag.*, vol. 70, no. 1, pp. 631-640, Jan. 2022.

[13] Z. Xia, H. Li, Z. Lee, S. Xiao, W. Shao, and X. Ding, "A wideband circularly polarized implantable patch antenna for ISM band biomedical applications," *IEEE Trans. Antennas Propag.*, vol. 68, no. 3, pp. 2399-2404, Mar. 2020.

[14] R. Luomaniemi, J.-M. Hannula, R. Kormilainen, A. Lehtovuori, and V. Viikari, "Unbroken metal rim MIMO antenna utilizing antenna clusters," *IEEE Antennas Wireless Propag. Lett.*, vol. 18, no. 6, pp. 1071-1075, June 2019.

[15] A. Burger. *Nokia Claims 600 MHz LTE Equipment First* [Online]. Available: www.telecompetitor.com/nokia-claims-600-mhz-lte-equipment-first/

[16] C. A. Wieczorek, "600MHz spectrum access systems and methods," U.S. Patent 10 735 969 B2, 4 Aug. 2020.

[17] M. Rajakumar and M. Meena, "Compact tri-band loaded antenna for wireless communication and fifth generation applications," *Journal of Electrical Systems*, vol. 20, no. 6s, 2024.

[18] S. C. D. Barrio, G. F. Pedersen, and A. S. Morris, "Tunable multiple-resonance antenna systems, devices, and methods for handsets operating in low LTE bands with wide duplex spacing," U.S. Patent 10 541 475 B2, 21 Jan. 2020.

M. Rajakumar is a research scholar at Vels University Chennai. His area of research ismetamaterial antenna forwireless applications. He completed his masters in VLSID design.

M. Meena is Associate Professor, Department of ECE, Vels University, Chennai. She has published 27 papers in National and International Journals. She has six patents in the area of wireless networks.

An All-metal Antipodal Vivaldi Antenna Design for High-power Microwave Application

Zichong Chen, Rui Yin, Yun Jiang, Xiaojun Mao, Pengjie Lv, Shangyi Jiang, and Yang Liu

Department of Microwave Research
Hunan Vanguard Group Co. Ltd., Changsha 410137, China
czc0720@hnu.edu.cn, yinrui@861china.com, 867581306@qq.com, maoxiaojun@861china.com, lvpengjie@861china.com, jiangshangyi@861china.com, liuyang@861china.com

Abstract – In this paper, the evolutionary process, fabrication and measurement of an all-metal antipodal Vivaldi antenna (AMAVA) design are presented for the high-power microwave (HPM) application. Derived from the substrate-loaded antipodal Vivaldi antenna, the proposed antenna is made all metallic to enhance its power handling capacity (PHC). Considering the further improvement of the radiation performance and antenna fixing, rectangular slots and tuning stubs with exponential corner cuts are employed in antenna design. In the air condition, the PHC values of the final proposed antenna are over 8000 W in its operating band. The proposed AMAVA is fabricated and measured in a microwave anechoic chamber. According to the measured results, the −10 dB impedance bandwidth covers 8.3-10.66 GHz, and its deepest resonance reaches −29.7 dB at 9.75 GHz. The measured radiation pattern values are in agreement with simulation values, and its peak gain values at 9.3 GHz, 9.8 GHz and 10.3 GHz are 4.54 dBi, 5.68 dBi and 5.71 dBi, respectively. A PHC experiment is conducted, which verifies the AMAVA is qualified for 8000 W-level PHC.

Index Terms – All-metal antenna, antipodal Vivaldi antenna (AVA), high-power microwave (HPM) antenna, power handling capacity (PHC).

I. INTRODUCTION

Unmanned aerial vehicle (UAV) technology and industry have been greatly improving and developing in recent years. As one of the directional energy technologies, high-power microwave (HPM) technology has been taken much into account for anti-UAV swarms and has obtained a significant effect in the practice. The HPM antenna, as the energy-radiating terminal, plays an important role in the HPM system to realize adequate energy to damage or destroy the target aircraft.

Printed on the same side of the dielectric substrate, the Vivaldi antenna (VA) is designed with specialized exponential slots, which transform small size to large size in order to realize an ultra-wideband [1, 2]. Great efforts for VA research are made into gain enhancement [3–5], antenna miniaturization [2, 6], notch band [8], dual polarization [9], circular polarization [2, 10] and array design [12]. Involving two flares with exponential slots printed on two sides of the substrate, antipodal Vivaldi antennas (AVA) have the advantages of a stable realized gain and compact structure, which is widely applied in wireless communication and radar detection [13]. Similarly, the AVA design mainly focuses on the topic of using metamaterials to enhance the realized gain for ultra-wideband applications [14], moisture sensors for industrial process control [15], monitoring liver microwave thermal ablation for microwave imaging systems [16] and near-field microwave imaging medical applications [17].

However, the common sub-loaded VA cannot be applied in the HPM systems due to its low power handling capacity (PHC), usually no more than 3000 W in the air. One of the most effective ways to enhance the PHC is making the Vivaldi antenna all metallic (AMVA). With inclined groove and orthogonal element, respectively, AMVA units are designed in [2, 18] for ultra-wideband dual-polarization applications. Based on the AMVA unit design, a linear phase array is proposed with eight elements, and two additional elements added as the virtual elements, realizing a broadband characteristic of 6-12 GHz and the phase scanning of a 45° angle [20]. Most given attention is emphasis on the AMVA array design, which involves a dual-polarization array for the HPM systems [2, 21], a flared-notch array [23], a dual-polarized array for airborne radar measurements of snow [24] and an array operating in 12 octaves [25].

This paper proposes and verifies an all-metal antipodal Vivaldi antenna (AMAVA) for HPM applications. By using an all-metal structure rather than the traditional substrate-loaded frame, two AVA flares are positioned vertically on the metallic plate, improving its PHC while maintaining its broadband characteristics. The proposed AMAVA has a PHC of more than 8000 W and a −10 dB

Submitted On: August 9, 2024
Accepted On: January 5, 2025
https://doi.org/10.13052/2024.ACES.J.391205

impedance bandwidth of 8.37-10.6 GHz, which demonstrates its ability in applying in the HPM system.

II. ANTENNA DESIGN

A. Evolution process and antenna specification

The AMAVA design is modeled, simulated and optimized in the Computer Simulation Technology (CST) Studio Suite 2021. The evolution process, detailed structure and dimension of the proposed antenna design are presented in Figs. 1 (a-d). At first, an AVA loaded on an FR-4 substrate ($\varepsilon_r = 4.4$) is regarded as the original antenna (*Ant I*). To enhance the PHC of the antenna, *Ant I* is made all-metallic as *Ant II*, whose one flare connects to a metallic ground plate, which helps to improve the directivity of the AMAVA, and another is fed by a coaxial probe. The chiral flares are set parallel and crossed. To further improve the performance of the AMAVA, some modifications are employed on the flares. The proposed AMAVA consists of two chiral metallic exponential radiation flares with rectangular slots to realize the broadband characteristic, a metal plate for grounding and a 50 Ω coaxial probe for feeding. The exponential curve of the AMAVA is, according to $y = ae^{(r*x)}+b$, a total of four exponential curves included in the proposed antenna design.

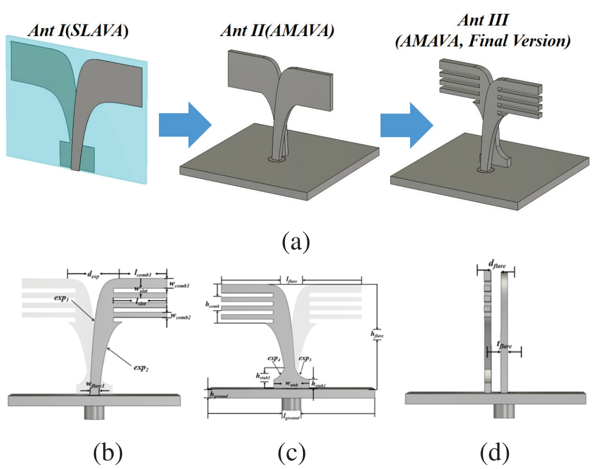

Fig. 1. Diagram of the proposed antenna: (a) evolution process of the SLAVA to the enhanced AMAVA, (b) flare fed by the coaxial probe, (c) flare connected with the ground, and (d) side view ($l_{comb1} = 9.5$ mm, $w_{comb1} = 2$ mm, $w_{slot} = 0.93$ mm, $l_{slot} = 11$ mm, $w_{comb2} = 1.1$ mm, $w_{flare1} = 1.9$ mm, $d_{exp} = 11.6$ mm, $l_{ground} = 35$ mm, $h_{ground} = 2$ mm, $h_{stub1} = 5.2$ mm, $h_{stub2} = 2$ mm, $w_{stub} = 7.6$ mm, $l_{flare} = 30.2$ mm, $h_{flare} = 24$ mm, $h_{comb} = 9$ mm, $d_{flare} = 1.9$ mm, $t_{flare} = 1.8$ mm, $r_1 = -0.6$, $r_2 = -0.95$, $r_3 = r_4 = -0.87$, $a_1 = -28$, $b_1 = 16$, $a_2 = -10$, $b_2 = 24$, $a_3 = 11.6$, $b_3 = 1.6$, $a_4 = 5.3$, $b_4 = 1.8$).

B. Simulated performances at different states

Comparisons of simulated results among the three antennas are shown in Figs. 2 (a-b). According to the PHC calculating method:

$$PHC = P_{in} * \left(\frac{E_{\text{air}}}{E_{\max}}\right)^2. \tag{1}$$

Input power P_{in} is 0.5 W, breakdown E-field intensity E_{air} in the air is 3 MV/m and $E_{\max}$ is the maximum E-field intensity. It is obvious that lowering the value of $E_{\max}$ is helpful to increase PHC. The simulated PHC values of *Ant I* are no more than 1000 W and cannot satisfy the basic demand of the HPM system. For the purpose of enhancing the PHC of the AVA, *Ant II* is a version of the all-metallic *Ant I*, whose simulated PHC values are improved significantly and over 8000 W in the operating band. However, the operating bandwidth and resonance depth of *Ant II* are narrow and shallow due to the all-metal structure. The deepest resonance depth is −15.5 dB at 9.8 GHz, and the −10 dB impedance bandwidth of *Ant II* covers 8.25-11.1 GHz. The shallow resonance depth of *Ant II* has the potential to influence the electric components, such as the low-noise amplifier. Considering this issue, with slots on the brims of the Vivaldi flares, some bandwidths are sacrificed to ensure enough resonance depth. The simulated −10 dB impedance bandwidth of *Ant III* can cover 8.62-10.66 GHz, and its deepest resonance depth can reach −29.5 dB at 9.8 GHz. Introducing slots, the E-field distributions of the AMAVA are changed, and its maximum E-field intensity is reduced, resulting in some improvements in simulated PHC at target frequencies according to equation (1).

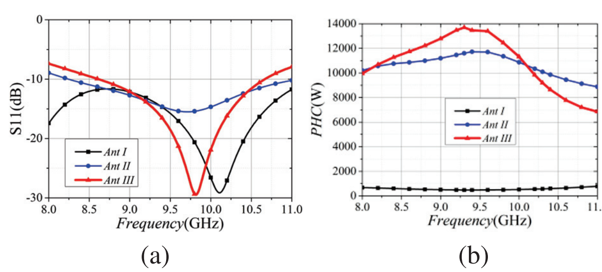

Fig. 2. Comparison among simulated results of *Ant I*, *Ant II* and *Ant III* (a) S11 and (b) PHC.

Comparisons of the simulated radiation patterns of the three antennas are listed in Figs. 3 (a-b). E-plane and H-plane radiation patterns of *Ant I* show great symmetry and are close to the shapes of '8' and '0', respectively. The antenna will be arranged in an array for the HPM radiation, and the back lobe of *Ant I* is too noticeable and will lead to strong back radiation, which has the potential to destroy irrelevant electrical components in the back end, so that it cannot apply in the HPM application. For some antenna arrays, they are examined for a certain angular deflection, so that the main lobe of the element antenna does not travel along the axis. When the original antenna undergoes metallization and transits to *Ant II* and *Ant III*, the radiation direction of *E*-plane patterns will deviate 7-8° from the main axis, and an asymmetry shows in *E*-plane and *H*-plane radiation patterns in the operating band. Thanks to the loading of the ground plane in *Ant II* and *Ant III* designs, their back radiation lobes are nearly eliminated and facilitation of antenna fixing is obtained.

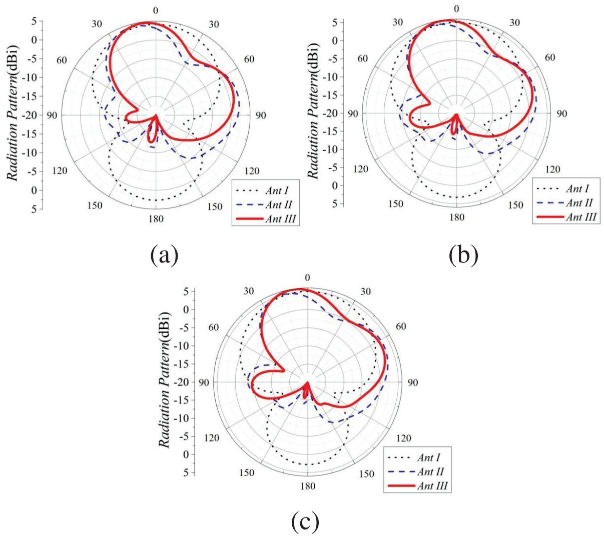

Fig. 3. Simulated *E*-plane radiation patterns of *Ant I*, *Ant II* and *Ant III* at (a) 9.3 GHz, (b) 9.8 GHz, and (c) 10.3 GHz.

C. Parameter study

A detailed optimum process of AMAVA will be presented in this section. First, an analysis of antenna performance will be given from the aspect of the structure of AMAVA itself. The thickness of the flare as well as the width of the flare is considered a significant parameter to influence impedance match and PHC. On the one hand, the size of the coaxial probe and the dielectric material restricts the thickness of the flare, so that the thickness of the flare and the width of the flare should be between them (1.27-4.1 mm). Once out of this range, the bottom of the flare will be punctured or a short circuit will occur. On the other hand, satisfying simulated results are obtained when $t_{flare} = 1.8\ mm$, as depicted in Figs. 4 (a-b).

As shown in Figs. 5 (a-b), the width of the AMAVA flare connected to the ground plane affects impedance match and PHC. When w_{flare1} increases from 1.4 mm to 2.4 mm, the resonance point will deviate and deepen, while PHC values in the operating band emerge with an opposite tendency. Therefore, the middle value of 1.9 mm is considered the optimum parameter for w_{flare1}.

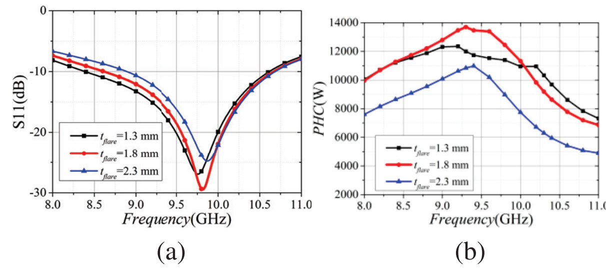

Fig. 4. Simulated results corresponding to different flare thickness values t_{flare} (a) S11 and (b) PHC.

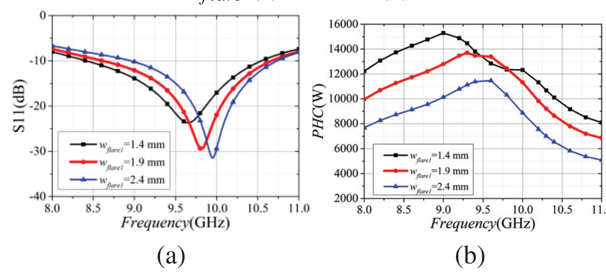

Fig. 5. Simulated results corresponding to different width values of the flare w_{flare1} (a) S11 and (b) PHC.

Meanwhile, it is exerting a great influence on the S11 and PHC of the AMAVA presented in Figs. 6 (a-b) for the distance between two flares. The simulated S11 deviates left and shallows with d_{flare} increases. When $d_{flare} = 1.9\ mm$ and 2.4 mm, PHC values remain relatively stable. PHC values go down rapidly in the main operating band when d_{flare} goes to 1.4 mm.

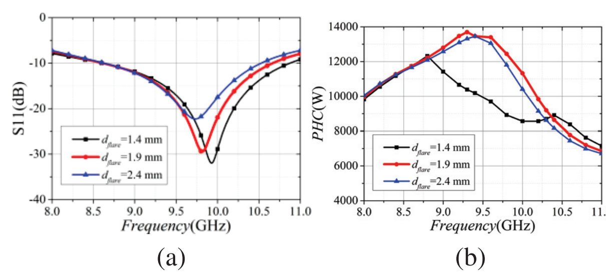

Fig. 6. Simulated results corresponding to different distance values between the two flares d_{flare} (a) S11 and (b) PHC.

To further enhance the ability of AMAVA, a rectangular tuning stub with exponential corner cuts is loaded on the bottom of the flare, which connects with the ground plane. In Figs. 7 (a-b), simulated resonance goes deeper when h_{stub1} increases. As for PHC value, it reaches its peak when $h_{stub1} = 5.2\ mm$.

Rectangular slots are employed on the flare of the AMAVA, and its influence on the antenna performance is depicted in Figs. 8 (a-b). With l_{slot} and w_{slot} increasing, the resonance depth and magnitude of the PHC are greatly improved due to the comb-like flare structure.

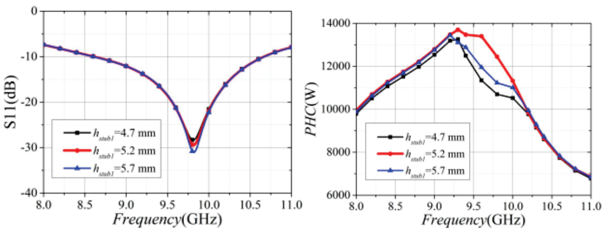

(a) (b)

Fig. 7. Simulated results corresponding to different height of stub values h_{stub2} (a) return loss and (b) PHC.

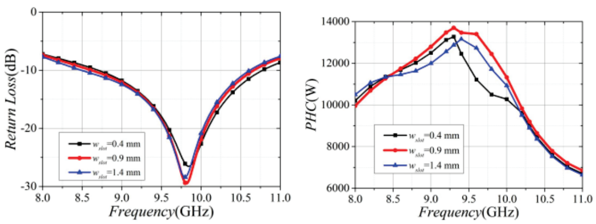

(a) (b)

Fig. 8. Simulated return loss results corresponding to different value lengths of the slot l_{slot}.

III. FABRICATION AND VERIFICATION

The prototype of the proposed antenna, which consists of two Vivaldi comb-like flares, an SMA ensuring HPM and a rectangular ground plate, is shown in Figs. 9 (a-b). Aluminum is selected as the metallic material for its light weight, low cost and durability in the HPM application. An SMA connector SMA-KFD3-1, manufactured by Gwave Technology Co. Ltd., which has an eligible PHC, is employed in the fabrication of AMAVA. The feed probe punctures through the ground plate and connects to the bottom of the Vivaldi comb-like flare. The outer dielectric material of the SMA inserts into the ground plate, on whose back the flange fixes the whole antenna design.

In Fig. 10, the measured and simulated S11 results are depicted and show a satisfying agreement. The measured S11 of the AMAVA covers 8.3-10.66 GHz, which is wider at low frequencies than that in the simulation, and its deepest resonance over frequency reaches −29.7 dB at 9.75 GHz.

The measured and simulated radiation patterns at three frequency points of the AMAVA are presented in Fig. 11. For E-plane radiation patterns, the measured values and their variation tendency are in good agreement with the simulation. The deviations of maximum radiation direction are between 7° and 8°, and the peak realized gain values are 4.54 dBi, 5.68 dBi and 5.71 dBi at 9.3 GHz, 9.8 GHz and 10.3 GHz, respectively. Levels of the measured back lobes are 2 dBi higher than the simulated results. As for the H-plane, the symmetry of measured radiation patterns keeps stable, while measured beamwidths are narrower than simulation beamwidths at selected frequencies.

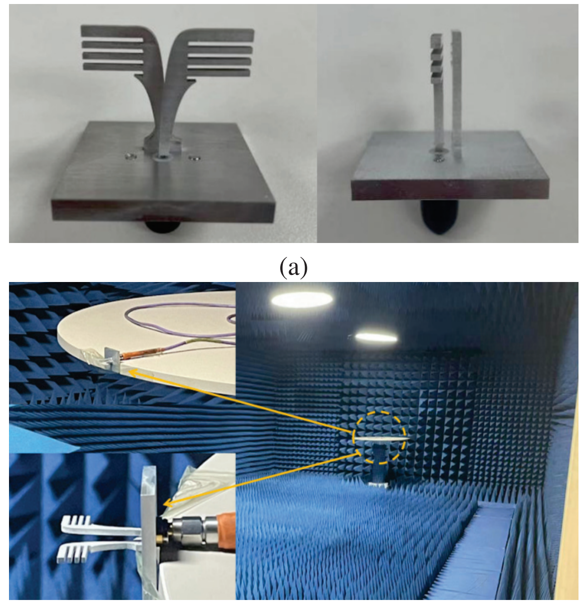

(a)

(b)

Fig. 9. Prototype of AMAVA (a) front view and side view and (b) in the anechoic chamber.

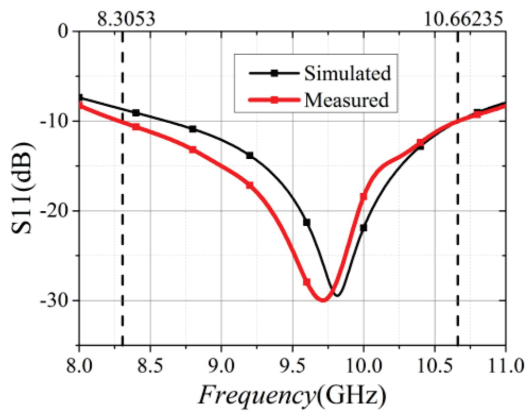

Fig. 10. Measured and simulated S11 results of AMAVA.

To verify the PHC of the proposed antenna, an HPM experiment involving two of the same AMAVAs (No. 1 and No. 2) measured at 9 GHz will be conducted as shown in Fig. 12. One proposed antenna is fed by an HPM source of 8000 W as a transmitting antenna, and the other one, as a receiving antenna, is connected through a 20 dB attenuator to a signal analyzer, which monitors and records the operating status of the HPM system. To test whether AMAVA can bear the PHC of 8000 W-level, the curve on the signal analyzer should be observed while the HPM source is on. If the curve remains stable for 10 minutes, AMAVA is

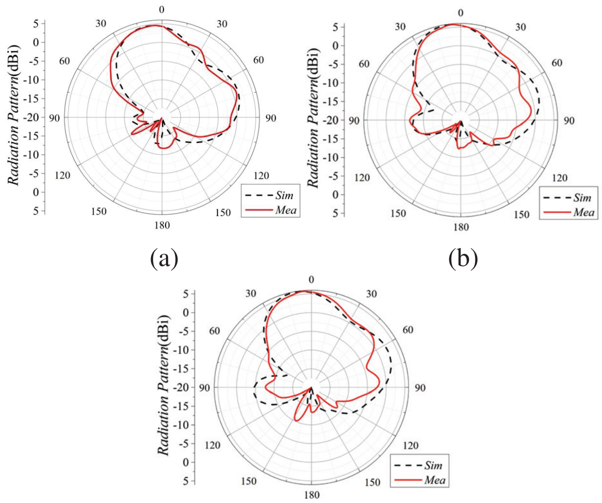

(a) (b) (c)

Fig. 11. Measured and simulated *E*-plane radiation patterns of AMAVA at (a) 9.3 GHz, (b) 9.8 GHz and (c) 10.3 GHz.

deemed qualified with the PHC of 8000 W level. If the curve changes greatly, the proposed antenna cannot be applied in the HPM system. Figure 13 and Table 1 depict the measured result on the signal analyzer at 9 GHz. The measured peak values of the AMAVA design on the signal analyzer are −2.31 dBm and −2.32 dBm, respectively. Exchanging the transmitting and the receiving antenna, the measured peak values in the second experiment are −2.28 dBm and remain unchanged. The measured results demonstrate the proposed antenna is qualified with 8000 W-level PHC, which shows its ability in the HPM system.

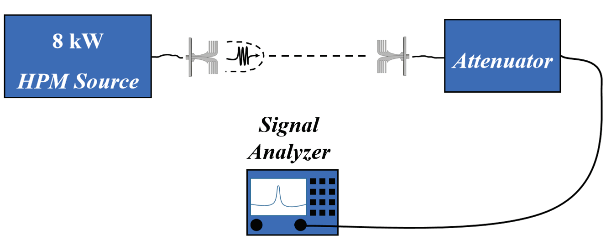

Fig. 12. Diagram of the PHC experiment.

Table 1: Measured peak values of AMAVA

	0 min	**10 min**
No.1	−2.31 dBm	−2.32 dBm
No.2	−2.28 dBm	−2.28 dBm

For a better understanding of the AMAVA design, a comparison with public VA designs is listed in Table 2, showing their characteristics in terms of antenna type,

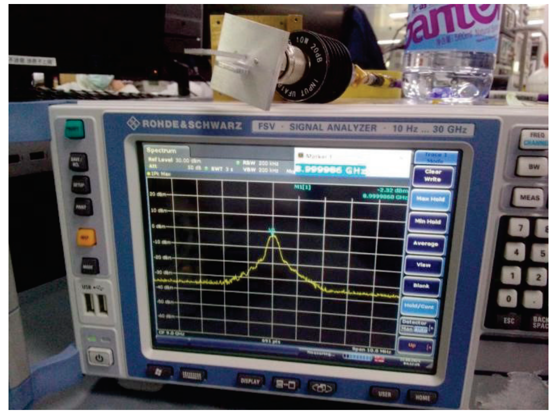

Fig. 13. Measured results on the signal analyzer at 9 GHz.

Table 2: Comparison of the AMAVA with public VAs

Ref	Type	Size	Bandwidth	Application
This work	**AMAVA**	**$0.87\lambda_0 \times 0.69\lambda_0$**	**8.3-10.7 GHz**	**HPM**
[14]	Sub-AVA	$0.87\lambda_0 \times 0.4\lambda_0$	1-28 GHz	UWB
[15]	Sub-AVA	$2\lambda_0 \times 0.8\lambda_0$	6-12 GHz	Moisture Sensor
[16]	Sub-AVA	$0.13\lambda_0 \times 0.08\lambda_0$	0.6-3 GHz	Microwave Imaging System
[17]	Sub-AVA	$0.75\lambda_0 \times 0.75\lambda_0$	1.5-3.3 GHz	Microwave Imaging System
[18]	AMVA	$0.53\lambda_0 \times 0.4\lambda_0$	2-50 GHz	UWB
[19]	AMVA	$0.32\lambda_0 \times 0.3\lambda_0$	2-6 GHz	Wireless Comm
[20]	AMVA	$3\lambda_0 \times 0.7\lambda_0$	6-12 GHz	Phased Array
[21] [22]	AMVA	$2.4\lambda_0 \times 0.6\lambda_0$	2-6 GHz	HPM
[23]	AMVA	$0.61\lambda_0 \times 0.33\lambda_0$	8-12 GHz	Radar
[24]	AMVA	$0.69\lambda_0 \times 0.09\lambda_0$	2-18 GHz	Radar
[25]	AMVA	$0.4\lambda_0 \times 0.06\lambda_0$	2.6-21.2 GHz	UWB

dimension, operating band and application. VA designs in [14–17] are AVA on the substrate with wideband characteristic. However, the PHC values of the VA designs loaded on the PCB are unqualified for the HPM systems. With a measured PHC of more than 8000 W, the proposed antenna design in this letter is appropriate for use in the HPM systems. References [18–25] are metallizing VA designs, among which that in [22] is applied for the HPM systems, and its simulated maximum *E*-field intensity is mentioned. According to equation (1), the PHC value of the VA design in [22] is 471 kW at 4 GHz. In general, the larger the microwave component, the lower the maximum *E*-field intensity (the higher the PHC). The size of a microwave component is in direct proportion to its lowest operating frequency. Therefore, working at lower frequencies and having a larger size, the proposed VA design in [22] is made to have a higher PHC compared to the AMAVA proposed in this paper.

IV. CONCLUSION

To solve the inability of the sub-loaded AVA for the HPM application, an all-metal antipodal antenna is proposed, designed and verified in this paper. Making the radiation flare all metallic, the PHC of the AMAVA is much improved. Rectangular tuning stub and slot are loaded on the antenna design, whose resonance depth and maximum PHC value are further enhanced. The prototype of the proposed antenna is fabricated and verified in the anechoic chamber, and its measured results are in good agreement with simulations. An 8000 W-level PHC experiment is conducted at 9 GHz, certifying the potential of AMAVA in the HPM systems. Consistent efforts will be made in terms of antenna miniaturization, cross-polarization optimization and bandwidth expansion in the future.

ACKNOWLEDGMENT

This work is supported by the Hunan science and technology project (outstanding science and technology innovative youth) under Grant 2023RC3266.

REFERENCES

[1] A. Bhattacharjee, A. Bhawal, A. Karmakar, and A. Saha, "Vivaldi antennas: A historical review and current state of art," *International Journal of Microwave and Wireless Technologies,* vol. 13, pp. 833-850, 2021.

[2] B. Wu, X.-Y. Sun, H.-R. Zu, and H.-H. Zhang, "Transparent ultrawideband halved coplanar Vivaldi antenna with metal mesh film," *IEEE Antennas Wireless Propag. Lett*., vol. 21, no. 12, pp. 2532-2536, 2022.

[3] S. Ramesh and T. Rama Rao, "High gain dielectric loaded exponentially tapered slot antenna based on substrate integrate waveguide for V-band wireless communications," *Applied Computation Electromagnetics Society (ACES) Journal*, vol. 29, no. 11, pp. 870-880, Nov. 2014.

[4] H. Lv, Q. Huang, J. Hou, and J. Liu, "Wideband dual-polarized Vivaldi antenna with gain enhancement," *Applied Computation Electromagnetics Society (ACES) Journal*, vol. 33, no. 9, pp. 990-996, Sep. 2018.

[5] H. Zhu, X. Li, L. Yao, and J. Xiao, "A novel dielectric loaded Vivaldi antenna with improved radiation characteristics for UWB application," *Applied Computation Electromagnetics Society (ACES) Journal*, vol. 33, no. 4, pp. 394-399, Apr. 2018.

[6] S. Pan, W. Shen, Y. Feng, and Z. Liu, "Miniaturization and performance enhancement of Vivaldi antenna based on ultra-wideband metasurface lens," *Int. J. Electron. Commun.,* vol. 134, pp. 1-7, 2021.

[7] A. Hossain and A.-V. Pham, "A novel gain-enhanced miniaturized and lightweight Vivaldi antenna," *IEEE Trans. Antennas Propag*., vol. 71, no. 12, pp. 9431-9439, 2023.

[8] H. Qi and H. Liu, "Single-ended band-notched Vivaldi antenna with common mode suppression and low cross polarization," *IEEE Antennas Wireless Propag. Lett*., vol. 20, no. 10, pp. 1983-1987, 2021.

[9] K. Zhang, R. Tan, Z. H. Jiang, Y. Huang, and L. Tang, "A compact, ultrawideband dual-polarized Vivaldi antenna with radar cross section reduction," *IEEE Antennas Wireless Propag. Lett*., vol. 21, no. 7, pp. 1323-1327, 2022.

[10] X. Liu, Y. Zhu, and W. Xie, "A miniaturized wide-band directional circularly polarized antenna based on bent Vivaldi antenna structure," *IEEE Antennas Wireless Propag. Lett*., vol. 22, no. 2, pp. 298-302, 2023.

[11] J. Liang, C. Chiu, T. Lin, and C. Lee, "An ultrawideband circularly-polarized Vivaldi antenna with high gain," *IEEE Access*, vol. 10, pp. 100446-100455, 2022.

[12] T. Zhang, Y. Chen, Z. Liu, and S. Yang, "A low-scattering Vivaldi antenna array with slits on nonradiating edges," *IEEE Trans. Antennas Propag*., vol. 71, no. 2, pp. 1999-2004, 2023.

[13] F. Gunes, I. O. Evranos, M. A. Belen, and P. Mahouti, "A compact triband antipodal Vivaldi antenna with frequency selective surface inspired director for IoT/WLAN applications," *Wireless Networks*, vol. 27, pp. 3195-3205, 2021.

[14] X. Shi, Y. Cao, Y. Hu, and X. Luo, "A high-gain antipodal Vivaldi antenna with director and metamaterial at 1-28 GHz," *IEEE Antennas Wireless Propag. Lett*., vol. 20, no. 12, pp. 2432-2436, 2021.

[15] F. Stern, W. Taute, R. Knöchel, and M. Höft, "Dual antipodal Vivaldi antenna-based moisture sensor for industrial process control," *IEEE Sensors Journal*, vol. 23, no. 19, pp. 22430-22439, 2023.

[16] M. Wang, L. Crocco, S. Costanzo, and R. Scapaticci, "A compact slot-loaded antipodal Vivaldi antenna for a microwave imaging system to monitor liver microwave thermal ablation," *IEEE Open Journal of Antennas and Propagation*, vol. 3, pp. 700-708, 2022.

[17] A. M. de Oliveira, A. M. de Oliveira Neto, M. B. Perotoni, and N. Nurhayati, "A fern antipodal Vivaldi antenna for near-field microwave imaging medical applications," *IEEE Trans. Antennas Propag*., vol. 69, no. 12, pp. 8816-8829, 2021.

[18] C. Zhao, Y. Bai, and Q. Wei, "A 2 to 50 GHz all-metal Vivaldi antenna for ultra-wideband (UWB)

application," *Int. J. Electron. Commun.,* vol. 148, pp. 1-6, 2022.
[19] Y. Chuo, L. Ziting, L. Qiang, and D. Haosheng, "Design of a metal Vivaldi antenna with wide band and dual polarization," in *2021 IEEE International Workshop on Electromagnetics: Applications and Student Innovation Competition (iWEM)*, Guangzhou, China, pp. 1-3, 2021.
[20] X. Ma, S. Chai, K. Xiao, and L. Ding, "Design of all-metal Vivaldi phased array antenna," in *2018 IEEE 3rd International Conference on Signal and Image Processing (ICSIP)*, Shenzhen, China, pp. 547-551, 2018.
[21] T. H. Lim, S. Park, C. S. Lee, and J.-R. Park, "A broadband dual-slant polarized metal Vivaldi antenna for a high-power jammer," in *2020 International Symposium in Antennas and Propagation (ISAP)*, Osaka, Japan, pp. 485-486, 2021.
[22] S. Ohm, E. Kang, T. H. Lim, and H. Choo, "Design of a dual-polarization all-metal Vivaldi array antenna using a metal 3D printing method for high-power jamming systems," *IEEE Access*, vol. 11, pp. 35175-35181, 2023.
[23] R. W. Kindt and W. R. Pickles, "Ultrawideband all-metal flared-notch array radiator," *IEEE Trans Antennas Propag.,* vol. 58, no. 11, pp. 3568-3575, 2010.
[24] J.-B. Yan, S. Gogineni, B. Camps-Raga, and J. A. Brozena, "A dual-polarized 2-18-GHz Vivaldi array for airborne radar measurements of snow," *IEEE Trans Antennas Propag.,* vol. 64, no. 2, pp. 781-785, 2016.
[25] R. W. Kindt and R. Pickles, "12-to-1 bandwidth all-metal Vivaldi array element," in *IEEE Antennas Propagation Symp*., pp. 1-4, 1-5 June 2009.

Zichong Chen received the M.E. degree from Hunan University in 2023. He works full-time as a microwave engineer for Hunan Vanguard Group Co. Ltd. His research interests include HPM antenna, flexible antenna and UWB antenna design.

Rui Yin received the M.E. degree from Nanjing University of Science and Technology in 2018. She works full-time as a microwave engineer at Hunan Vanguard Group Co. Ltd. Her current research interests include HPM antenna and high-performance microwave circuits.

Yun Jiang received the Ph.D. degree from National University of Defense Technology in 2022. He works full-time as a senior microwave engineer at Hunan Vanguard Group Co. Ltd. His current research interests include HPM overall system design, microwave RF circuit and radar technology.

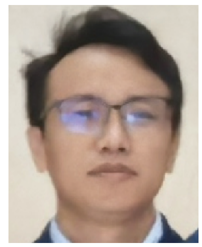

Xiaojun Mao received the Ph.D. degree from Harbin Engineering University in 2017. He works full-time as a senior microwave engineer at Hunan Vanguard Group Co. Ltd. His current research interests include the HPM overall system design, antenna array algorithm and radar technology.

Pengjie Lv received the M.E. degree from Shenyang University of Science and Technology in 2009. He works full-time as a microwave engineer at Hunan Vanguard Group Co. Ltd. His current research interests include HPM overall system design.

Shangyi Jiang received the M.E. degree from Nanjing University of Science and Technology in 2023. He works full-time as a microwave engineer at Hunan Vanguard Group Co. Ltd. His current research interests include HPM source design and electromagnetic compatibility.

Yang Liu received the B.E degree from Changsha University of Science and Technology in 2020. He works full-time as a microwave engineer at Hunan Vanguard Group Co. Ltd. His current research interests include HPM antenna and damage effect.

Design of a Single-fed Gain-enhanced Circularly Polarized Patch Antenna for Microwave Power Transmission

Ziyang Jiang[1], Zhonghua Ma[1,2*], Xiaojing Sun[1,2], Weiqian Liang[1], and Haitao Xing[1]

[1]School of Marine Information Engineering
Jimei University, Xiamen 361021, China
202121303012@jmu.edu.cn, *mzhxm@jmu.edu.cn, 202321303042@jmu.edu.cn,
liangwq@jmu.edu.cn, xht2005@jmu.edu.cn,

[2]National Research and Development Center for Eel Processing Technology
Key Laboratory of Eel Aquaculture and Processing of Fujian Province, Fujian Provincial Engineering Research Center for Eel Processing Enterprise, Fuzhou, 350200, China,

***Abstract* –** A high-gain single-fed circularly polarized (CP) microstrip patch antenna for microwave transmission systems is proposed in this paper. Two narrow rectangular slots are added to the rectangular microstrip patch to enhance the antenna gain. The patch is rotated by 90° to form a cross microstrip patch antenna, and a pair of narrow microstrip strips are added at the edge of the cross patch along the -45° diagonal direction of the antenna to implement circular polarization. Two short rectangular microstrip lines are added on both sides of the narrow microstrips to adjust the phase of the current to further reduce the axial ratio (AR) value. The designed antenna model is simulated, fabricated and measured. The results of the measurement show that the antenna has a gain of 11.3 dB at the resonance frequency of 5.8 GHz, and the CP AR is 2.73 dB. The antenna can be applied to microwave power transmission systems and other personal wireless communication systems.

***Index Terms* –** Axial ratio, circular polarization, gain enhancement, single-fed.

I. INTRODUCTION

With the development of science and technology, microwave power transmission (MPT) technology has attracted the attention of engineers and researchers. As the ”virtual battery” of microsystems, microwave energy transmission technology brings much convenience to work and life. A microwave energy transmission system is mainly composed of three parts: microwave transmission system, microwave transmission channel and microwave receiving system. The antenna is the key device of signal transmitting and receiving in microwave transmission system. In order to get higher power transmitting efficiency, the high gain circular polarized microstrip patch antenna is a very attractive choice.

In order to increase the distance of wireless transmission of electrical energy and the power of the transmitted electrical energy, it is necessary to transmit and receive electrical energy wirelessly with a high gain antenna. Microstrip antennas have low gain compared to horn antennas, and it is necessary to use gain enhancement techniques to improve the gain of the antenna. In addition to the traditional array design method, the gain enhancement of the antenna can also be improved by adding parasitic patches, multi-layer substrate structure and adding slots on the microstrip patch [1–4]. Cao et al. proposed to generate a new resonance mode by adding parasitic patches on the two radiating edges of the main radiating patch. The combination of the new resonant mode and the original resonant mode realizes broadband high gain performance [1]. Zhang et al. reconstructed the surface current distribution on the microstrip resonator by introducing a horizontal slot in the center of the square microstrip patch to achieve gain enhancement [2]. Hong et al. added narrow rectangular slots on the edge of the circular patch antenna to change the distribution of the reverse current, making the current distribution more consistent [3]. This operation reduced the mutual interference between the reverse current and the co-directional current in the far-field region of the antenna and enhanced the radiation of the current in the x-axis direction, thereby increasing the gain of the antenna. In [4], four short-circuit pins are placed symmetrically on the two diagonals of a square patch antenna. Due to the shunt inductance effect, these shorting pins affect the field distribution below the patch, thus improving the antenna gain.

In addition to this, there are novel designs to enhance the gain of the antenna. For example, an artificial magnetic conductor antenna with a hexagonal annular slot loaded on the ground was reported in [5]. Gain

Submitted On: August 22, 2024
Accepted On: December 19, 2024
https://doi.org/10.13052/2024.ACES.J.391206

enhancement and low profile are achieved by adjusting the distance between the patch antenna and the ground at zero phase reflection frequency. Reference [6] proposes folding the ground plane at the non-radiating edge of the patch antenna to enhance the gain of the antenna without affecting the bandwidth of the original antenna. In [5–6], both realize the gain enhancement of the antenna by adding the design only on the ground plane, although there is the problem of large volume of space occupied by the antenna, which is not conducive to the integration of the antenna.

Line-polarized (LP) antennas used in MPT require strict polarization alignment of the transmitting and receiving antennas, otherwise polarization loss will be produced and the efficiency of power transmission will be reduced. Moreover, for mobile terminals, due to the random change of their position and direction, LP antennas have fatal defects for mobile terminals. In MPT systems, circularly polarized (CP) antennas can cut down the sensitivity of signal polarization, adapt to different transmission environments and demands, reduce the power loss caused by polarization mismatch, and thus improve the efficiency of power transmission. However, it is challenging to make the antenna with both circular polarization and high gain performance. References [7–8] utilized a two-layer antenna structure to realize the CP design of antennas, but their gains are lower than 10 dB. On the basis of the CP antennas units, references [9–13] form an array to enhance the antenna gain. Although the CP and the high gain performances are implemented, a relatively complex feeding network is required.

This article proposes a gain-enhanced CP microstrip patch antenna with low profile, which can be used in microwave wireless transmission systems. By utilizing the slotting technique of the symmetric structure, the current distribution of the patch antenna can be changed to achieve gain enhancement. At the same time, by adding a pair of narrowband microstrip lines in the -45° direction of the antenna, the two rectangular patches aligned along the x-axis and y-axis can be successfully excited to produce signals of equal amplitude with a phase difference of 90°, thereby achieving the characteristic of circular polarization. In addition, this antenna adopts a single dielectric layer. Compared with double-fed and microstrip-fed antennas, the single-feed antenna avoids the complex feed network of the antenna array, and it has the advantages of simple fabrication and low cost.

II. THEORY OF CIRCULAR POLARIZATION

A. Antenna directionality principle

Antennas usually radiate in a particular direction. The directivity $D(\theta,\phi)$ of an antenna is defined as the ratio of the radiated power per unit steradian angle to the power received by an isotropic radiator. The directivity of an antenna can be obtained by:

$$D(\theta,\phi) = \frac{\frac{1}{2}\times r^2\times \mathrm{Re}[\mathrm{E}\times H^*]}{\frac{P_{rad}}{4\pi}} = \frac{2\pi\times r^2\times \mathrm{Re}[\mathrm{E}\times H^*]}{P_{rad}}. \tag{1}$$

E, H, r and P_{rad} are the peak power of the electric field, the peak power of the magnetic field, the distance between the source and the test point, and the power radiated by the antenna, respectively.

The gain of an antenna is an indicator of its ability to converge power to a specific direction, which is closely related to the directionality of the antenna. The gain is not only closely related to the directionality of the antenna, but also to the radiation efficiency of the antenna. The radiation efficiency considers the potential energy loss that the antenna may experience during the radiation process. The gain of an antenna can be expressed as:

$$G(\theta,\phi) = \eta\cdot D(\theta,\phi). \tag{2}$$

$D(\theta,\varphi)$ is the antenna directivity mentioned in equation (1), and η is the radiation efficiency of the antenna, which is usually determined by the antenna design and material properties.

B. Circular polarization principle

Circular polarization of an antenna can be realized by radiating two orthogonal electric field components in the far-field region. The electric field radiated by the antenna can be expressed as:

$$\vec{E}(\theta,\phi) = \vec{E}_\theta(\theta,\phi)\,\mathrm{e}^{j\phi_1} + \vec{E}_\phi(\theta,\phi)\,\mathrm{e}^{j\phi_2}. \tag{3}$$

Here, $\overrightarrow{E}_\theta(\theta,\phi)\,e^{j\phi_1}$ and $\overrightarrow{E}_\phi(\theta,\phi)\,\mathrm{e}^{j\phi_2}$ denote the magnitude of the electric field components in the far field of the antenna, respectively. ϕ_1 and ϕ_2 denote the phase shift of each field component, respectively.

Circular polarization can be achieved when the total vector of the electric field is composed of two orthogonal components with equal amplitude and a 90° phase difference between them, as expressed in the following equation:

$$E_\theta(\theta,\phi) = E_\phi(\theta,\phi). \tag{4}$$

$$\phi_1 - \phi_2 = \pm\frac{\pi}{2}. \tag{5}$$

For CP waves, the electric field vector at any point in space traced as a function of time is a circle. This continuous circular motion is a unique electromagnetic property of CP waves. It ensures that the electromagnetic waves have the same radiation characteristics in all directions, thus providing a high degree of flexibility and robustness in wireless communications. The mode of polarization, on the other hand, can be determined by observing the temporal rotation of the field of the wave along the direction of propagation. If the rotation of the field is clockwise, the radiated wave is right-hand circular polarization (RHCP). If the rotation of the field is counterclockwise, the radiated wave is left-hand circular polarization (LHCP).

III. GAIN-ENHANCED CP ANTENNA DESIGN

A. Antenna structure

Figure 1 shows the structure of the designed gain-enhanced CP antenna. The antenna is implemented on F4BM substrate, with the relative dielectric constant ε_r of 2.2, the loss tangent angle tanδ of 0.001, and the thickness of the substrate is 1.5 mm. The selection of substrate materials with low dielectric constant and low loss tangent is crucial for optimizing the radiation characteristics of the antenna and reducing energy loss. Consequently, after optimizing the thickness parameter of the substrate, we have chosen F4BM with a thickness (H) of 1.5 mm as the substrate material. The antenna pattern is printed on the top layer of the dielectric plate, and the grounding plane is printed on the bottom layer, and coaxial back-feeding is used, and the feed point is set at a position F=6 mm away from the center of the patch. The structure of the antenna consists of two orthogonal rectangular microstrip patches and a pair of rectangular slots placed along the x-axis and y-axis, respectively. A pair of rectangular narrow microstrip lines is added to the diagonal of the patch antenna. The detailed structure of the proposed antenna is shown in Fig. 1. The proposed antenna is simulated by a high frequency structure simulator (HFSS). Table 1 shows the final structural parameter values of the proposed antenna.

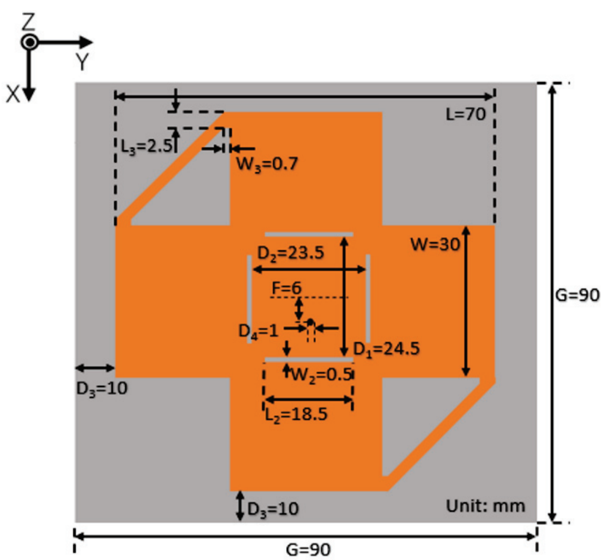

(a)

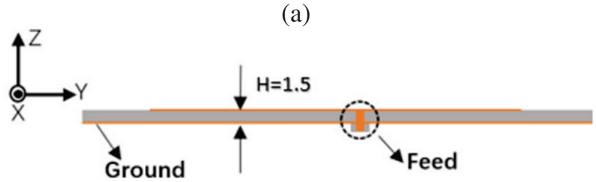

(b)

Fig. 1. Proposed high gain CP patch antenna structure: (a) top view and (b) side view.

Table 1: Parameters of the proposed antenna (unit: mm)

G	L	W	F	L_2	W_2	H
90	70	30	6	18.5	0.5	1.5
L_3	W_3	D_1	D_2	D_3	D_4	
2.5	0.7	24.5	23.5	10	1	

B. Evolution of antenna design

In the first step, as shown in Fig. 2 (a), antenna I is a long rectangular microstrip patch, which is a simple coaxial back-feeding method. Compared with the conventional half-wavelength patch antenna, the design of the long rectangular patch antenna permits the distribution of multiple half-wavelength-length radiation units on the patch.

Due to the multi-period electromagnetic distribution on the patch antenna, there must be an anti-phase current. The anti-phase current will affect the radiation efficiency of the antenna, causing destructive interference with the in-phase current in the far-field region, affecting the radiation mode of the antenna, thereby cutting down the gain of the antenna. Next, on the basis of antenna I, a pair of narrow rectangular slots is loaded about half a wavelength away from the center of the patch, that is, the two

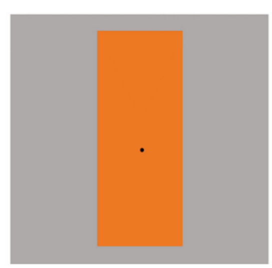

(a)

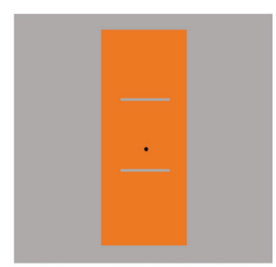

(b)

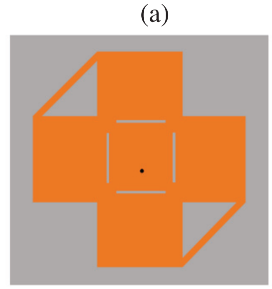

(c)

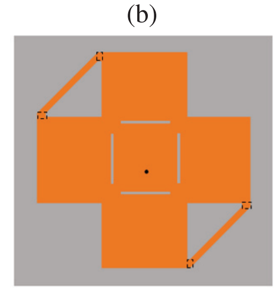

(d)

Fig. 2. Evolution of the antenna structure (a) antenna I, (b) antenna II, (c) antenna III and (d) antenna IV.

slots are approximately one wavelength apart, as shown by antenna II in Fig. 2 (b).

Figure 3 illustrates the distribution of vector currents on the resonant patch. From the arrows marked in Fig. 3 (a), it can be seen that antenna I distributes reverse currents. For the location of the reverse currents, a narrow rectangular slot is added between the co-current and the reverse current so that the reverse currents are forced to be distributed around the rectangular slot, as shown in Fig. 3 (b). At both sides of the rectangular slot, the current flow direction is reversed, so the current on both sides of the slot interacts with each other in the far field region of the antenna, which greatly reduces the influence of the reverse current. According to equation (1), the electric field E and magnetic field H in the far field region of the antenna are improved after adding the rectangular slot, so the directivity and gain of the antenna are effectively improved. Figure 4 shows the reflection coefficient curves of the antennas of several structures shown in Fig. 2. The reflection coefficient curves of the structure of Fig. 2 (a) are shown in the curve Ant.I in Fig. 4, and the resonance point deviates from 5.8 GHz. The reflection coefficient curves of the structure of Fig. 2 (b) are shown in the curve Ant.II in Fig. 4, and the resonant frequency is adjusted to about 5.8 GHz by choosing the appropriate length and width dimensions of the rectangular slot, L_2 =18.5 mm and W_2 = 0.5 mm. The reflection coefficient curve of the antenna structure in Fig. 2 (c) is curve Ant.III in Fig. 4. A slight degradation appears in the performance of curve Ant.III that is primarily due to the implementation of circular polarization, which leads to a decrease in the reflection performance. Four small rectangular microstrips are added in Fig. 2 (d), as shown in the position of the dotted box. Resonance frequency 5.8 GHz belongs to the Industrial, Scientific, and Medical (ISM) frequency band, which does not cause interference to other communication systems and is one of the best frequency points for wireless power transmission. Moreover, the electrical length corresponding to 5.8 GHz is smaller than that of free frequency bands such as 2.45 GHz, which can reduce the size of the antenna. From Fig. 5, it can be observed that at the frequency of 5.8 GHz, the gain of antenna II has increased to 11.4 dB compared with antenna I. The curve Ant.IV indicates the

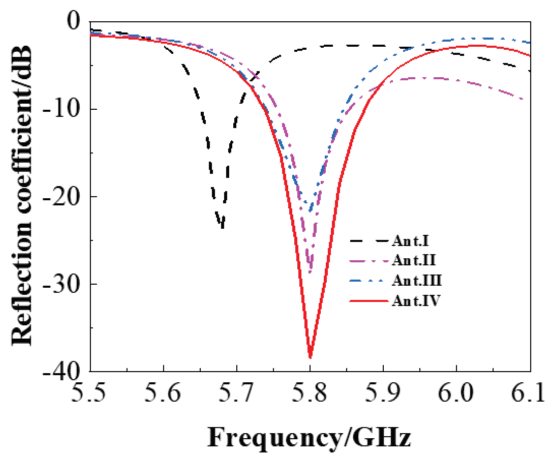

Fig. 4. Simulated reflection coefficient of antennas.

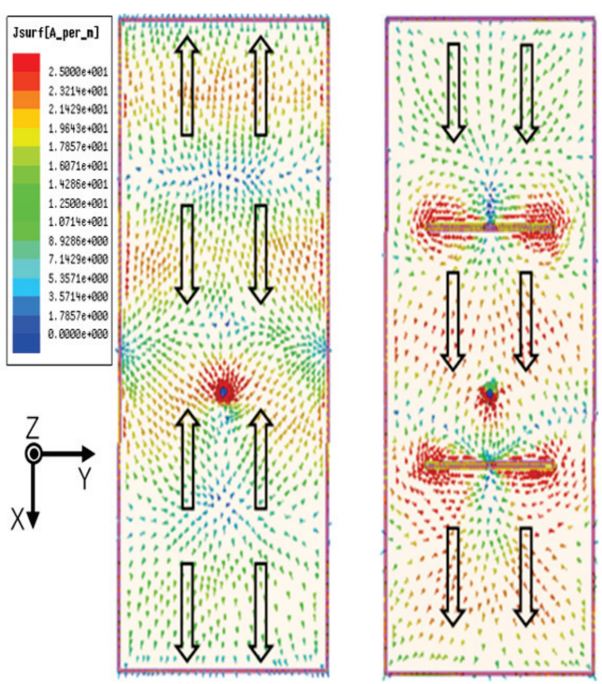

(a) (b)

Fig. 3. Vector current distribution with phase information of long rectangular microstrip patch: (a) antenna I and (b) antenna II.

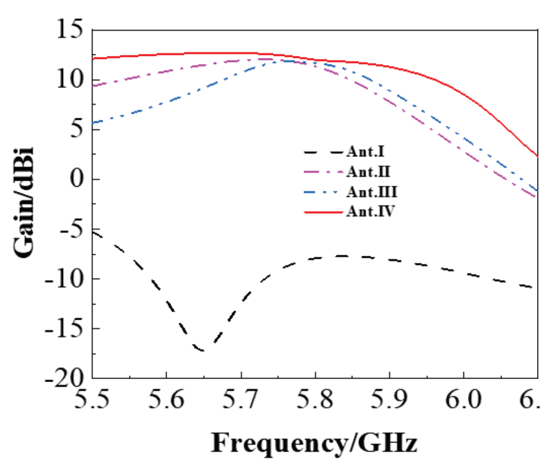

Fig. 5. Simulated gain of antennas.

gain simulation curve of the final structure of the proposed antenna with a gain of 11.9 dB at working frequency of 5.8 GHz.

C. Implementation of CP characteristics

An antenna must be capable of simultaneously radiating two signals that are of equal amplitude, orthogonal to each other, for achieving CP characteristic in the far field. The resonant current direction of antenna II is towards the x-axis in the Fig. 3 (b). To ensure that there is resonant current along the y-axis direction as well, the antenna II is rotated by 90° around the center point of the patch, forming a cross-shaped patch antenna. In order to achieve circular polarization, a pair of narrow microstrips are loaded at the edge of the cross patch along the direction of the antenna -45° diagonal, as shown in antenna III in Fig. 2 (c). To reduce the axial ratio (AR) value of the proposed antenna at 5.8 GHz, two rectangular microstrips with small dimensions are added at both terminals of the narrow microstrip line, as shown in Fig. 2 (d). The purpose of this design is to increase the current flow path and change the current phase difference between the two rectangular patches along the x-axis and the y-axis direction to optimize the AR value. It is also worth noting that, compared to antenna III, the resonant frequency point of the antenna will be shifted by 5.8 GHz due to the structural change of antenna IV. Therefore, antenna IV also needs to adjust the distance of the two pairs of resonant slots distributed along the x-axis and y-axis from the center of the patches, respectively. Finally, the structure parameter of D_1 is chosen to be 24.5 mm while D_2 is 23.5 mm, as shown in Fig. 1.

The changes in the AR curve during evolution process of the antenna structure in Fig. 2 are shown in Fig. 6 (a). The AR curves Ant.I and Ant.II are greater than 50 dB when theta is equal to zero. After adopting the structure of Fig. 2 (c), the AR of the antenna is greatly reduced without affecting the gain of the antenna. However, the AR value of the antenna is still higher than 3 dB, and further design is still needed to improve the circular polarization AR. From Fig. 6 (b), it is obvious that, compared to AR curve Ant.III, the AR of curve Ant.IV is reduced to less than 3 dB while its resonance frequency and gain remain the same.

Figure 7 demonstrates the distribution of the current on the surface of the patch antenna for phi=0°, 90°, 180°, and 270°, respectively. The arrows mark the main direction of the current on the patch. Observing along the reverse direction of the electromagnetic wave propagation direction, it is obvious from Fig. 7 that the vector currents show a clockwise rotation tendency, and thus the antenna has the characteristic of left-hand circular polarization. Similarly, according to the symmetry property of the antenna, if a pair of narrow microstrip

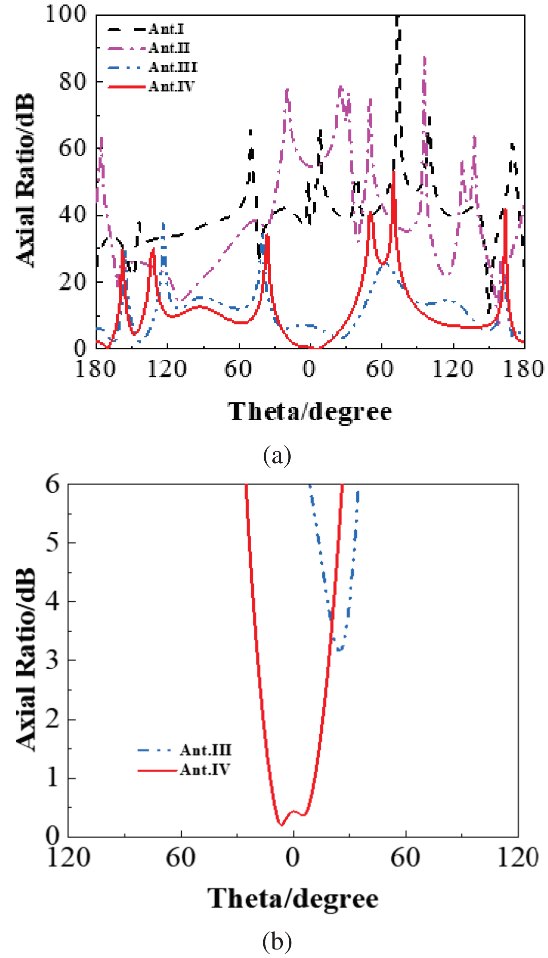

Fig. 6. Simulated axial ratio of (a) antennas I-IV and (b) antennas III and IV.

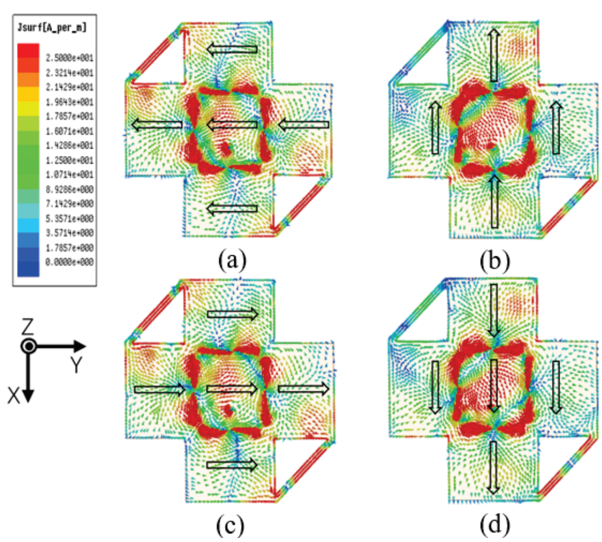

Fig. 7. Current distribution of the proposed antenna for (a) phi=0°, (b) phi=90°, (c) phi=180° and (d) phi=270°.

lines are loaded in the 45° direction of the patch antenna and similarly observed along the reverse direction of the electromagnetic wave propagation direction, the currents will show a tendency to rotate counterclockwise, and the antenna will have the characteristic of right-hand circular polarization.

IV. ANTENNA MEASUREMENTS AND DISCUSSION

To verify the performance of the designed antenna, the antenna was fabricated on the F4BM substrate. The antenna is measured in a microwave anechoic chamber with the setup shown in Fig. 8. The structure parameter values of the fabricated antenna samples are consistent with the data listed in Table 1. Figures 9 to 12 show the simulated and measured reflection coefficient curves, realized gain, and AR curves of the antenna. In Fig. 9, the measured reflection coefficient has obvious frequency shifts and the reflection deterioration. After discussion and analysis, the main reason may be due to machining accuracy or material tolerances during the production and welding process of the antenna, as well as errors brought about by the adapter, which can lead to the actual matching performance decreases and resonance changes, thus causing frequency shifts and reflections to increase. The simulated and measured 10 dB impedance bandwidth (S11≤-10 dB) is 2.2% (5.74-5.87 GHz) and 2.8% (5.77-5.93 GHz), respectively. Figure 10 shows the simulated and measured gain curves. The measured maximum gain reaches 11.3 dB at the operating frequency of 5.8 GHz. The measured maximum gain is slightly lower than the simulated gain, which may be due to the tolerance of the antenna fabrication and the loss of electromagnetic energy during the testing process. Additionally, as depicted in Fig. 10, there is a notable difference between the simulated and measured gain within the 5.5-5.7 GHz frequency band. This variation may stem from the antenna's structural properties changing at the frequency of near 5.5 GHz, which impacts the measured outcomes, as well as potential measurement errors that could occur during the testing process. The antenna designed in this article focuses on

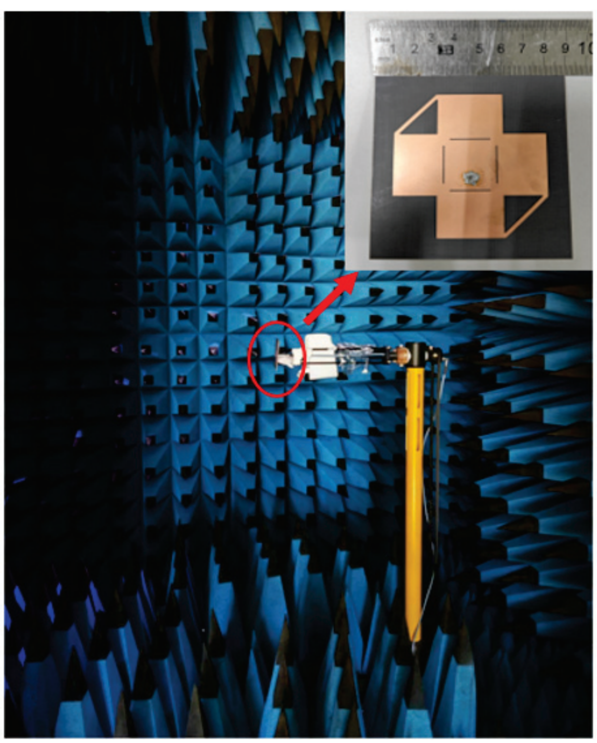

Fig. 8. Prototype of the proposed antenna and its measurement setup.

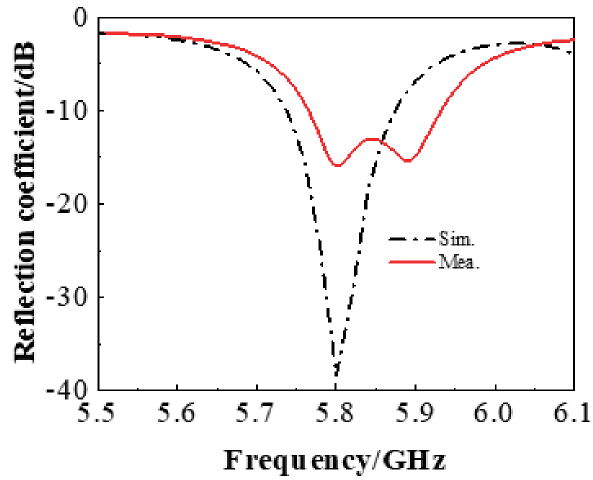

Fig. 9. Simulated and measured reflection coefficient for proposed antenna.

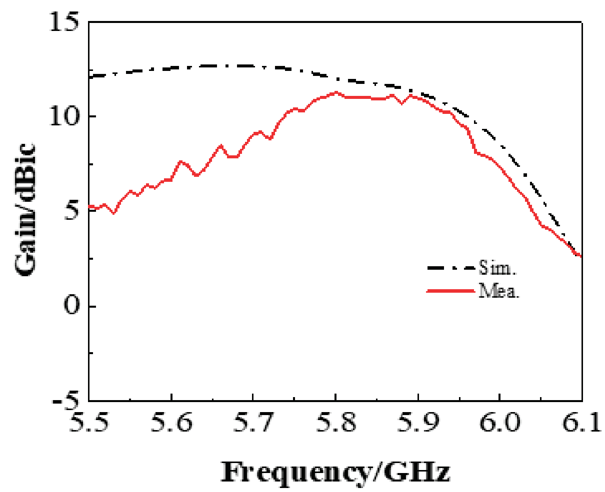

Fig. 10. Simulated and measured gain for proposed antenna.

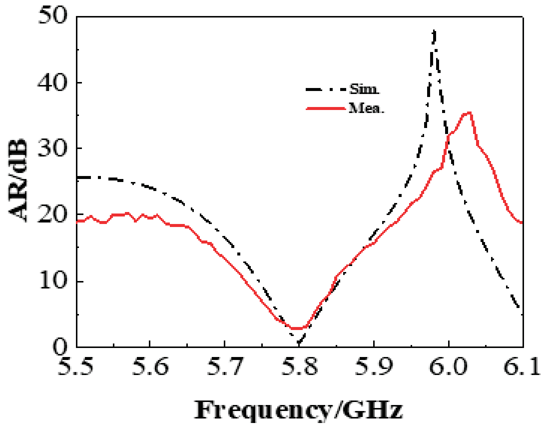

Fig. 11. Simulated and measured AR for proposed antenna with changing frequency.

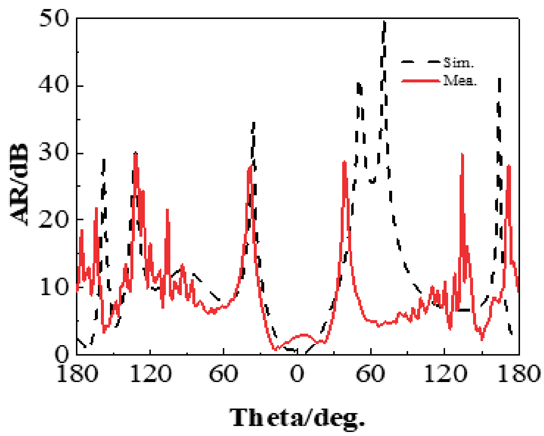

Fig. 12. Simulated and measured AR for proposed antenna with changing theta.

wireless power transmission at the working frequency of 5.8 GHz, so the matching of the antenna mainly concentrates on the around 5.8 GHz frequency point. The difference between simulation and actual measurement from 5.5 GHz to 5.7 GHz is mostly caused by impedance mismatch and other factors. However, since the antenna designed in this article is specifically targeted for the 5.8 GHz frequency, the impact of such differences can be disregarded. Figures 11 and 12 show the AR curves of the antenna for frequency variation and theta variation, respectively. The simulated and measured 3 dB AR bandwidths are both 0.52% (5.78-5.81 GHz). The proposed antenna maintains good circular polarization characteristics at 5.8 GHz.

Figure 13 shows the simulated and measured radiation of the proposed CP antenna in the xoz and yoz planes. At the center frequency of 5.8 GHz, Fig. 13 (a) is the co-polarization (LHCP) pattern and cross-

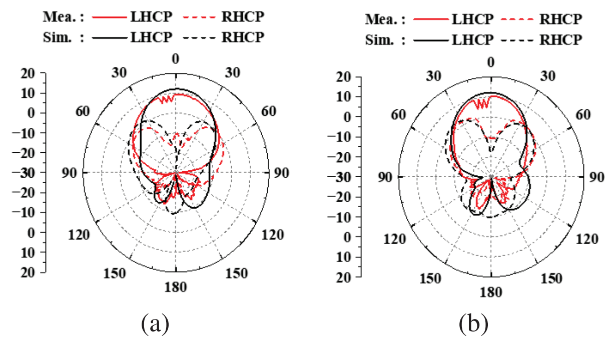

Fig. 13. Radiation pattern of antenna at 5.8 GHz: (a) xoz plane and (b) yoz plane.

polarization (RHCP) pattern in the xoz plane. Figure 13 (b) is the co-polarization (LHCP) pattern and the cross-polarization (RHCP) pattern in the yoz plane. It can be seen that the measured LHCP gain is more than 20 dB higher than the corresponding RHCP gain in Fig. 13. Therefore, the designed CP antenna has clear LHCP characteristics. Although there are minor differences between the measurements and simulations, their overall agreement is acceptable. The minor differences may be mainly attributed to manufacturing tolerances and experimental measurement errors.

Table 2 provides a detailed comparison of the high-gain CP antenna proposed in this paper with the antenna performance reported in the existing literature. Since both the impedance bandwidth and the 3 dB AR bandwidth include the key frequency of 5.8 GHz, the antenna designed in this study is highly suitable for MPT. Compared to other antennas for MPT detailed in Table 2, the antenna designed here is more compact in size. Further-

Table 2: Comparison of recently reported antennas for microwave wireless power transmission

Ref.	Overall Size (λ_0^3)	Polarization	εr	Gain (dBi)	Impedance BW (GHz)/ FBW	3 dB AR BW(GHz) /FBW
[14]	4.45 ×4.45 ×4	LP	-	13.4	5.3-6.3 (17.24%)	-
[15]	1.93 ×1.93 ×0.075	CP	2.2	8.5	5.53-6.06 (9.14%)	5.74-5.89 (2.58%)
[16]	2.08 ×49.17 ×0.06	CP	10	5.87	5.77-5.85 (1.38%)	5.74-5.84 (1.72%)
[17]	2.18 ×2.18 ×0.04	CP	3.55	3.8	5.75-5.92 (2.93%)	5.77-5.84 (1.21%)
This work	1.74 ×1.74 ×0.029	CP	2.2	11.3	5.77-5.93 (2.8%)	5.78-5.81 (0.52%)

more, although the antennas described in [16–18] are all CP, the antenna proposed in this paper utilizes gain enhancement techniques. This results in a gain that is 2.8-7.5 dB higher than that of other CP antennas, which is beneficial for improving the efficiency of MPT.

V. CONCLUSION

In this study, a novel gain-enhanced CP microstrip patch antenna is proposed. The gain of the antenna is enhanced by loading two narrow rectangular slots to the conventional rectangular microstrip patch. The microstrip patch is rotated by 90° to form a cross microstrip patch antenna. Meanwhile, some microstrip structures are added at the edges to change the flow direction of the current to implement the CP characteristic. The position of the two pairs of narrow rectangular slots is slightly adjusted to fine-tune the resonant frequency without affecting other characteristics.

The experimental measurements show that the antenna gain reaches 11.3 dB and AR reaches 2.73 dB at the resonant frequency of 5.8 GHz, which satisfies the performance requirements of high gain and CP for use in microwave power transmission antennas. The design method and experimental results of this study provide valuable references for the antenna design of future microwave transmission systems. It not only provides new tools and solutions for the development of microwave transmission technology but also brings new research ideas and development directions in the field of antenna design.

ACKNOWLEDGMENT

This work was supported by the Fujian Natural Science Foundation Project (2022J01823) and Xiamen Science and Technology Subsidy Project (2024CXY0314).

REFERENCES

[1] Y. Cao, Y. Cai, W. Cao, B. Xi, Z. Qian, and T. Wu, “Broadband and high-gain microstrip patch antenna loaded with parasitic mushroom-type structure,” *IEEE Antennas and Wireless Propagation Letters*, vol. 18, no. 7, pp. 1405-1409, July 2019.

[2] X. Zhang, L. Zhu, and Q.-S. Wu, “Sidelobe-reduced and gain-enhanced square patch antennas with adjustable beamwidth under TM03 mode operation,” *IEEE Transactions on Antennas and Propagation*, vol. 66, no. 4, pp. 1704-1713, Apr. 2018.

[3] K.-D. Hong, X. Chen, X. Zhang, L. Zhu, and T. Yuan, “A slot-loaded high-gain circular patch antenna with reconfigurable orthogonal polarizations and low cross polarization,” *IEEE Antennas and Wireless Propagation Letters*, vol. 21, no. 3, pp. 511-515, Mar. 2022.

[4] X. Zhang and L. Zhu, “Gain-enhanced patch antennas with loading of shorting pins,” *IEEE Transactions on Antennas and Propagation*, vol. 64, no. 8, pp. 3310-3318, Aug. 2016.

[5] W. Li, Y. Suo, X. Xu, and Y. Liu, “A gain-enhanced rectangular patch antenna with artificial magnetic conductor ground,” in *2017 IEEE International Symposium on Antennas and Propagation & USNC/URSI National Radio Science Meeting*, San Diego, CA, pp. 2177-2178, 2017.

[6] G. Dhaundia and K. J. Vinoy, “A high-gain wide-band microstrip patch antenna with folded ground walls,” *IEEE Antennas and Wireless Propagation Letters*, vol. 22, no. 2, pp. 377-381, Feb. 2023.

[7] G. Cheng, B. Huang, Z. Huang, and L. Yang, “A high-gain circularly polarized filtering stacked patch antenna,” *IEEE Antennas and Wireless Propagation Letters*, vol. 22, no. 5, pp. 995-999, May 2023.

[8] X. Chen, L. Yang, J.-Y. Zhao, and G. Fu, “High-efficiency compact circularly polarized microstrip antenna with wide beamwidth for airborne communication,” *IEEE Antennas and Wireless Propagation Letters*, vol. 15, pp. 1518-1521, 2016.

[9] C. S. Ong, M. F. Karim, L. C. Ong, T. M. Chiam, and A. Alphones, “A compact 2×2 circularly polarized antenna array for energy harvesting,” in *2010 Asia-Pacific Microwave Conference*, Yokohama, Japan, pp. 1977-1980, 2010.

[10] A. Verma, M. Arrawatia, and G. Kumar, “Broadband series-fed circularly polarized microstrip antenna array,” in *2020 IEEE International Symposium on Antennas and Propagation and North American Radio Science Meeting*, Montreal, QC, Canada, pp. 225-226, 2020.

[11] M. A. Sennouni, J. Zbitou, B. Abboud, A. Tribak, and M. Latrach, “Efficient rectenna design incorporating new circularly polarized antenna array for wireless power transmission at 2.45GHz,” in *2014 International Renewable and Sustainable Energy Conference (IRSEC)*, Ouarzazate, Morocco, pp. 577-581, 2014.

[12] K. Ding, C. Gao, T. Yu, D. Qu, and B. Zhang, “Gain-improved broadband circularly polarized antenna array with parasitic patches,” *IEEE Antennas and Wireless Propagation Letters*, vol. 16, pp. 1468-1471, 2017.

[13] V. Rafii, J. Nourinia, C. Ghobadi, J. Pourahmadazar, and B. S. Virdee, “Broadband circularly polarized slot antenna array using sequentially rotated technique for C-band applications,” *IEEE*

Antennas and Wireless Propagation Letters, vol. 12, pp. 128-131, 2013.

[14] C. Chen, B. Zhang, and K. Huang, "Nonuniform Fabry-Perot leaky-wave antenna with flat-topped radiation patterns for microwave wireless power transmission," *IEEE Antennas and Wireless Propagation Letters*, vol. 18, no. 9, pp. 1863-1867, Sep. 2019.

[15] D. M. Nguyen, N. D. Au, and C. Seo, "Aperture-coupled patch antenna with flat-top beam for microwave power transmission," *IEEE Antennas and Wireless Propagation Letters*, vol. 21, no. 10, pp. 2130-2134, Oct. 2022.

[16] D. Surender, Md. A. Halimi, T. Khan, F. A. Talukdar, B. K. Kanaujia, and K. Rambabu, "Analysis of facet-loaded rectangular DR-rectenna designs for multisource RF energy-harvesting applications," *IEEE Transactions on Antennas and Propagation*, vol. 71, no. 2, pp. 1273-1284, Feb. 2023.

[17] M. Chang, J. Han, Y. Li, X. Ma, H. Liu, and L. Li, "Self-powered polarization-reconfigurable rectenna for wireless power transfer system," *IEEE Transactions on Antennas and Propagation*, vol. 71, no. 8, pp. 6297-6307, Aug. 2023.

Ziyang Jiang was born in 2002 in Fujian Province, China. He is currently pursuing his B.S. degree with the Department of Communication Engineering at Jimei University, Fujian Province, China. His research interests are circularly polarized antenna technology and rectenna technology.

Zhonghua Ma was born in Gansu, China, in 1973. He received his Ph.D. in Microelectronics from Lanzhou University in 2018. His present research interests include the antenna techniques, RF circuits design, WPT and IoT.

Xiaojing Sun was born in 2004 in Hebei Province, China. She is currently pursuing her B.S. degree with the Department of Communication Engineering at Jimei University, Fujian Province, China. Her research interests are in microwave technology and rectenna technology.

Weiqian Liang was born in Heilongjiang Province, China, in 1977. He received his Ph.D. in Electronic Science and Technology from Tsinghua University in 2006. His current research interests include signal processing, deep learning and embedded systems.

Haitao Xing was born in 1983 in Shandong, China. In 2010, he obtained a master's degree in communication and information engineering from Ningbo University. At present, his main research interests are embedded system, artificial intelligence and Internet of Things.

Accelerated Variant Model-aided Optimization of Coupled Line Bandpass Filter

Ahmet Uluslu

Department of Electronics and Automation
Istanbul University-Cerrahpaşa, Istanbul 34500, Turkey
auluslu@iuc.edu.tr

Abstract **–** Here, a 5-row microstrip coupled line filter design with six different variable design parameters having a center resonance frequency of 2.45 GHz is considered as a multi-dimensional and single-objective optimization problem using a variant of the newly proposed Chameleon swarm algorithm. In this study, three different objective functions specially adapted from mathematical models were used for the current problem. Additionally, artificial neural network (ANN) modeling support was used for acceleration, thus eliminating the extra hardware cost that may be needed. The filter toolbox, which was recently released with the MATLAB 2021b version, was used throughout the optimization process. The study includes multiple innovations, including the updated algorithm, new toolbox and original objective functions.

Index Terms **–** Chameleon swarm algorithm, coupled line bandpass filter, evolutionary algorithms, non-uniform microstrip filter, optimization techniques, swarm intelligence algorithms.

I. INTRODUCTION

Microwave filters are very important in RF and microwave applications. They combine or separate different frequencies from each other. Filters are frequently encountered in microwave systems, especially in satellite and mobile communication systems. The most sought-after features in these filter designs are high performance, low loss, small size and low cost. At the beginning of the usage areas of bandpass filters, we can offer devices such as oscillators and mixers to prevent unwanted signals. Many microwave systems, such as these devices, incorporate bandpass filter structures to block unwanted signals. In order to meet the requirements arising in this context, filters are designed as collective element and discrete element circuits. These designs consist of waveguide, coaxial line and microstrip transmission lines [1]. Microstrip parallel-connected filters consisting of microstrip transmission line are widely used in these designs because they have many advantages [2]. These parallel-connected microstrip filters used can create an unsymmetrical passband response as well as excess passband at multiples of the targeted frequency. The reason for the common harmonic's formation in parallel connected microstrip filters is the difference in the phase velocities in the inhomogeneous dielectric medium in the microstrip structure. This causes performance degradation in systems such as frequency divider or WLAN receiver.

Combined microstrip lines are used in many circuit functions and the design procedures are well established [3, 4]. Principle application areas are directional combiners, filters and delay lines [5]. Parallel coupled line filters are generally used in microwave technologies at high frequencies (up to 0.8-30 GHz). At low- and mid-level frequencies, bandpass or filtering filters are generally in the form of distributed circuits and are used by combining classical resistors, coils and capacitors in different ways according to needs [6]. Resistors, coils and capacitors become an unstable and unsolvable material that encounters many problems as higher frequencies are increased. For this reason, at high frequencies, parallel combined line filters can be used as a solution with a completely different way of thinking and production without the need for conventional circuit elements. In microstrip structures, materials with different properties are combined on top of each other in different thickness, height and length, and these long strips are produced on the card surface in a straight, horizontal, perpendicular and parallel manner. The thickness of these strips, the distance between the strips, how long they will be and whether the strips will be connected to each other are decided during the design [7]. When the structure of the material used in the strips and the state of the layers are evaluated together with other components, it will answer questions such as what the center frequency, bandwidth and harmonics of the designed filter will be. As a result, since trouble-free filters cannot be designed with resistance coils and capacitors at high frequencies, fabricated to do their job, parallel combined line filters, which are stable at high frequencies

Submitted On: October 16, 2024
Accepted On: December 15, 2024
https://doi.org/10.13052/2024.ACES.J.391207
1054-4887 © ACES

and comply with the principles of materials science, are designed [8]. When two unshielded transmission lines are placed side by side, a proportion of the power available to the main line is coupled to the secondary line. Bandpass filters are indispensable elements of communication system designs. They reduce harmonics and spurious emissions for transmitters [9]. In coupled lines, the characteristic impedance can be increased [10] to widen the gaps and reduce coupling. Narrowing the line widths can cause an increase in conductor loss. Electromagnetic field analysis or experimental measurements may be needed to find the distance to be left between the resonators [11]. However, the design equations of the stepped track structure are only correct for the central frequency of the passband and further optimization with CAD tools is still required [12]. In brief, although there are methods that contain many empirical equations for filter designs, their complexity and inconsistency in some cases have led designers to filter simulation programs [13, 14].

Although there is a great interest in the design and optimization of microstrip combined line filters in the literature, there are many studies on it [15, 16]. In one study, circuit implementation of the filter was made through concentrated components such as inductors (L) and capacitors (C) for even and odd filter order. Afterwards, it was designed in a microstrip structure using mathematical equations and simulated with the help of the CST program. Both the inconsistency of the mathematical equations and the complexity of the method have made the design very difficult [17]. In another study, microstrip coupled line bandpass filter design with 400 MHz bandwidth has been made. Since this study is based on mathematical equations, it has computational complexity as well as computational redundancy [18]. In another study, a method for optimizing the coupling gaps for a microstrip bandpass filter design using cross-linked resonators to achieve high selectivity is presented [19]. PSO was used as the algorithm. The optimization process is based on mathematical equations. In addition, many filter design optimization studies have been done [20–23]. However, many of them perform the validation simulation for a single model by optimizing from numerical calculations.

In recent years, scientists have developed many optimization methods based on different methods in order to overcome multi-dimensional and various optimization problems, in engineering science as well as other fields. In this context, there are several optimization studies on transistors that form the basis of microwave electronics [24–27]. Optimization problems contain single- or multi-objective problems that need to be improved. The mathematical expression of these problems is called the objective function. In addition, these objective functions are combined within themselves and include the cost function. In most problems, the objective functions and design variables are linear. Nonlinear objective functions, on the other hand, have limitations due to their complex structure [28]. Often, nonlinear problems contain sharp and multiple peaks along with many local optima [28]. It may be necessary to generate complex objective functions for optimization problems with complex and large design parameters. The main purpose of optimization is to achieve the global optimum. Meta-heuristic algorithms are very successful in both preventing the local optimum and finding the global optimum. For this reason, studies are carried out on new meta-heuristic algorithm models. One of them is the Chameleon swarm algorithm (CSA), which has been discussed recently. Chameleons are mostly creatures that live in forests or deserts and are constantly searching for food. There was no optimization algorithm in the literature that mimicked the behavior of chameleons in nature, until [29]. In this study, a meta-heuristic algorithm called CSA is presented to solve global optimization problems [29]. The inspiration for this algorithm is the dynamic behavior of chameleons looking for food in nature. In another study on this successful study, developed with existing CSA variant models, supported by original complex linear and nonlinear objective functions, variant models played an active role in finding more performance results [28].

In order to overcome the traditional filter design problems mentioned previously, the complexities and inconsistencies in filter designs suggest that the optimization problem of bandpass filter design can be overcome by using the newly proposed variant CSA. The fact that both the bandwidth and the center resonance frequency can be easily adjusted by changing only the objective function with optimization is a step towards solving traditional problems. In addition, the fact that there is no empirical equation, and the system is simulation-based is an advantage over other studies in terms of closeness to reality. In addition, the large number of filter design parameters and the fact that the filter is bandpass make the problem difficult. In order to overcome this power optimization design problem, the variant CSA supplemented with the original objective functions will be used. There are many bandpass filter studies in the literature, and almost none of them solved by the optimization method are simulation-based. The filter toolbox of MATLAB 2021, which has just been put into use with the 2021b version, saves us from computational confusion. In addition, no filter optimization studies have yet been encountered with the algorithm or its derivatives used.

This article is organized as follows. Filter design is mentioned in section II. In section III, information about the objective and cost functions used together with the variant optimization used is given. The study part is in section IV, and self-criticism is in section V. The paper concludes with section VI.

II. FILTER DESIGN

Microstrip transmission lines are the most widely used transmission lines in microwave engineering and applications. Discussing the advantages and disadvantages of microstrip transmission lines, the fact that the circuit is on a patch allows it to easily adapt to the surface on which it is applied. We can add ease of production and low cost as another advantage. If we talk about the disadvantages, its high insulation can cause radiation and undesired filter response. Also, although the microstrip supports transverse electromagnetic mode (TEM) due to the fill factor, in some cases it may appear non-TEM due to the interconnection of the lines. Therefore, we can classify the frequency of the microstrip bandpass filter as asymmetric [30]. The dielectric constant of the substrate is greater than the effective dielectric constant because some parts of the transmission line are in air. Therefore, dielectric constants are important for microstrip lines. There are many studies on microstrip coupled line filter design [31, 32]. In particular, microstrip line Chebyshev single band and dual bandpass filters are widely available [33–35]. There are also many bandpass filter designs made with different approaches [33–35].

Here, a bandpass filter with a middle band of 2.45 GHz with a microstrip combined line filter structure will be designed. The proposed filter consists of the supply connected to the parallel lines connected between the two ports. In the proposed design, the characteristic impedance is chosen as $Z_0 = 50\ \Omega$, while the microstrip bandpass is designed on Teflon material with ε_r=4.4 and the combined line filter height $h = 1.6$ mm from the ground plane. Figure 1 shows the schematic of the filter design. The design parameter values specified in the diagram are given in Table 1 in detail. Of the eight design parameters specified here, six of them are variable and two of them are fixed values. In addition, three of the variable design parameters contain six different variable parameters. In the design processes, PEC was chosen as the conductor and Teflon as the substrate. Although there are many empirical equations and methods for microstrip coupled line filter design, it has been mentioned that the equations are not suitable for practical designs due to their inconsistency and the technique is old [13–14]. For this reason, the filter toolbox of MATLAB 2021, which is one of the toolboxes that are libraries of MATLAB functions adapted to MATLAB for the solution of special problems in optimization operations and filter simulations in the study, was used. A toolbox in Simulink is a collection of blocks and functions used to simulate complex engineering systems. In short, toolboxes provide ready-made blocks and functions that allow users to design, simulate and debug their systems quickly and easily. In addition, although this toolbox is still very new, it has been made available with the 2021b version. Thus, the complexity and inconsistency in the equations have been completely overcome. At the same time, this situation can be considered as a digital model representing

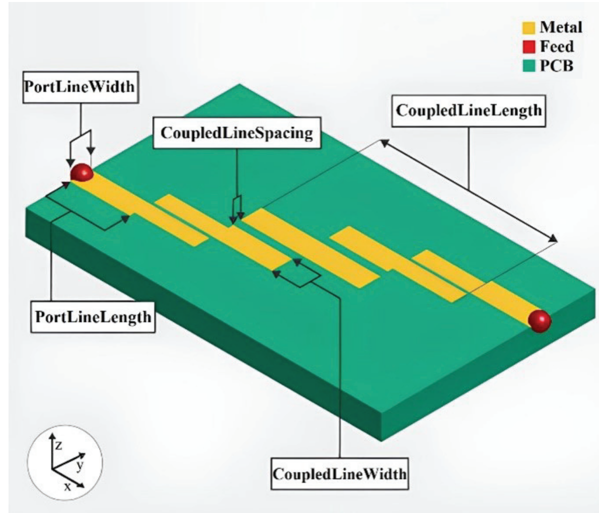

Fig. 1. Coupled line filter.

Table 1: Coupled line filter design parameters

Parameter	Definition	Center Value	Value Range
FilterOrder	Filter order	5	-
PortLineLength	Length of input and output lines	27.9 (mm)	±40%
PortLineWidth	Width of input and output lines	5.1 (mm)	±40%
CoupledLineLength	Lengths of coupled lines	[27.9 27.9 27.9 27.9 27.9 27.9]	±40%
CoupledLineWidth	Widths of coupled lines	[3.6 4.9 4.9 4.9 4.9 3.6]	±40%
CoupledLineSpacing	Distance between coupled lines	[0.1827 1.9 1.9 1.9 1.9 0.1827]	±40%
Height	Height of coupled line filter from ground plane	1.6 (mm)	constant
GroundPlaneWidth	Width of ground plane	55.1 (mm)	±40%
Substrate	Type of dielectric material	Teflon	-
Conductor	Type of metal used in conducting layers	PEC	-

a virtual simulation of real-world objects, processes or systems. Thus, it provides analysis and prediction in real time by simulating the properties, performance and behavior of the physical object, saving it from many empirical equations and load confusion in filter design. In terms of application, it can be easily integrated into optimization stages as a fast, efficient, accurate and practical solution.

III. CHAMELEON SWARM ALGORITHM

Design problems are getting more difficult day by day and designers' demand for better solutions makes existing optimization algorithms insufficient and directs researchers to develop new algorithms. Meta-heuristic algorithms work by integrating them into real simulations to mimic some properties of commodities existing in nature [36]. One of the algorithms that has been developed in recent years and inspired by nature is CSA. This algorithm supports the concept of 'no-free-lunch' (NFL) [29]. Chameleons usually live-in forests or deserts and constantly search for food. A study published a few years ago found an optimization algorithm that mimics the behavior of chameleons in nature [29]. Essentially, the algorithm adapts the movements chameleons make while searching for food to the mathematical model. One part of this is that chameleons catch their prey by rapidly throwing their tongues. When all these behaviors are applied to create an optimization algorithm, a model that finds suitable solutions is obtained. The mentioned CSA algorithm is an algorithm that has proven its success in global optimization problems. In addition, it is seen that more successful results are obtained in the study compared to other meta-heuristic algorithms such as GA, GWO and PSO [29].

The source of inspiration of CSA consists of briefly following the prey, pursuing the prey with its eyes and attacking the prey [28]. To summarize the functions of the algorithm used:

Initialization and function evaluation: Since CSA is a population-based algorithm, this stage covers the beginning of the process.

Search for prey: Covers the updating of the behavior and movements of the chameleons while searching for food.

Rotation of the chameleon eyes: Chameleons have the ability to determine the location of their prey by using the ability to rotate their eyes independently of each other.

Prey hunting: When chameleons are very close to their prey, they attack and conclude the hunting process. We can say that the chameleon that comes closest to its prey is the best and is assumed to be optimal.

In another study, a U-slot antenna design with four resonance frequencies has been discussed as a multi-dimensional and single-objective optimization problem by using CSA and its variants developed in collaboration with CSA, proposed in [28]. It has been suggested that the CSA and its variants can undoubtedly be adapted to any optimization problem with a large number of variable design parameters [28]. The mCSA algorithm produced will be used in the study.

A. Variants of CSA

Reproduction, crossover and mutation are among the most frequently used operators in many population-based optimization algorithms, especially genetic-based optimization algorithms. It is made possible by these basic processes for the previous generation to transfer their characteristics to new generations. Thus, individuals with good characteristics are more likely to be selected for breeding. Considering all these advantages, mutation and crossover operators that were not found in the original CSA were added to the basic CSA and a variant model was derived [28].

Crossover and mutation are two basic operators used in genetic algorithms to create new individuals from existing individuals. The crossover operator is used to generate two new individuals (children) through information exchange (gene swap) from two individuals (parents) in the current population. The purpose of crossover is to combine good parts of old chromosomes to produce new individuals that are expected to be better. The frequency of crossover is controlled by a parameter called crossover probability. A high crossover rate will cause the search space to be explored very quickly, and individuals that are better than others will deteriorate very quickly after new breeding processes. A low crossover rate will cause very few new and different individuals to enter the new generation resulting from reproduction, and the research space will not be adequately scanned. Therefore, determining a reasonable probability value for the crossover rate is important for the performance of the algorithm. Major crossover operators are single-point crossover, two-point crossover and PMX. According to the two-point crossover, the two points to be crossed over in the chromosomes are determined and these parts are exchanged to obtain two new generation chromosomes. Other genes are inherited from the first parent to the first progeny chromosome, respectively. In the same way, transfer is made from the second parent to the second new generation chromosome. During the transfer, if the transferred gene is already present in the new chromosome, the other gene is passed on. If not, this gene is transferred to the new chromosome. In the study, the two-point crossover operator is preferred.

The mutation operator, on the other hand, simulates the genetic mutation event in nature and plays an important role in the success of GA. This operator generates a new solution by changing the value of some genes of the chromosomes of an existing solution. The mutation operator provides scanning of different regions of the solution space by inserting new information into the existing population. In this way, it helps to overcome the problem of early convergence. In a genetic algorithm without a mutation operator, the optimal solution can only be obtained if the necessary information is found in the initial population. Therefore, the population size of the genetic algorithm without a mutation operator will have to be kept very large. This will reduce the speed of the algorithm. The genes to be mutated are randomly determined according to a very small mutation rate. A high mutation rate will introduce excessive randomness to the search and accelerate divergence. Conversely, a low mutation rate will slow divergence and prevent full exploration of the search space. Therefore, the problem of early convergence will arise. Three types of mutation operators have been studied. These are the 'Swap', 'Insert' and 'Shift' mutation operators. The swap operator swaps two randomly determined genes on a randomly determined chromosome. In the study, the 'Swap' operator was preferred.

First, a cut-off point was created between the results found. The algorithm was forced to find the desired results because the costs were shown high in the results that were outside the desired limit. After the calculation of the targets, artificial neural network (ANN) modeling should be added before the solution archive is created. This can shorten the optimization time by reducing the number of iterations to reach the minimum cost value. In addition, all the results found in each step were brought together to form a feasible solution set and this set was used for selection. Figure 2 shows its mathematical modeling. The beginning of the process is to define the parameters of the algorithm, such as the population size, maximum iterations and weight coefficients, as shown in Fig. 2. At this point, the latest development, ANN model support, was specified externally. Thus, the optimization time was shortened by up to six times. As seen in Fig. 2, if the ANN model is included, the calculation part is skipped, and time is saved. All this ends when the best solution is reached.

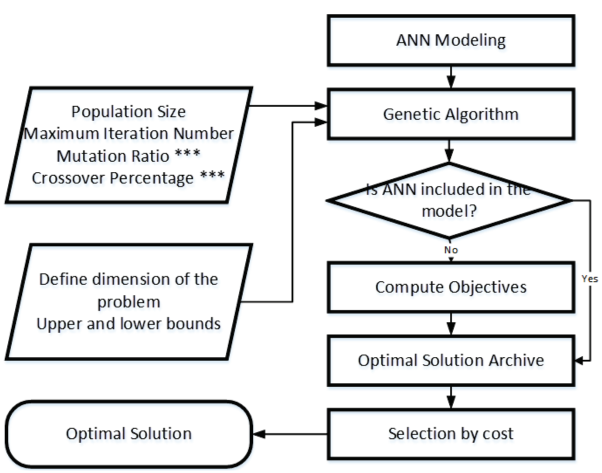

Fig. 2. Flowchart for optimal solution of CSA with accelerated variant model support of the coupled line bandpass filter.

B. Objective and cost functions

The variant model of the CSA, which is a new optimization technique, will be supported with original objective functions in order to obtain more performance results. Here, three different types of objective function pairs are defined for the pass and stop band segments adapted from linear and nonlinear mathematical models. These were named in a study as polynomial, power and exponential model, respectively [28]. Two measurement functions, S_{11} and S_{21}, were chosen as the decision variables that make up these unique objective functions. Here, it is aimed that S_{11} should be as small as possible (maximum -10 dB) in the passband, and S_{21} should be close to 0 in the passing band, and S_{21} should be as small as possible (maximum -10 dB) and S_{11} should be close to 0 in the stopping band. Since S_{11} and S_{21} have the same importance for this problem, the weighting coefficients of the measurement functions ($wc_{1-2} = 0.5$) are taken as equal.

Adapted from the polynomial model, the objective function pairs are defined as follows for two separate parts, the bandpass and the bandstop. Bandpass part:

$$OFp_{11} = \sum_{i=m}^{M} (wc_1 * |S21_i|), \tag{1}$$

$$OFp_{12} = \sum_{i=m}^{M} \left(\frac{wc_2}{|S11_i|} \right). \tag{2}$$

Bandstop part:

$$OFs_{11} = \sum_{j=n}^{N} (wc_1 * |S11_j|), \tag{3}$$

$$OFs_{12} = \sum_{j=n}^{N} \left(\frac{wc_2}{|S21_j|} \right). \tag{4}$$

The objective function pairs adapted from the power model are defined as follows for two separate parts, the bandpass and the bandstop. Bandpass part:

$$OFp_{21} = \sum_{i=m}^{M} (wc_1 * |S21_i|)^2, \tag{5}$$

$$OFp_{22} = \sum_{i=m}^{M} \left(\frac{wc_2}{|S11_i|} \right)^2. \tag{6}$$

Bandstop part:

$$OFs_{21} = \sum_{j=n}^{N} (wc_1 * |S11_j|)^2, \tag{7}$$

$$OFs_{22} = \sum_{j=n}^{N} \left(\frac{wc_2}{|S21_j|} \right)^2. \quad (8)$$

Adapted from the exponential model, the objective function pairs are defined for two separate parts, the bandpass and the bandstop. Bandpass part:

$$OFp_{31} = \sum_{i=m}^{M} wc_1 * e^{-S21_i}, \quad (9)$$

$$OFp_{32} = \sum_{i=m}^{M} wc_2 * e^{S11_i}. \quad (10)$$

Bandstop part:

$$OFs_{31} = \sum_{j=n}^{N} wc_1 * e^{-S11_j}, \quad (11)$$

$$OFs_{32} = \sum_{j=n}^{N} wc_2 * e^{S21_j}, \quad (12)$$

where *i*=2.44 and 2.46, *j*=2.36 and 2.54. Each represent a resonance cutoff frequency.

In addition to all these objective functions, a cost function has been determined. It is found as a result of the collection of the objective function pairs determined for the pass and stop band parts and is defined as follows:

$$cost = OFs_{k1} + OFs_{k2} + OFp_{k1} + OFp_{k2} \quad , \quad k = 1,2,3. \quad (13)$$

In the next section, a detailed working case will be presented on the optimization of the combined line filter with the predetermined design parameters for the bandpass model with a center frequency of 2.45 GHz.

IV. RESULTS

In the analysis part of the study, the variant model of the CSA, which was previously proposed in a study and has proven its success against other traditional algorithms, will be used in the optimization problem of the bandpass combined line filter design with a center frequency of 2.45 GHz. As is known, changing the length and width of the lines will cause different results of the S parameters. In the study, firstly, the analysis of the cases with and without ANN added to show the effect of ANN support on the study was made. Then, the most optimal algorithm parameters will be selected for the problem. Finally, experiments will be made with equal weight functions for three different original objective function pairs adapted based on the mathematical models with the selected optimal algorithm parameters.

A. Performance analysis of ANN-aided modeling

Since the success of the proposed CSA against traditional algorithms was given in a recent study [28], no additional comparison was included in this study. Instead, since the optimization processes take a long time, ANN modeling support was used for acceleration, thus eliminating the extra hardware cost that may be needed. In this part of the study, experiments were carried out for different population values by choosing maximum iteration=30, which is parallel to the study in the literature. In order to see the difference in the graphs more clearly, the results are shown for two different cases, with and without ANN modeling support, for population (N)=60, which was found to be the most successful result and which we accepted as the default parameter, in the next part [28]. In Fig. 3, the typical cost and function evaluation number (FEN) change variations with the best performance repetition are shown. The best results from 10 different studies are selected and exhibited for both cases. With ANN modeling support, the step to reach the minimum cost was reduced from 30 to 25. Therefore, optimum was reached approximately 20% earlier. In addition, as shown in Fig. 3, ANN modeling and the archive section created with these models were included at the beginning of the application. As a result of skipping the calculation part of the objectives, it was seen that the application time was reduced by approximately six times.

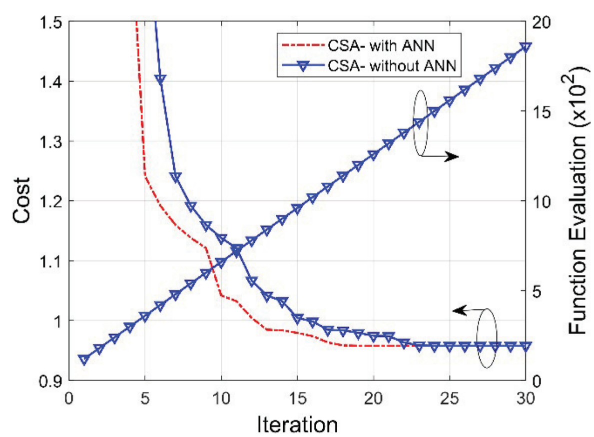

Fig. 3. Typical cost and FEN variations with iteration of the best performance of CSA selected from 10 runs for optimization.

B. Optimal parameter set selection for optimization

Since CSA is a population-based algorithm, the selection of the population size is of great importance [29]. Considering both the possibility of being stuck in the local optimum and the waste of resources, this value should be chosen as the most optimum [37]. Performance comparisons were made over the *cost* (13) function by using OFp_{11}-OFp_{12}-OFs_{11}-OFs_{12} (1,2,3,4) among the objective function pairs determined with population (N)=30, 60 and 100 values in order for the study to be based on solid foundations. The results obtained are shown in Fig. 4 as typical variations of *cost* and FEN

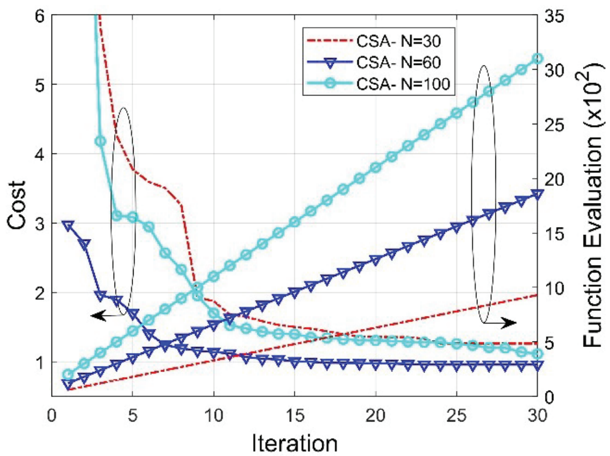

Fig. 4. Typical cost and FEN variations with iteration of the best performance selected from among 10 runs based on population parameter selection.

with the repetition of the best performance selected from 10 different studies. In addition, the *cost* and FEN variations in Fig. 4 are given in Table 2. Among the results obtained for this study, it is seen that the population (N) value which gives the result with the lowest minimum and average cost is 60.

Table 2: Performance evaluations of algorithm by population parameter for results in Fig. 4 (maximum iteration=30)

Population		Minimum	Maximum	Mean
30	Cost	1.262	10.815	2.583
	FEN	750	60	930
60	Cost	0.958	2.978	1.239
	FEN	1500	120	1860
100	Cost	1.113	10.174	2.170
	FEN	2500	200	3100

C. Performances of different objective functions

The objective functions determined in the optimization process are primarily tried to converge to zero in proportion to their weight coefficients. For this reason, objective functions are critically important for an optimization problem. In this section, we have detailed mathematical calculations in the previous section in order to find S_{11} as small as possible (maximum -10 dB) in the bandpass part, and close to 0 in S_{21}, and as small as possible (-10 dB) in S_{21} in the bandstop part and close to 0 in S_{11}. Experiments were made using three different model objective function pairs adapted from the models. The best result obtained using OFp_{11}-OFp_{12}-OFs_{11}-OFs_{12} (1,2,3,4) is given in Fig. 5 as typical magnitude-frequency variation of S_{11}-S_{21} between

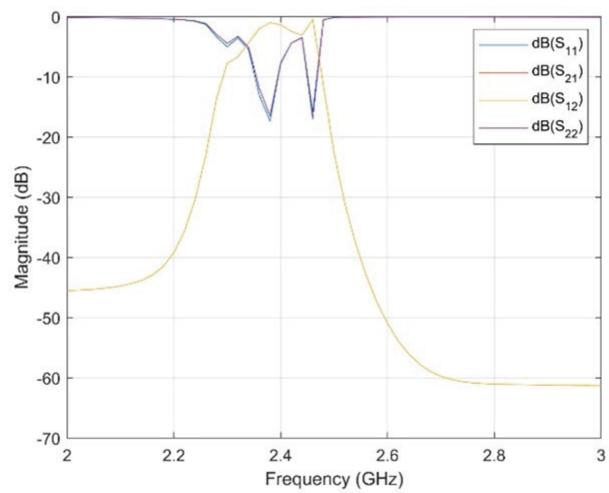

Fig. 5. S parameters of the bandpass filter obtained using MATLAB with the polynomial model objective function.

4 GHz and 5 GHz. Likewise, the most successful result obtained using OFp_{21}-OFp_{22}-OFs_{21}-OFs_{22} (5,6,7,8) is given in Fig. 6 as typical magnitude-frequency variation of S_{11}-S_{21} between 4 GHz and 5 GHz. Finally, the most successful result obtained using OFp_{31}-OFp_{32}-OFs_{31}-OFs_{32} (9,10,11,12) is given in Fig. 7 as typical magnitude-frequency variation of S_{11}-S_{21} between 4 GHz and 5 GHz. In addition, the design parameter values found as a result of this optimization are given numerically in Table 3. When all these results are considered together, it is seen that the most successful result with wider frequency bandwidth and better return loss is found by using OFp_{21}-OFp_{22}-OFs_{21}-OFs_{22} (5,6,7,8), which is called the Power Model.

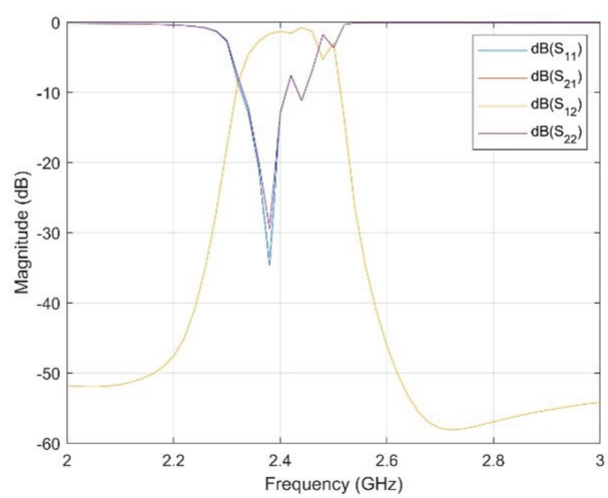

Fig. 6. S parameters of the bandpass filter obtained using MATLAB with the power model objective function.

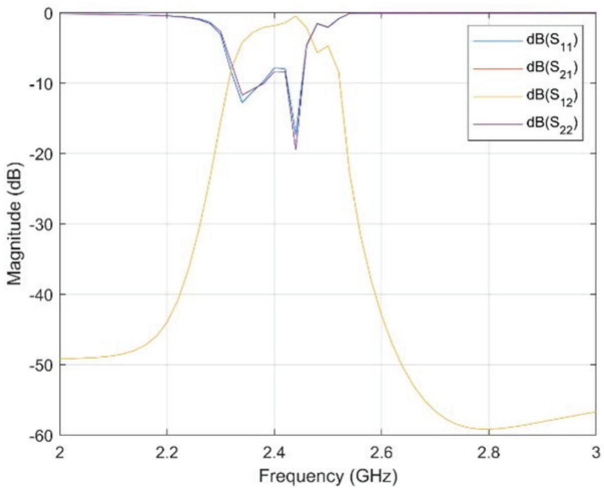

Fig. 7. S parameters of the bandpass filter obtained using MATLAB with the exponential model objective function.

Table 3: Performance evaluations of algorithm by population parameter for results in Figs. 5–7 (maximum iteration=30)

Parameter	Polynomial Model Value (mm)	Power Model Value (mm)	Exponential Model Value (mm)
PortLineLength	17.47	**34.21**	27.81
PortLineWidth	4.25	**4.78**	4.92
CoupledLineLength	[22.7 22.7 22.7 22.7 22.7 22.7]	**[22.28 22.28 22.28 22.28 22.28 22.28]**	[22.28 22.28 22.28 22.28 22.28 22.28]
CoupledLineWidth	[2.36 4.85 4.85 4.85 4.85 2.36]	**[3.79 5.01 5.01 5.01 5.01 3.79]**	[3.24 5.1 5.1 5.1 5.1 3.24]
CoupledLineSpacing	[0.24 2.29 2.29 2.29 2.29 0.24]	**[0.12 2.29 2.29 2.29 2.29 0.12]**	[0.16 2.13 2.13 2.13 2.13 0.16]
GroundPlaneWidth	54.97	**54.34**	46.98

V. DISCUSSION

At the beginning of the study, modeling support was not added because the optimization processes were short for a computer with powerful hardware. Since the optimization processes became undesirably long with additional trials, the flow of the study was directed to modeling-supported optimization. A much longer model (8-9 rows) could have been preferred from an architectural perspective. However, this would only extend the processes, and it would be unknown whether it would have any effect on the verification of the successful implementation. In future studies, it is possible to make the processes faster by changing the network used in modeling support. A suggested approach for longer-lasting models such as antenna optimization can also be tried.

VI. CONCLUSION

In this study, a new variant CSA in the literature of a combined line filter with a center frequency of 2.45 GHz, three of which contain six different variable parameters in themselves, in total eight design parameters, is considered as a multi-dimensional and single-objective optimization problem. The study started with the performance measurements of the modeling-supported shortening of the optimization processes. Then, it continued with the selection of the optimum population parameter considering both the possibility of getting stuck in the local optimum and the waste of resources. The linear and nonlinear objective functions used in the study are completely original and have been specially designed for the bandpass filter model, one of the mathematical models. Although the CSA model preferred in the study is a very new optimization algorithm, it has not yet been encountered in any filter design optimization problem in the literature. In addition, the variant model used played an active role in finding more performance results in another study [28]. The study aimed to find the optimum filter design dimensions. In all these selections, objective function pairs played an active role as well as algorithm parameters. Compared to other results, the most successful result with wider frequency bandwidth and better return loss was obtained using OFp_{21}-OFp_{22}-OFs_{21}-OFs_{22} (5,6,7,8) adapted from the power model. The study discussed includes many innovations with all these aspects and sheds light on future studies. It shows that this algorithm, which can overcome the problems of filter designers, can be a safe, practical and efficient solution for multi-dimensional optimization applications. Henceforth, CSA can undoubtedly be adapted by changing the objective functions for any optimization problem with a large number of design parameters.

REFERENCES

[1] A. Uluslu, “Microstrip Low Pass Filter Analysis and Design,” in *Research & Reviews in Engineering- Gece Kitaplığı Yayınevi*, Gece Kitaplığı Yayınevi, 2021.

[2] J. Hong and M. J. Lancaster, *Microstrip Filters for RF/Microwave Applications*. Hoboken, NJ: Wiley, 2001.

[3] S. B. Cohn, “Parallel-coupled transmission-line-resonator filters,” *IEEE Trans Microw Theory Tech*, vol. 6, no. 2, pp. 223-231, Apr. 1958.

[4] G. L. Matthaei, “Design of wide-band (and narrow-band) band-pass microwave filters on the insertion loss basis,” *IEEE Trans. Microw. Theory Tech.*, vol. 8, no. 6, pp. 580-593, Nov. 1960.

[5] S. S. Olokede and B. S. Paul, “Design of a narrow-band microstrip ring resonator bandpass filter,” in *2017 Progress In Electromagnetics Research*

Symposium - Spring (PIERS), pp. 1835-1841, May 2017.

[6] L. Zhu, S. Sun, and R. Li, *Microwave Bandpass Filters for Wideband Communications*, *vol. 20.* Hoboken, NJ: Wiley, 2012.

[7] C.-S. Ye, Y.-K. Su, M.-H. Weng, C.-Y. Hung, and R.-Y. Yang, "Design of the compact parallel-coupled lines wideband bandpass filters using image parameter method," *Progress In Electromagnetics Research*, vol. 100, pp. 153-173, 2010.

[8] M. Makimoto and S. Yamashita, "Bandpass filters using parallel coupled stripline stepped impedance resonators," *IEEE Trans. Microw. Theory Tech.*, vol. 28, no. 12, pp. 1413-1417, Dec. 1980.

[9] C. J. Kikkert, "A design technique for microstrip filters," in *2008 2nd International Conference on Signal Processing and Communication Systems*, pp. 1-5, Dec. 2008.

[10] D. Ahn, C.-S. Kim, M.-H. Chung, D.-H. Lee, D. W. Lew, and H. J. Hong, "The design of parallel coupled line filter with arbitrary image impedance," in *1998 IEEE MTT-S International Microwave Symposium Digest*, pp. 909-912, 1998.

[11] E. G. Cristal, "Tapped-line coupled transmission lines with applications to interdigital and combline filters," *IEEE Trans. Microw. Theory Tech.*, vol. 23, no. 12, pp. 1007-1012, Dec. 1975.

[12] K. W. Kim, C.-H. Park, and S.-J. Han, "A new design procedure of tapped coupled-line filters," in *IEEE Antennas and Propagation Society Symposium,* pp. 2863-2866, 2004.

[13] J. Ossorio, J. Vague, V. E. Boria, and M. Guglielmi, "Exploring the tunability range of classic circular waveguide dual mode filters using EM-based CAD," in *2017 IEEE MTT-S International Conference on Numerical Electromagnetic and Multiphysics Modeling and Optimization for RF, Microwave, and Terahertz Applications (NEMO)*, pp. 332-334, May 2017.

[14] G. Mansour, M. K. A. Rahim, and H. A. Aldeeb, "Cross-coupled microstrip bandpass filters with finite frequency transmission zeros," in *2021 IEEE 1st International Maghreb Meeting of the Conference on Sciences and Techniques of Automatic Control and Computer Engineering MI-STA*, pp. 684-688, May 2021.

[15] T. Mahouti, T. Yıldırım, and N. Kuşkonmaz, "Artificial intelligence-based design optimization of nonuniform microstrip line band pass filter," *International Journal of Numerical Modelling: Electronic Networks, Devices and Fields*, vol. 34, no. 6, Nov. 2021.

[16] A. Uluslu, "Design of microstrip filter by modeling with reduced data," *Applied Computational Electromagnetics Society (ACES) Journal*, vol. 36, no. 11, pp. 1453-1459, Dec. 2021.

[17] T. Ragani, N. A. Touhami, and M. Agoutane, "Designing a microstrip coupled line bandpass filter," *International Journal of Engineering & Technology*, vol. 2, no. 4, p. 266, Sep. 2013.

[18] M. Sasic and S. T. Imeci, "Design of microstrip coupled-line bandpass filter," *Heritage and Sustainable Development*, vol. 3, no. 1, pp. 44-52, Apr. 2021.

[19] S. Vikash, K. Natarajan, B. Sri Hari, B. Sri Pragathi, T. Poornima, and S. Natarajamani, "Multi-objective optimization of cross coupled resonators based microstrip bandpass filter using PSO," in *2020 5th International Conference on Communication and Electronics Systems (ICCES)*, pp. 322-325, June 2020.

[20] H. Oraizi and N. Azadi-Tinat, "A novel method for the design and optimization of microstrip multi-section bandpass combline filters," in *2006 European Microwave Conference*, pp. 1217-1220, Sep. 2006.

[21] T. Singh, J. Chacko, N. Sebastian, R. Thoppilan, A. Kotrashetti, and S. Mande, "Design and optimization of microstrip hairpin-line bandpass filter using DOE methodology," in *2012 International Conference on Communication, Information & Computing Technology (ICCICT)*, pp. 1-6, Oct. 2012.

[22] E. V. Navin Baaskar, R. Harshini, T. Poornima, and S. Natarajamani, "Design of microstrip bandpass filter based on genetic optimization," in *2019 International Conference on Communication and Electronics Systems (ICCES)*, pp. 1237-1239, July 2019.

[23] V. A. Karpova and N. V. Ivanov, "Optimization of a microstrip tunable bandpass filter design," in *2021 IEEE Conference of Russian Young Researchers in Electrical and Electronic Engineering (ElConRus)*, pp. 129-132, Jan. 2021.

[24] F. Gunes, A. Uluslu, and P. Mahouti, "Pareto optimal characterization of a microwave transistor," *IEEE Access*, vol. 8, pp. 47900-47913, 2020.

[25] F. Kiani, A. Seyyedabbasi, and P. Mahouti, "Optimal characterization of a microwave transistor using grey wolf algorithms," *Analog Integr Circuits Signal Process*, vol. 109, no. 3, pp. 599-609, Dec. 2021.

[26] F. Güneş, S. Demirel, and P. Mahouti, "Design of a front-end amplifier for the maximum power delivery and required noise by HBMO with support vector microstrip model," *Radioengineering*, vol. 23, no. 1, pp. 134-143, 2014.

[27] F. Güneş, S. Demirel, and P. Mahouti, “A simple and efficient honey bee mating optimization approach to performance characterization of a microwave transistor for the maximum power delivery and required noise,” *International Journal of Numerical Modelling: Electronic Networks, Devices and Fields*, vol. 29, no. 1, pp. 4-20, Jan. 2016.

[28] A. Uluslu, “Chameleon swarm algorithm assisted optimization of U-slot patch antenna for quad-band applications,” *IEEE Access*, vol. 10, pp. 74152-74163, 2022.

[29] M. S. Braik, “Chameleon swarm algorithm: A bio-inspired optimizer for solving engineering design problems,” *Expert Syst. Appl.*, vol. 174, p. 114685, July 2021.

[30] I. J. Bahl and D. K. Trivedi, “A designer’s guide to microstrip line,” *Microwaves*, vol. 16, pp. 174-182, May 1977.

[31] X. Wu, Y. Li, and X. Liu, “High-order dual-port quasi-absorptive microstrip coupled-line bandpass filters,” *IEEE Trans. Microw. Theory Tech.*, vol. 68, no. 4, pp. 1462-1475, Apr. 2020.

[32] S. Chatterjee, T. K. Das, and B. Gupta, “Harmonic suppression in in-line parallel-coupled microstrip bandpass filter by Minkowski fractals,” in *2017 Mediterranean Microwave Symposium (MMS)*, pp. 1-4, Nov. 2017.

[33] S. R. Choudhury, A. Sengupta, and S. Das, “Bandpass filters using multilayered microstrip structures,” in *2018 Emerging Trends in Electronic Devices and Computational Techniques (EDCT)*, pp. 1-3, Mar. 2018.

[34] R. A. Rahim, S. I. S. Hassan, M. N. Junita, and N. A. M. Damrah, “Microstrip dual-band bandpass filter for ISM band applications,” in *2015 IEEE International Conference on Control System, Computing and Engineering (ICCSCE)*, pp. 281-286, Nov. 2015.

[35] M. B. Priya, K. Ramprakash, P. Pavithra, and D. A. Joe, “A cost effective dual band Chebyshev parallel coupled microstrip line bandpass filter for ISM band applications,” in *2017 International Conference on Wireless Communications, Signal Processing and Networking (WiSPNET)*, pp. 623-626, Mar. 2017.

[36] M. Jain, V. Singh, and A. Rani, “A novel nature-inspired algorithm for optimization: Squirrel search algorithm,” *Swarm Evol. Comput.*, vol. 44, pp. 148-175, Feb. 2019.

[37] C. R. Reeves and J. E. Rowe, *Genetic Algorithms—Principles and Perspectives, vol. 20*. Boston, MA: Springer US, 2002.

Ahmet Uluslu received his Ph.D. from Istanbul Yıldız Technical University Electronics and Communication Engineering Department in 2020. He completed his master’s degree at the Department of Electromagnetic Fields and Microwave Techniques from the same university. He is working as an associate professor at Istanbul University - Cerrahpaşa Electronics and Automation Department. His current research areas are microwave circuits, especially optimization techniques of microwave circuits, antenna design optimization-modelling, surrogate-based optimization and artificial intelligence algorithm applications.

Performance Comparison Between Fingerprinting-based RSS Indoor Localization Techniques at WLAN Frequencies: Simulation Study

Huthaifa Obeidat[1], Eyad Alzuraiqi[2], Issam Trrad[1], Nouh Alhindawi[3,4], and Mohammad R. Rawashdeh[2]

[1]Faculty of Engineering
Jadara University, Irbid, Jordan
h.obeidat@jadara.edu.jo, itrrad@jadara.edu.jo

[2]Hijjawi Faculty for Engineering Technology
Yarmouk University, Irbid, Jordan
eyad.zuraiqi@yu.edu.jo, alrwashd@yu.edu.jo

[3]Faculty of Sciences and Information
Jadara University, Irbid, Jordan
hindawi@jadara.edu.jo

[4]Ira A. Fulton Schools of Engineering, School of Computing and Augmenting Intelligence (SCAI)
Arizona State University, Arizona, USA
nalhinda@asu.edu

Abstract – This paper presents a performance comparison between two fingerprinting-based received signal strength (RSS) indoor localization techniques at wireless local-area network (WLAN) frequencies: 2.4 GHz and 5.8 GHz. The investigated algorithms include the comparative RSS (CRSS) and vector algorithms. The study was conducted using Wireless InSite ray-tracer software. The simulation was conducted in a simulated environment on the 3rd floor of the Chesham Building, University of Bradford, UK. Also, we presented an estimator which looks at the correlation between the test point RSS and the reference point RSS. The estimator performance is compared to the root mean square error (RMSE) performance. It was found that the CRSS algorithm suffers from the similarity problem while constructing the radio map, and it also suffers from ambiguity problems during localization. The vector algorithm outperforms CRSS algorithms in both frequencies and does not suffer from similarity or ambiguity problems. The proposed estimator shows better performance at both frequencies.

Index Terms – Indoor localization, received signal strength (RSS), Wireless InSite, wireless local-area network (WLAN).

I. INTRODUCTION

Localization has become essential for pervasive applications, including medical healthcare, behavior recognition, and smart buildings [1]. Localization in outdoor environments has been resolved thanks to global navigation satellite systems (GNSS), such as the global positioning system (GPS), the European GALILEO, the Russian GLONASS, and the Chinese BeiDou Satellite Navigation System. Using GNSS, the customer can infer the whereabouts of his location by using received satellite signals from his smartphone. Unfortunately, the GNSS signal cannot penetrate through buildings; therefore, the demand to localize people and items inside indoor environments encouraged researchers to utilize other technologies for localization, including Wi-Fi [2], satellite [3], inertial [4], magnetic [5], ultrasound [6], infrared [7], frequency modulation (FM) waves [8], ZigBee [9], Bluetooth [10], ultra-wideband (UWB) [11], and radio-frequency identification (RFID) [12].

In [13], the authors summarized the usage percentage of localization techniques in indoor environments, as seen in Table 1. RF-based techniques are widely used in indoor environments, representing 73% of all adopted indoor localization techniques. Wi-Fi is the most used technology within the RF-based techniques category, followed by Bluetooth. Hybrid technologies were introduced to enhance accuracy. Table 2 presents the pros and cons of using RF technologies in localization within indoor environments.

Wi-Fi technology is widely used globally since the infrastructure is implanted in most commercial,

Submitted On: September 11, 2024
Accepted On: December 3, 2024
https://doi.org/10.13052/2024.ACES.J.391208

Table 1: Usage percentage of localization technologies in indoor environments

Localization Technique		Usage Percentage	
Infrared		9%	
Ultrasound		6%	
GPS		4%	
Magnetic		1%	
Vision		1%	
Other		6%	
RF Positioning	Wi-Fi	24%	73%
	Bluetooth	17%	
	RFID	7%	
	Ultra-Wideband	6%	
	UHF	4%	
	Cellular	1%	
	Hybrid	6%	
	Cooperative Sensor-Based	8%	

Table 2: Advantages and disadvantages of RF technologies used in indoor localization

Technology	Advantage	Disadvantage
Wi-Fi	Low cost Widely deployed	Requires training
Bluetooth	Low cost Smartphones can collect signals	Requsires training
RFID	Low cost High accuracy	Deployment is tiresome Coverage area is small
Ultra-Wideband	High accuracy	Expensive Requires special equipment
mm-wave technology	Massive bandwidth High accuracy	Huge penetration losses
Cellular	Low cost	Low accuracy

industrial, educational, and residential facilities [14]. Additionally, smartphones can be used as receivers, which makes the technology cheap. The main challenge for localization using Wi-Fi technology is to reach the cm-level accuracy. Within the Wi-Fi data, many signal measures can be used for localization, RSS, channel state information (CSI) and round trip time (RTT), time of arrival, and angle of arrival [14].

RSS is the most popular measure. The data are collected from the surrounding access points (APs) at each location. If the RSS is less than the receiver sensitivity, the signal is said to be undetected [15]. Triangulation and fingerprinting techniques use RSS data for localization [16, 17]. RSS is sensitive to the effect of superimposition of multipath signals of different phases; therefore, by taking the mean value of the locally close RSS values, the effect of fast fading is reduced [18].

By averaging over access points with multiple frequencies and/or heights, the variation of recorded RSS becomes less. The less variation, the more monotonic relationship between distance from access point and recorded RSS; therefore, localization error becomes less [19].

Channel properties of a communication link, also known as CSI, can be used for Wi-Fi localization, discriminating multipath, and increasing localization accuracy. Compared to RSS, the CSI is more stable [20]. However, Wi-Fi network interference cards are needed [21]. RTT is distinguished from time of arrival (TOA) and time difference of arrival (TDOA) as it does not require clock synchronization between the transmitter and receiver [22]. The transmitter sends a message to the receiver and records the timestamp, the receiver sends back an acknowledgment, and then the transmitter estimates the RTT. However, both transmitter and receiver have error measurements due to processing time and phase noise [23].

The TOA method measures travel time between the AP and the receiver. The distance is calculated by multiplying the TOA by the speed of light, and both the transmitter and receiver must be synchronized [24]. For 2D localization, 3 APs are required to perform trilateration. For 3D scenarios, 4 APs are needed. This technique requires larger bandwidth (BW). For example, using a 10 MHz BW, the time resolution will be 10^{-7} s, and the error will be up to 30 m. However, using a 1 GHz BW, the time resolution will be 10^{-9} s, and the error will be reduced to about 0.03 m. Therefore, it is widely used with UWB positioning technologies [25]. The enormous BW available in the 5G and 6G networks will make the utilization of TOA in localization more realizable [26, 27].

The angle of arrival (AOA) can be calculated by estimating the phase differences on the antenna elements. Estimation using AOA requires 2 APs for 2D localization and 3 APs for 3D localization. However, the cost is relatively high compared to other techniques. Additionally, AOA techniques suffer from multipath and low signal-to-noise ratios [28]. In [29], authors proposed a hybrid technique that combines TOA and AOA. This reduced the number of APs needed, the system required large BW, and it leverages the benefits from both techniques.

In this paper, we compared the localization performance of two radio-frequency algorithms at the wireless local-area network (WLAN) frequencies. The investigated algorithms are fingerprinting-based algorithms, including the comparative received signal strength (CRSS) algorithm and the vector algorithm. This work is an extension of the work done in [30]; however, we adopted different frequencies.

Also, we proposed an estimator that considers the correlation between the test point (TP) RSS and the reference point (RP) RSS while estimating the closest RP to the TP. The estimator checks the similarity between the RSS received at a TP from an AP and other RSS values collected at all RPs from the same AP. This process is for all APs in the facility. By taking the summation of likenesses, the closest RP to the TP will be the one with maximum likeness. The order of this paper is as follows. Section II investigates the examined algorithms. Section III presents the methodology and simulation setup, section IV discusses the results, and conclusions are drawn in section V.

II. INVESTIGATED ALGORITHMS

The proposed algorithms are radio-frequency fingerprinting-based algorithms, where data are collected from known locations. A radio map is constructed by mapping the received signal strength (RSS) data collected from each receiver point to its location. This stage is known as the offline phase. In the next stage (the online phase), RSS data are collected from unknown locations termed TP and, by using the radio map, the TP data are compared to the radio-map database. The RP with the lowest RSS difference is assumed to be the closest RP.

In this study, we compared two algorithms. The first algorithm is the vector algorithm [31], where data collected are stored in vectors, and each vector represents the RSS collected at the RP from the surrounding APs. TP data are also stored as a vector. The TP vector is compared to each vector in the radio map by estimating the root mean square error (RMSE) between the TP-RSS vector and each RP-RSS vector in the radio map. The RP whose vector achieves the lowest RMSE is said to be the closest location to the TP. The RMSE between the RSS values of the j^{th} RP and the TP is given by:

$$e_j = \sqrt{\frac{\sum_{i=1}^{N}(c_{ij}-t_i)^2}{N}}, \tag{1}$$

where N is the number of the APs, t_i is the RSS collected at TP from the i^{th} AP, and c_{ij} is the RSS collected by the j^{th} RP from the i^{th} AP.

RMSE is a popular metric since it is understandable by showing the average error in the same units as the data. It highlights larger errors, which is beneficial for avoiding big errors. RMSE is widely used as it provides a comprehensive measure of accuracy by combining the average and variability of errors, making it easy to compare results across different studies and models [32].

Another popular estimator is the mean average error (MAE). The MAE is easy to understand, robust to outliers, and it performs well even when the target variable has skewed distributions. The MAE between the RSS values of the k^{th} RP and the TP is given by:

$$ee_k = \frac{1}{N}\sum_{i=1}^{N}|c_{ik}-t_i|. \tag{2}$$

We introduced another estimator, which sees how similar the RSS collected at a TP is from an AP to other RSS values collected at all RPs from the same AP. The likeness percentage (LP) is estimated by:

$$l_i = 1-\left|\frac{c_{ij}-t_i}{c_{ij}}\right|. \tag{3}$$

When l equals 1, both TP and RP record the same RSS from an AP; the more l approaches one, the more the likeness between TP and RP. For all APs in the facility, the summation of likenesses is taken as shown in (4); the closest RP to the TP will be the one with maximum likeness:

$$L = \sum_{i=1}^{N} l_i = \sum_{i=1}^{N} 1-\left|\frac{c_{ij}-t_i}{c_{ij}}\right|. \tag{4}$$

Using different estimators in localization is common, as in [33], where authors proposed using Spearman distance instead of Euclidean distance. The simulation results show improved results. The LP estimator searches for similarity instead of difference. Rather than exaggerating the effect of enormous errors, the error levels are equally treated.

The second algorithm is the CRSS, where at each RP/TP RSS vector, the algorithm compares each RSS value of the vector with the other values collected in the same vector. The comparison was made based on the following equation [34]:

$$M_N = [c_{ik}] \qquad i,\, k = 1,\, 2, \ldots,\, N, \tag{5}$$

$$c_{ik} = \begin{cases} +1 & R_i > R_k > R_{sens} \\ -1 & R_k > R_i > R_{sens} \\ 0 & R_i = R_k > R_{sens} \\ +2 & R_i > R_{sens} > R_k \\ -2 & R_k > R_{sens} > R_i \\ +3 & R_{sens} > [R_k, R_i] \end{cases}, \tag{6}$$

where M_N is the constructed matrix, R_i is the RSS value to be compared to other RSS values R_k, and R_{sens} is the receiver sensitivity. Both i and k range from 1 to N. For example, if the RSS vector was v=[−59.59 −34.1 −59.02 −100 −95], then the generated CRSS matrix is given as:

$$\text{CRSS} = \begin{bmatrix} 0 & -1 & -1 & +2 & +2 \\ +1 & 0 & +1 & +2 & +2 \\ +1 & -1 & 0 & +2 & +2 \\ -2 & -2 & -2 & 0 & +3 \\ -2 & -2 & -2 & +3 & 0 \end{bmatrix}. \tag{7}$$

This process is accomplished for every RSS vector in the radio map; the resultant matrices are saved as a new radio map. During localization, the RSS of the TP-RSS vector is converted into a CRSS matrix and then compared to the new radio map. The closest location is the RP, with the lowest RMSE between its corresponding CRSS matrix and the TP-CRSS matrix.

Fingerprinting localization is one of the most common techniques. The investigated algorithms include the CRSS algorithm and the vector algorithm. In a previous paper, the performance between the two algorithms is tested at a lower frequency of 400 MHz [30]; in this paper, the performance is examined at microwave frequencies 2.4 and 5.8 GHz. The target of this study is to examine the robustness of the CRSS algorithm at microwave frequencies.

III. METHODOLOGY AND SIMULATION SETUP

The simulations were done using Wireless InSite® (WI) ray-tracing software, which has been validated over WLAN frequencies [35, 36]. In this project, a detailed layout of the 3rd floor of the Chesham Building at the University of Bradford was constructed; the design took into account the materials of the building, including concrete, drywall, glass, and wood.

WI allows modeling the floor as seen in Fig. 1, where the user can change the electrical constitutive parameters (permittivity and conductivity). The user can set up the communication links between transmitters and receivers. This includes the type of antenna used, transmitted power, operating frequency, signal BW, the maximum number of reflections, transmissions, and diffractions, propagation model, ray-tracing method, sum complex electric fields, and the number of propagation paths.

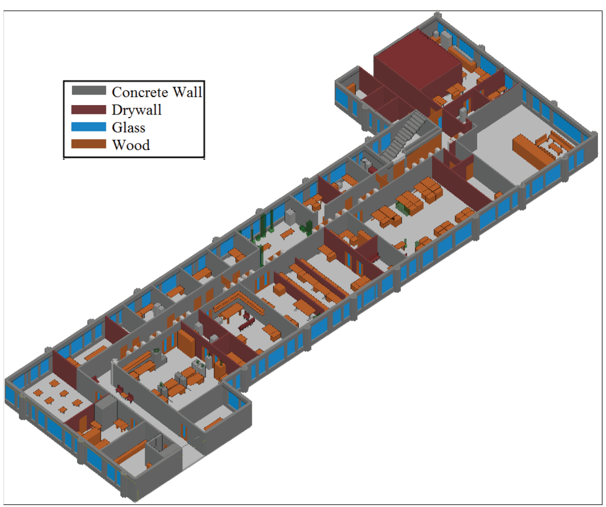

Fig. 1. Simulated environment for the 3rd floor in the Chesham Building, University of Bradford, UK.

Adding more paths, transmissions, reflections, and diffractions will be at the expense of computational time. Sufficient results were found when the maximum number of paths is 10, the number of transmissions is 4, and the number of reflections is 4 [35]. Table 3 summarizes the settings used in the WI software for both operating frequencies: 2.4 GHz and 5.8 GHz. Table 4 presents the permittivity ε_r and conductivity σ values used in our simulations based on the ITU tables [37]. The permittivity does not change considerably with frequency contradictory to the conductivity.

Table 3: Wireless InSite settings for the investigated scenario

Setting	Value
Transmitter antenna	3-elements omnidirectional array
Antenna gain	3.5 (2.4 GHz) 4.5 (5.8 GHz)
Receiver antenna	Omnidirectional
Sum complex electric fields	None
Operating frequency	2.4 GHz 5.8 GHz
Bandwidth	20 MHz (2.4 GHz) 40 MHz (5.8 GHz)
Number of reflections	4
Number of transmissions	4
Number of diffractions	0
Ray-spacing	0.1°
Plane-wave ray spacing	0.5 m
Maximum rendered paths	10
Ray-tracing method	Shooting-and-Bouncing-Rays (SBR)
Ray-tracing acceleration	Octree
Propagation model	full 3D

Table 4: Material properties with frequency

Material	2.4 GHz		5.8 GHz	
	ε_r	σ	ε_r	σ
Concrete	5.31	0.0662	5.31	0.1258
Glass	6.27	0.0122	6.27	0.0314
Wood	1.99	0.0120	1.99	0.0281
Drywall	2.94	0.0216	2.94	0.0378

As mentioned earlier, the localization techniques used in this article are RF-fingerprinting-based algorithms. Figure 2 shows the distribution of the APs, RPs, and TPs. There are 7 APs, 176 RPs, and 85 TPs. The choice of these numbers was based on recommendations from a previous study [30]. In that paper, the effect of adding more APs and RP is examined. It was found that adding more APs will enhance the localization performance; however, the vector and matrix sizes will be

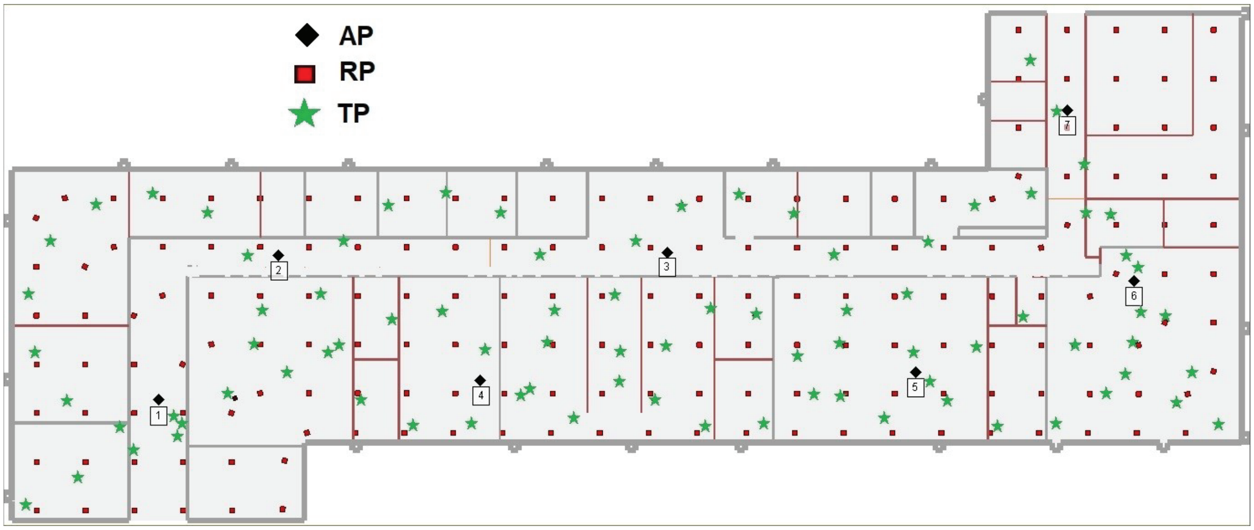

Fig. 2. APs, RPs, and TPs distribution on the 3rd floor of the Chesham Building.

larger. Adding more RPs will enhance the performance up to a certain limit; after that, adding more RPs will not enhance the performance, it may worsen it.

Based on the above, the number of APs and RPs was set to ensure the best performance. Our paper uses 7 APs to ensure that at least 4 APs cover all regions within the floor. We tried to avoid adding redundant RPs; therefore, the RPs were chosen to have space bigger than 10λ. This number is used widely to perform averaging to minimize the fast-fading effect; the window could be up to 22λ. Therefore, the spacing between the RPs will ensure no redundant RPs and, in a practical scenario, the averaging window extends from 10λ to 22λ [19].

In Wireless InSite, the fast fading effect is removed by taking the power sum of incident rays rather than considering the phase [38]. The collected data is given to Matlab code; the code builds up the radio map based on the RPs data, and then each TP data is compared to the radio map by estimating the RMSE, MAE, and LP estimators (equations (1)–(3)). The closest RP is estimated when its corresponding RMSE/MAE value is the least or its corresponding LP value is the maximum. The code also generates the CRSS matrices based on equation (5) and builds up the CRSS radio map. Similarly, the code estimates the closest RP by finding the lowest RMSE/MAE.

IV. RESULTS AND DISCUSSION

Using two RF fingerprinting techniques, we have examined localization accuracy for two algorithms at the two WLAN bands: 2.4 GHz and 5.8 GHz.

A. CRSS algorithm

During the generation of the CRSS matrices, it was observed that many RPs are relatively close to each other and construct the same matrix since the descending (or ascending) order of the APs based on their corresponding RSS level is the same for these RPs. As seen in Fig. 3, each contoured set of RPs indicates that the RPs within the contour generate the same CRSS matrix. We refer to this problem as similarity. In this figure, each black contour surrounds RPs that generate the same CRSS. We found that some RPs generate the same CRSS matrix but are not co-located. Therefore, we used different colors for their contours; for example, there are two purple contours on the right-lower side of Fig. 3, meaning these 4 RPs generate the same CRSS matrix.

When localization was conducted at 2.4 GHz, only 20% of TPs were linked to a single RP. For each TP of the remaining 80%, the estimated location is a group of RPs with the same CRSS matrix or different CRSS matrices. At 5.8 GHz, only 23% of TPs were linked to a single RP. As shown in Fig. 4, the estimated TP is linked to RPs with different CRSS matrices.

As seen, the TP (represented by a black tetragram) is linked to 3 RPs, each with a different CRSS matrix; once localization is performed, these RPs are considered the closest. Also, the TP represented by a red star is linked to 7 RPs, which are represented by 3 CRSS matrices (4 of them are represented by a single CRSS, and the RPs contour color is blue). So, in addition to the similarity problem, we have ambiguity problem, when TP location is linked to different RPs which have different CRSS matrices.

This makes using the CRSS algorithm inefficient; therefore, we do not recommend using this algorithm for localization purposes.

Figure 5 shows a localization error (LE) comparison at the two WLAN frequencies using the CRSS algorithm

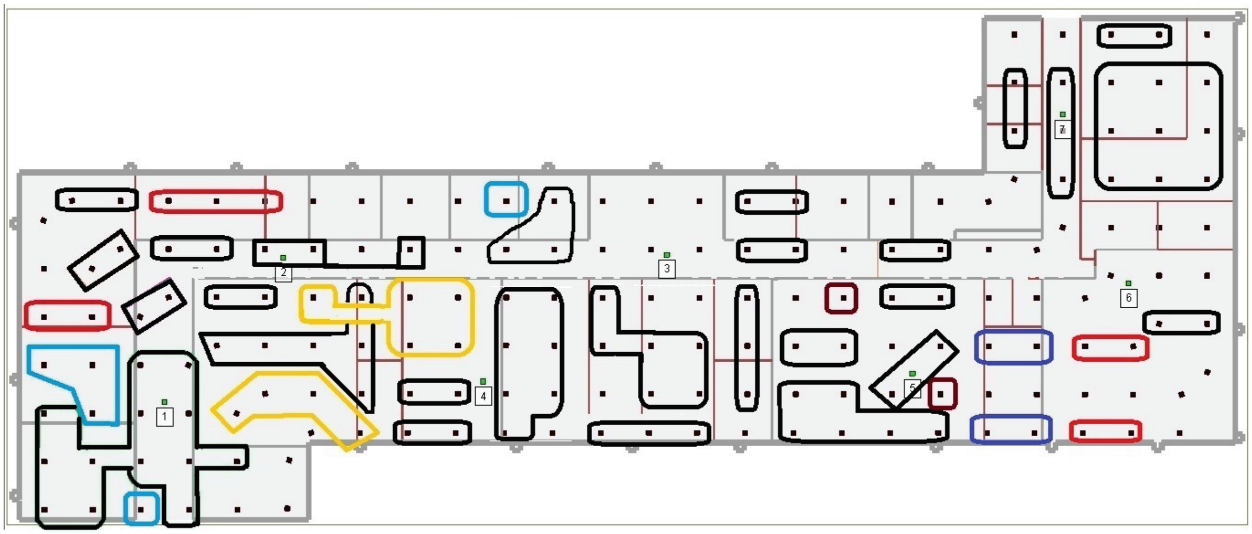

Fig. 3. RPs similarity observed at 5.8 GHz. Table 5 shows how many sets of RPs generate the same CRSS matrix. For example, at 5.8 GHz, we found that the number of cases where 2 RPs generate the same CRSS matrix is 17 cases. Similarly, we found that the number of cases where 3 RPs generate the same CRSS matrix is 5. We also found that 13 RPs generate the same CRSS matrix. Similarity tends to worsen as frequency increases. At 2.4 GHz, only 56 RPs out of 176 generated unique CRSS matrices, which comprise 32.3% of the entire RPs set; however, at 5.8 GHz, only 44 RPs generate unique CRSS matrices, which are 25%. We found that only 33 RPs are free from similarity at both frequencies. The figure shows that similarity occurs more in halls and rooms separated by drywalls. However, they tend to be less in rooms separated by concrete walls. This explains why RPs in the upper half of the figure have less similarity. Therefore, using the CRSS algorithm, lower-resolution radio maps are better since having a high-resolution radio map will lead to similarity. A similar observation was recorded at 2.4 GHz.

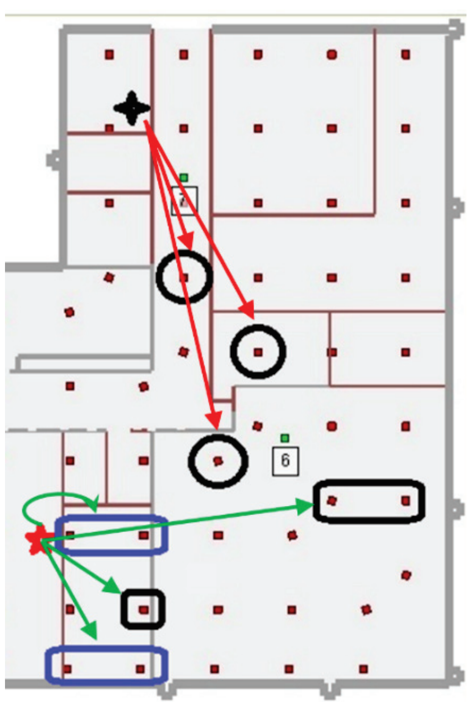

Fig. 4. Example of ambiguity at 5.8 GHz.

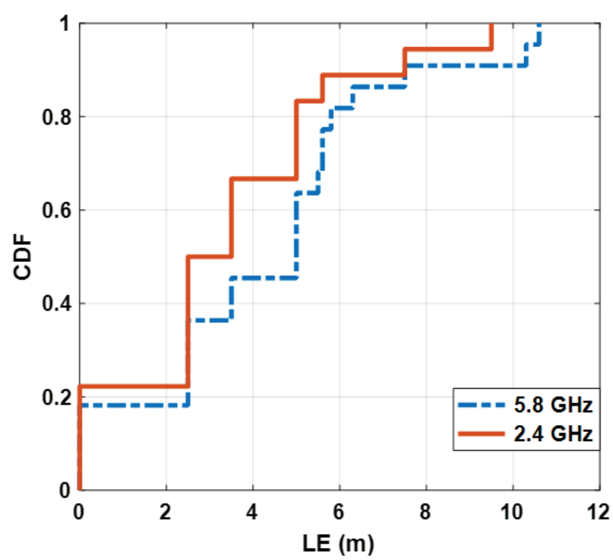

Fig. 5. LE comparison using the CRSS algorithm without the ambiguous cases at the WLAN frequencies.

without considering the ambiguous cases. LE tends to be less at 2.4 GHz when no ambiguity is considered. This means that the accuracy of the CRSS algorithm becomes

Table 5: Total of how many sets of RPs generate the same CRSS matrices

Similarity RPs	2.4 GHz	5.8 GHz
	No. of Cases	No. of Cases
2 RPs generate the same matrix	14	17
3 RPs generate the same matrix	9	6
4 RPs generate the same matrix	3	2
5 RPs generate the same matrix	0	2
6 RPs generate the same matrix	2	4
7 RPs generate the same matrix	3	1
8 RPs generate the same matrix	1	0
9 RPs generate the same matrix	0	2
10 RPs generate the same matrix	1	0
11 RPs generate the same matrix	0	0
12 RPs generate the same matrix	0	0
13 RPs generate the same matrix	0	1
Similarity	67.7%	75%

lower as frequency increases. Also, the similarity effect becomes more significant as frequency increases, as shown in Table 5.

B. Vector algorithm

We have used three estimators: RMSE, MAE, and the proposed LP estimator. Figure 6 shows an LE comparison for each estimator at the two WLAN frequencies. Both RMSE and LP estimators show that localization accuracy decreases as frequency increases; however, MAE shows better performance as frequency increases. For example, using the LP estimator, the probability of localization error less than 2.5 m is 75% and 60% at 2.4 GHz and 5.8 GHz, respectively. Using MAE, the probability for localization error less than 2.5 m is 60% and 50% at 2.4 GHz and 5.8 GHz, respectively. Using RMSE, the probability for localization error less than 2.5 m is 35% and 25% at 2.4 GHz and 5.8 GHz, respectively.

The probability of localization error less than 5 m and 5.5 m is 90% using the LP estimator at 2.4 GHz and 5.8 GHz. Also, 90% of errors are less than 5.5 m and 6 m using the MAE and RMSE estimators at 2.4 GHz and 5.8 GHz, respectively.

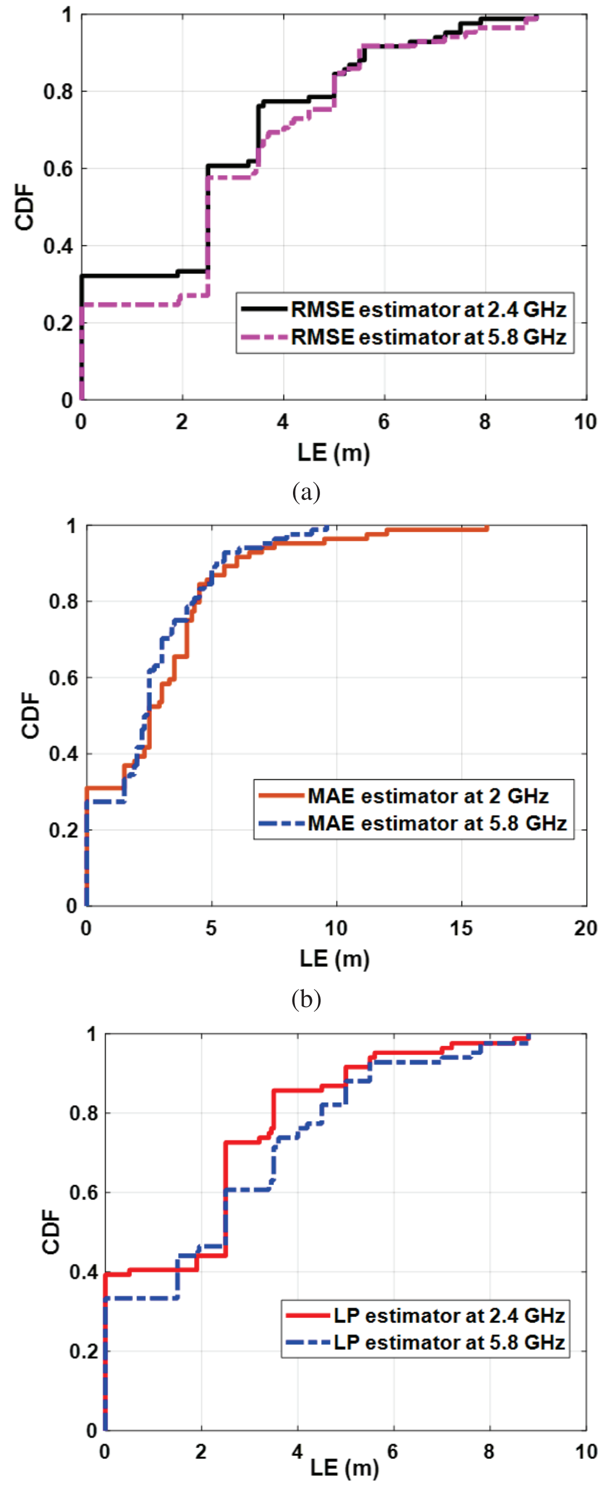

Fig. 6. LE comparison for (a) RMSE estimator, (b) MAE estimator, and (c) LP estimator at the two WLAN frequencies.

Results show that the LP estimator tends to show better performance, as shown in Fig. 7. The LP estimator shows better all-over performance at the two WLAN frequencies; for example, at 2.4 GHz, the probability for localization error less than 3.5 m is 86%, 66%, and 76% using LP estimator, MAE estimator, and RMSE estimator, respectively. At 5.8 GHz, the probability of an error being less than 3.5 m is 71%, 75%, and 66% using the LP, MAE, and RMSE estimators, respectively.

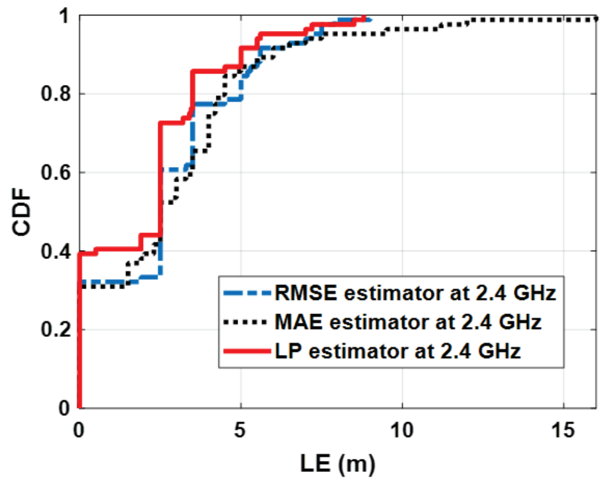

(a)

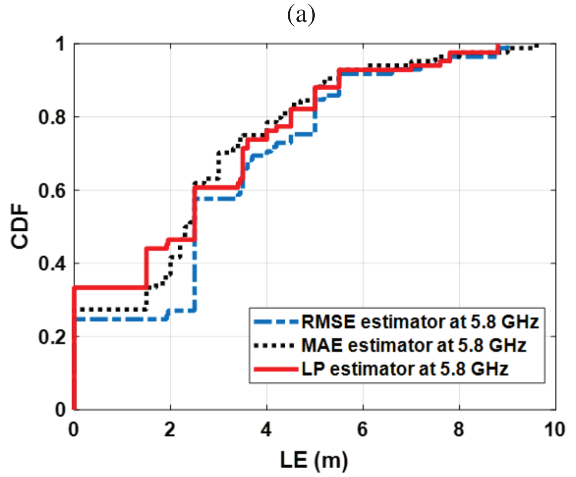

(b)

Fig. 7. LE comparison between the three estimators at (a) 2.4 GHz and (b) 5.8 GHz.

Tables 6 and 7 present a comparison between the three estimators at the two frequencies. The tables show how many estimated RP were the closest to the TP (the accurate), the second closest RP, and the third closest RP. For example, using the LP estimator at 2.4 GHz, for 33 TPs, the estimated location for each TP was the actual closest RP to that TP. For 27 TPs, the estimated location for each TP was the first neighbor to the closest RP. For 12 TPs, the estimated location for each TP was the second neighbor to the closest RP. The tables show that the LP estimator outperforms the MAE and RMSE estimators at the two WLAN frequencies, as provided by the metrics. It can be seen from the figures and the tables that the best estimator is the LP estimator, followed by the MAE estimator. RMSE squares the errors before averaging, giving more weight to larger errors; therefore, it performs less well.

Table 6: Performance comparison between LP, MAE, and RMSE estimators at 2.4 GHz

	2.4 GHz		
	RMSE	**MAE**	**LP**
Accurate RP	27	29	33
1st neighbor	24	14	27
2nd neighbor	15	11	12

Table 7: Performance comparison between LP, MAE, and RMSE estimators at 5.8 GHz

	5.8 GHz		
	RMSE	**MAE**	**LP**
Accurate RP	20	23	28
1st neighbor	28	9	21
2nd neighbor	15	10	17

Figure 8 compares vector and CRSS algorithms when we excluded ambiguity cases at 5.8 GHz. Even when we considered only the cases when the CRSS algorithm detects 1 RP, the vector algorithm performs better. For example, 90% of errors are less than 5.5 m using the vector algorithm, while 90% of errors are less than 7.5 m using the CRSS algorithm.

V. CONCLUSION

A comparison between two radio-frequency localization techniques at WLAN bands is presented. The algorithms include vector and CRSS algorithms, which are fingerprinting-based RSS techniques. The study was performed in a simulated environment on the 3rd floor of the Chesham Building, University of Bradford, UK, using Wireless InSite software. It was found that the CRSS algorithm suffers from similarity and ambiguity problems; both get worse as frequency increases. Therefore, the algorithm is not recommended for indoor positioning. The vector algorithm shows acceptable performance at both frequencies as the probability for an error to be less than 2.5 m is 72.5% at 2.4 GHz and 60% at 5.8 GHz.

Additionally, the performance of the vector algorithm outperforms the CRSS algorithms, even when we do not consider the ambiguity cases. Also, we introduced a new estimator to find which RP is the closest to the TP based on their RSS values;

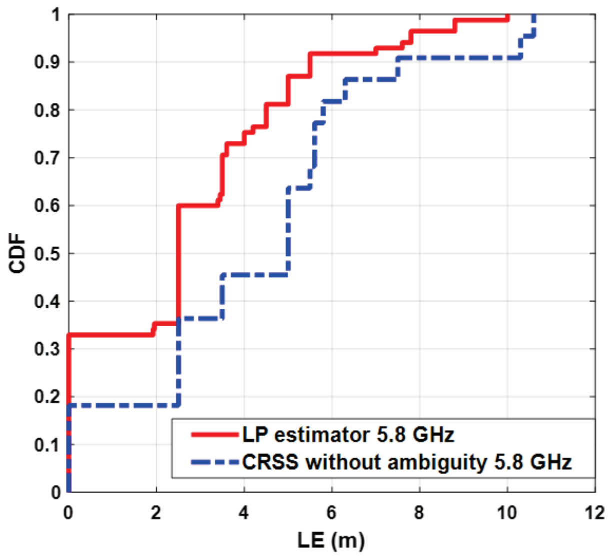

Fig. 8. LE comparison between vector and CRSS algorithms when we excluded the ambiguity cases.

the estimator considers/utilizes the correlation between the RSS collected by the TP and the RSS collected by the RPs. The performance was compared to MAE and RMSE, showing better performance at both frequencies.

REFERENCES

[1] S. Subedi and J.-Y. Pyun, "A survey of smartphone-based indoor positioning system using RF-based wireless technologies," *Sensors*, vol. 20, no. 24, p. 7230, 2020.

[2] V. Bellavista-Parent, J. Torres-Sospedra, and A. Perez-Navarro, "New trends in indoor positioning based on Wi-Fi and machine learning: A systematic review," arXiv Prepr. arXiv2107.14356, 2021.

[3] X. Wan and X. Zhan, "The research of indoor navigation system using pseudolites," *Procedia Eng.*, vol. 15, pp. 1446-1450, 2011.

[4] Z. Chen, Q. Zhu, and Y. C. Soh, "Smartphone inertial sensor-based indoor localization and tracking with iBeacon corrections," *IEEE Trans. Ind. Informatics*, vol. 12, no. 4, pp. 1540-1549, 2016.

[5] P. Davidson and R. Piché, "A survey of selected indoor positioning methods for smartphones," *IEEE Commun. Surv. Tutorials*, vol. 19, no. 2, pp. 1347-1370, 2016.

[6] F. Sainjeon, S. Gaboury, and B. Bouchard, "Real-time indoor localization in smart homes using ultrasound technology," *in Proceedings of the 9th ACM International Conference on Pervasive Technologies Related to Assistive Environments*, pp. 1-4, 2016.

[7] B. Mukhopadhyay, S. Sarangi, S. Srirangarajan, and S. Kar, "Indoor localization using analog output of pyroelectric infrared sensors," *in 2018 IEEE Wireless Communications and Networking Conference (WCNC), IEEE*, pp. 1-6, 2018.

[8] A. Popleteev, V. Osmani, and O. Mayora, "Investigation of indoor localization with ambient FM radio stations," *in 2012 IEEE International Conference on Pervasive Computing and Communications, IEEE*, pp. 171-179, 2012.

[9] A. Billa, I. Shayea, A. Alhammadi, Q. Abdullah, and M. Roslee, "An overview of indoor localization technologies: Toward IoT navigation services," *in 2020 IEEE 5th International Symposium on Telecommunication Technologies (ISTT), IEEE*, pp. 76-81, 2020.

[10] R. Giuliano, G. Cardarilli, C. Cesarini, L. Di Nunzio, F. Fallucchi, R. Fazzolari, F. Mazzenga, M. Re, and A. Vizzarri, "Indoor localization system based on Bluetooth low energy for museum applications," *Electronics*, vol. 9, p. 1055, 2020.

[11] A. Poulose and D. S. Han, "UWB indoor localization using deep learning LSTM networks," *Appl. Sci.*, vol. 10, no. 18, p. 6290, 2020.

[12] W. Shuaieb, G. Oguntala, A. AlAbdullah, H. Obeidat, R. Asif, R. Abd-Alhameed, M. Bin-Melha, and C. Kara-Zaïtri, "RFID RSS fingerprinting system for wearable human activity recognition," *Future Internet*, vol. 12, p. 33, 2020.

[13] C. Esposito and M. Ficco, "Deployment of RSS-based indoor positioning systems," *Int. J. Wirel. Inf. Networks*, vol. 18, no. 4, pp. 224-242, 2011.

[14] X. Feng, K. A. Nguyen, and Z. Luo, "A survey of deep learning approaches for WiFi-based indoor positioning," *J. Inf. Telecommun.*, pp. 1-54, 2021.

[15] H. Obeidat, W. Shuaieb, O. Obeidat, and R. Abd-Alhameed, "A review of indoor localization techniques and wireless technologies," *Wirel. Pers. Commun.*, pp. 1-39, 2021.

[16] Y. Wang, X. Yang, Y. Zhao, Y. Liu, and L. Cuthbert, "Bluetooth positioning using RSSI and triangulation methods," *in 2013 IEEE 10th Consumer Communications and Networking Conference (CCNC), IEEE*, pp. 837-842, 2013.

[17] H. A. Obeidat, W. Shuaieb, H. Alhassan, K. Samarah, M. Abousitta, R. A. Abd-Alhameed, S. M. R. Jones, and J. M. Noras, "Location based services using received signal strength algorithms," *in 2015 Internet Technologies and Applications (ITA), IEEE*, pp. 411-413, 2015.

[18] H. Obeidat, A. A. S. Alabdullah, N. T. Ali, R. Asif, O. Obeidat, M. S. A. Bin-Melha, W. Shuaieb,

R. A. Abd-Alhameed, and P. Excell, "Local average signal strength estimation for indoor multipath propagation," *IEEE Access*, vol. 7, pp. 75166-75176, 2019.

[19] H. Obeidat, M. Al-Sadoon, C. Zebiri, O. Obeidat, I. Elfergani, and R. Abd-Alhameed, "Reduction of the received signal strength variation with distance using averaging over multiple heights and frequencies," *Telecommun. Syst.*, vol. 86, no. 1, pp. 201-211, 2024.

[20] X. Zhu, W. Qu, T. Qiu, L. Zhao, M. Atiquzzaman, and D. O. Wu, "Indoor intelligent fingerprint-based localization: Principles, approaches and challenges," *IEEE Commun. Surv. Tutorials*, vol. 22, no. 4, pp. 2634-2657, 2020.

[21] M. Li, Y. Meng, J. Liu, H. Zhu, X. Liang, Y. Liu, and N. Ruan, "When CSI meets public Wi-Fi: Inferring your mobile phone password via Wi-Fi signals," *in Proceedings of the 2016 ACM SIGSAC Conference on Computer and Communications Security*, pp. 1068-1079, 2016.

[22] G. Guo, R. Chen, F. Ye, X. Peng, Z. Liu, and Y. Pan, "Indoor smartphone localization: A hybrid Wi-Fi RTT-RSS ranging approach," *IEEE Access*, vol. 7, pp. 176767-176781, 2019.

[23] C. Yang and H.-R. Shao, "WiFi-based indoor positioning," *IEEE Commun. Mag.*, vol. 53, no. 3, pp. 150-157, 2015.

[24] C. Gao, G. Wang, and S. G. Razul, "Comparisons of the super-resolution TOA/TDOA estimation algorithms," *in 2017 Progress in Electromagnetics Research Symposium-Fall (PIERS-FALL), IEEE*, pp. 2752-2758, 2017.

[25] A. Poulose, O. S. Eyobu, M. Kim, and D. S. Han, "Localization error analysis of indoor positioning system based on UWB measurements," *in 2019 Eleventh International Conference on Ubiquitous and Future Networks (ICUFN), IEEE*, pp. 84-88, 2019.

[26] T. R. Rao, D. Murugesan, S. Ramesh, and V. A. Labay, "Radio channel characteristics in an indoor corridor environment at 60 GHz for wireless networks," *in 2011 Fifth IEEE International Conference on Advanced Telecommunication Systems and Networks (ANTS), IEEE*, pp. 1-5, 2011.

[27] H. Obeidat and G. T. El Sanousi, "Indoor propagation channel simulations for 6G wireless networks," *IEEE Access*, vol. 12, pp. 133863-133876, 2024.

[28] F. Zafari, A. Gkelias, and K. K. Leung, "A survey of indoor localization systems and technologies," *IEEE Commun. Surv. Tutorials*, vol. 21, no. 3, pp. 2568-2599, 2019.

[29] S. Venkatraman and J. Caffery, "Hybrid TOA/AOA techniques for mobile location in non-line-of-sight environments," *in 2004 IEEE Wireless Communications and Networking Conference (IEEE Cat. No. 04TH8733), IEEE*, pp. 274-278, 2004.

[30] H. A. Obeidat, Y. A. S. Dama, R. A. Abd-Alhameed, Y. F. Hu, R. Qahwaji, J. M. Noras, and S. M. R. Jones, "A comparison between vector algorithm and CRSS algorithms for indoor localization using received signal strength," *Applied Computational Electromagnetics Society (ACES) Journal*, vol. 31, no. 8, pp. 868-876, 2016.

[31] H. A. Obeidat, R. A. Abd-Alhameed, J. M. Noras, S. Zhu, T. Ghazaany, N. T. Ali, and E. Elkhazmi, "Indoor localization using received signal strength," *in 2013 8th IEEE Design and Test Symposium, IEEE*, pp. 1-6, 2013.

[32] S. M. Robeson and C. J. Willmott, "Decomposition of the mean absolute error (MAE) into systematic and unsystematic components," *PLoS One*, vol. 18, no. 2, p. e0279774, 2023.

[33] Y. Xie, Y. Wang, A. Nallanathan, and L. Wang, "An improved K-nearest-neighbor indoor localization method based on spearman distance," *IEEE Signal Process. Lett.*, vol. 23, no. 3, pp. 351-355, 2016.

[34] K. Sayrafian-Pour and J. Perez, "Robust indoor positioning based on received signal strength," *in 2007 2nd International Conference on Pervasive Computing and Applications, IEEE*, pp. 693-698, 2007.

[35] H. A. Obeidat, O. A. Obeidat, M. F. Mosleh, A. A. Abdullah, and R. A. Abd-Alhameed, "Verifying received power predictions of Wireless InSite software in indoor environments at WLAN frequencies," *Applied Computational Electromagnetics Society (ACES) Journal*, vol. 35, no. 10, 2020.

[36] Y. A. S. Dama, R. A. Abd-Alhameed, F. Salazar-Quinonez, D. Zhou, S. M. R. Jones, and S. Gao, "MIMO indoor propagation prediction using 3D shoot-and-bounce ray (SBR) tracing technique for 2.4 GHz and 5 GHz," *in Proceedings of the 5th European Conference on Antennas and Propagation (EUCAP), IEEE*, pp. 1655-1658, 2011.

[37] P. Series, "Effects of building materials and structures on radiowave propagation above about 100 MHz," *Recomm. ITU-R*, pp. 2040-2041, 2021.

[38] H. Obeidat, R. Asif, N. Ali, Y. Dama, O. Obeidat, S. Jones, W. Shuaieb, M. Al-Sadoon, K. Hameed, A. Alabdullah, and R. Abd-Alhameed, "An indoor path loss prediction model using wall correction factors for wireless local area network and 5G indoor networks," *Radio Sci.*, vol. 53, no. 4, pp. 544-564, 2018.

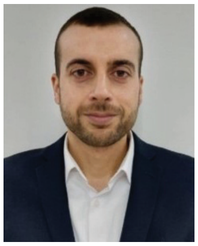

Huthaifa Obeidat is Associate Professor in Communication and Computer Engineering department at Jadara University in Jordan. He received a Ph.D. in Electrical Engineering from the University of Bradford, UK. In 2018, he was awarded an MSc degree in Personal Mobile and Satellite Communication from the same University in 2013. He was awarded the best paper presentation at the 7th International Conference on Internet Technologies and Application (ITA2017). His research interests include Radiowave Propagation, mm wave propagation, e-health applications, and Antenna and Location-Based Services. Obeidat has been an URSI senior member since 2022 and a member of the Jordanian engineering association since 2011.

Eyad Alzuraiqi obtained his Ph.D. in Electrical Engineering from University of New Mexico, USA, in 2012. He joined Yarmouk University, Jordan, as a faculty member. Currently, he is a research associate professor at University of New Mexico, USA. His research interests include Applied and Computational Electromagnetics, Antennas, Neural Networks, and Communications Systems.

Issam Trrad received his bachelor's and master's degrees in electrical & communication engineering at the Ukraine National Academy, Ukraine, in 1999, with high honors GPA. He received his Ph.D. degree in Electrical & Communication Engineering at the Odessa National Academy of Communication, Odessa, Ukraine, in 2003. Currently, he is an Associate Professor in the Department of Electrical and Commuter Engineering at Jadara University. He was Dean of the College of Engineering. He has been a member of the Jordan Engineers Association (JEA) since 2000.

Nouh Alhindawi is an Associate Professor in the field of Software Engineering and Computer Science. Currently, he is an Associate Teaching Professor, Ira A. Fulton Schools of Engineering, School of Computing and Augmenting Intelligence (SCAI), at Arizona State University, USA. Before that, he served as Assistant to the President of Jadara University for Digital Transformation and E-Learning. He brings a wealth of expertise to his role. Notably, he held the esteemed position of Director of Information Technology and Electronic Transformation Directorate at the Ministry of Higher Education and Scientific Research in Jordan (MoHESR) from 2018 to 2022. Alhindawi served as the Director for the Computer Center at Jadara University from 2015 to 2018. Additionally, he has held various faculty positions and acted as the University Advisor for Jadara University in matters pertaining to Digital Transformation Policies. Alhindawi completed his doctoral studies in Computer Science / Software Engineering at Kent State University, USA, in 2013. He holds a master's degree from Al-Balqa Applied University, Jordan, obtained in 2006, and a bachelor's degree from Yarmouk University, Jordan, earned in 2004.

Mohammad R. Rawashdeh is currently an associate professor in the Communications Engineering Department, Yarmouk University, Irbid, Jordan. He got his Ph.D. from Michigan State University, East Lansing, Michigan, USA, in 2018. His research interests include computational electromagnetics, microwave circuits design and analysis, and non-destructive evaluation.

Analysis of Induction-polarization Response Characteristics of Marine Controlled-source Electromagnetic Multiphase Composite Medium

Chunying Gu[1], Suyi Li[1], and Silun Peng[2*]

[1]College of Instrumentation and Electrical Engineering
Jilin University, Changchun 130061, China
cygu20@mails.jlu.edu.cn, lsy@jlu.edu.cn

[2]College of Automotive Engineering
Jilin University, Changchun 130022, China
*pengsilun@jlu.edu.cn

Abstract – The complex composition and structure of the submarine reservoir and its secondary pyrite, which are multiphase composite media, can provoke the induced polarization (IP) effect, resulting in the change of the marine controlled-source electromagnetic (CSEM) induction-polarization response, which directly affects geological interpretation results. In this paper, the generalized effective-medium theory of induced polarization (GEMTIP) model is introduced to study the influence of composition, structure and geometric characteristics of submarine reservoirs and secondary pyrite on the 3D marine CSEM induction-polarization response. We first construct the 3D finite-difference frequency-domain (FDFD) electromagnetic field governing equation based on the GEMTIP model, apply the emission source on the non-uniform grid, and solve the linear equations by using the difference coefficient matrix. Then we perform forward calculation on a typical 1D reservoir model to verify the correctness and effectiveness of the proposed algorithm. Finally, we design the reservoir and secondary pyrite models, and analyze the influence laws of IP parameters and polarization layer geometry parameters on the 3D marine CSEM induction-polarization response. These studies are of great value for understanding the relationship between submarine multiphase composite medium and electromagnetic wave propagation.

Index Terms – GEMTIP model, induced polarization (IP) effect, marine controlled-source electromagnetic (CSEM), reservoir polarization, secondary pyrite polarization.

I. INTRODUCTION

The marine controlled-source electromagnetic (CSEM) method has become an important geophysical method for deep-sea oil exploration, seabed geological structure investigation and marine ecological environment survey due to its advantages of high precision, low cost and wide range [1–7]. In the actual exploration of marine CSEM, multiphase composite media such as submarine oil reservoir and its secondary pyrite are often accompanied by the induced polarization (IP) effect [8–11], that is, under the action of applied electric field, positive and negative charges in the subsea multiphase composite medium will move in a directional way and accumulate to form double electric layers on both sides of the interface. After the applied electric field is turned off, positive and negative charges will return to the original state, thus forming a displacement current in the opposite direction of the applied electric field. This phenomenon will directly affect the measurement results of induction-polarization response of marine CSEM. Therefore, it is necessary to study the IP effect simulation of marine CSEM multiphase composite medium for improving the accuracy of geological interpretation of exploration data.

In recent years, some progress has been made in the simulation of the IP effect of marine CSEM. Wang et al. [12] established two 1D polarized medium models of reservoir generating IP effect based on the Cole-Cole model and analyzed the influence of IP parameters of the two models on electromagnetic response. Huang [13] calculated the 1D marine CSEM electromagnetic response with IP effect and analyzed the influence degree of different Cole-Cole model parameters on the response. Liu et al. [14] combined electromagnetic induction and IP effect, used real resistivity and complex resistivity (Cole-Cole) models to calculate the 1D CSEM response, and evaluated the influence of noise level on electromagnetic response and IP effect on inversion. Ding et al. [15] calculated the 1D and 2D marine CSEM response by introducing the Cole-Cole model and studied the influence of IP effect on marine CSEM

Submitted On: September 25, 2024
Accepted On: January 10, 2025
https://doi.org/10.13052/2024.ACES.J.391209

response. Mittet [16] conducted induction-polarization dual-field forward modeling based on the fictitious wave domain method, calculated the electromagnetic response of marine CSEM, and analyzed the influence of IP parameters in the Cole-Cole model on the electromagnetic response. Xu and Sun [17] designed polarized medium models with different field source azimuths, IP parameters and terrain, implemented 2.5D marine CSEM forward modeling based on adaptive finite element method, and analyzed the influence law of Cole-Cole model parameters on electromagnetic response. Li et al. [18] realized finite volume forward modeling of marine CSEM in 3D frequency domain based on the Cole-Cole model and applied dual-frequency IP phase decoupling technology to marine CSEM data interpretation, which improved the sensitivity of the IP phase to polarized reservoir objects. Qiu et al. [19] used the integral equation method to conduct a 3D forward modeling of marine CSEM with IP effect, adopted the scattering and superposition methods to calculate the dyadic Green's function, studied the response rule of the Cole-Cole polarization model, and analyzed the influence law of various model parameters. At present, although good research results have been obtained, the Cole-Cole model in the above marine CSEM forward modeling is only a qualitative description, lacking the physical and geometric characteristics of relevant actual petrology, so it cannot directly explain how the structure and mineral composition of rocks or reservoirs affect the conductive properties of rocks. Therefore, it is of great significance to find a physical model that can relate the conductivity characteristics of the seafloor strata to its structure, composition and polarizability, and study the influence law of the model parameters on the marine CSEM field to improve the interpretation accuracy of later data.

The generalized effective-medium theory of induced polarization (GEMTIP) model is a unified mathematical-physical model based on effective-medium theory (EMT), IP theory and Born approximation principle for heterogeneity, multiphase structure and polarizability of rock or reservoir [20–22]. The model is derived strictly based on Maxwell's equation of multiphase composite conductive medium, including both surface and volume polarization effects, and is suitable for describing electrode polarization effects related to electron polarization and thin film polarization effects related to ion polarization [23–25]. IP parameters of the GEMTIP model (such as matrix conductivity, volume fraction, relaxation parameters, grain radius, etc.) have clear physical definitions and are closely related to the reservoir structure, mineral grain size, shape, polarization, porosity and other geometric-physical properties, which can better describe the IP response characteristics of the reservoir. This provides a quantitative analysis method for studying the conductivity characteristics of multiphase composite reservoirs [26, 27].

In this paper, the GEMTIP composite conductivity model is introduced to analyze the influence of composition, structure and geometric characteristics of submarine reservoir and secondary pyrite on the induction-polarization response of marine CSEM. First, based on Maxwell's equation and GEMTIP model, a 3D finite difference electromagnetic field governing equation in frequency domain is established. After completing the non-uniform mesh generation and the emission source layout, the linear equations are solved directly by using the difference operator matrix. The correctness and effectiveness of the algorithm are verified by the forward calculation of a typical 1D reservoir model. Finally, we build the reservoir and secondary pyrite models and perform numerical calculations to study the influence characteristics of GEMTIP model parameters on the marine CSEM field response, and to analyze the influence rules of geometry parameters such as the polarization layer thickness, buried depth, and size on the induction-polarization response. The above research can provide a theoretical basis for the subsequent exploration of submarine oil resources with IP effect.

II. FDFD METHOD BASED ON GEMTIP MODEL

A. Introduction of the GEMTIP composite conductivity model

The GEMTIP model is a multiphase medium electrical model proposed by Zhdanov in 2008 based on the classical effective-medium method and IP effect theory. This model can translate the physical and electrical characteristics of a medium containing inclusions into an analytical expression for effective conductivity [20]. According to the basic idea of the GEMTIP model, minerals in the isotropic multiphase composite medium can be regarded as spherical grains of varying sizes. When the homogeneous medium is filled with N types of spherical grains, the effective conductivity of the multiphase composite polarized medium under quasi-static conditions can be expressed as:

$$\sigma_e = \sigma_0 \left\{ 1 + 3 \sum_{l=1}^{N} \left[f_l \frac{\sigma_l - \sigma_0}{2\sigma_0 + \sigma_l + 2k_l a_l^{-1} \sigma_0 \sigma_l} \right] \right\}, \quad (1)$$

where σ_0 is the matrix conductivity, f_l is the volume fraction of the lth grain, σ_l is the conductivity of the lth grain, and a_l is the radius of the lth grain. k_l is the surface polarizability factor, which is the complex function of the frequency, expressed as:

$$k_l = \alpha_l (i\omega)^{-C_l}, \quad (2)$$

where ω is the angular frequency, α_l is the surface polarizability coefficient of the lth grain, and C_l is the relaxation parameter of the lth grain.

The surface polarizability factor is substituted into equation (1) and, after a series of algebraic operations, the general analytical expression of the effective conductivity of a typical heterogeneous polarized medium can be written as:

$$\sigma_e = \sigma_0 \left\{ 1 + \sum_{l=1}^{N} \left[f_l m_l \left[1 - \frac{1}{1+(i\omega\tau_l)^{C_l}} \right] \right] \right\}. \quad (3)$$

The material property tensor m_l and time parameter τ_l of the lth grain are equal to:

$$m_l = 3\frac{\sigma_l - \sigma_0}{2\sigma_0 + \sigma_l}, \tau_l = \left[\frac{a_l}{2\alpha_l} \cdot \left(\frac{2}{\sigma_l} + \frac{1}{\sigma_0} \right) \right]^{1/C_l}. \quad (4)$$

Taking the polarization effect generated by the reservoir itself as an example, this paper introduces in detail the GEMTIP conductivity relaxation model (Fig. 1), which consists of a three-phase medium of oil, sand cluster with saltwater layer and pyrite [28], in which sand cluster with saltwater layer and pyrite are "conductive grains". The volume filled with oil is a "matrix" with dielectric properties. In this model, the IP effect is mainly caused by the double electric layer formed on the boundary of sand cluster with saltwater layer, pyrite and oil matrix.

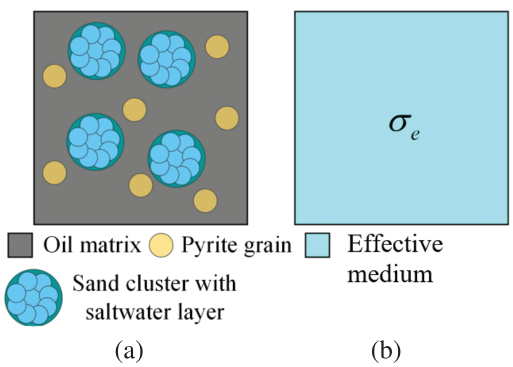

Fig. 1. Three-phase GEMTIP model: (a) subsea reservoir multiphase heterogeneous model and (b) corresponding effective-medium model.

B. Construction of governing equations containing GEMTIP model

Based on the introduced GEMTIP complex conductivity model, the electromagnetic field governing equation of frequency domain CSEM method is constructed. Assuming the time harmonic factor $e^{-i\omega t}$ and ignoring the displacement current, in the case of quasi-static, Maxwell's equations in the frequency domain containing the complex conductivity model can eliminate the magnetic field **H** in the formula after corresponding mathematical operations, and obtain the equation about the electric field **E**:

$$\nabla \times \nabla \times \mathbf{E} + i\omega\mu_0\sigma_e\mathbf{E} = -i\omega\mu_0\mathbf{J_s}, \quad (5)$$

where **E** is the electric field, $\mathbf{J_s}$ is the electric source-current density, ω is the angular frequency, μ_0 is the permeability in a vacuum and σ_e is the complex conductivity of the GEMTIP model. The above equation contains only one unknown electric field **E**, which can be solved directly. After the solution is completed, the electric field **E** can be substituted into the expression of Faraday's electromagnetic induction law to obtain the magnetic field **H**, thus reducing the overall calculation amount.

C. Grid generation and application of emission source

In order to overcome the influence of electromagnetic field source singularity on numerical results and make the electromagnetic field component approximate to zero when propagating to the Dirichlet boundary, we use a non-uniform grid to divide the submarine reservoir model [29]. We first use the seafloor surface as the interface and divide the grid of the model into two parts, where the upper grid consists of the seawater layer and the lower grid consists of the sediment layer. Then we place the transmitter and receiver on the seabed to simulate the process of electromagnetic excitation and response measurement. Finally, we use a fine grid to divide the central region of the emission source, and a variable step length coarse grid to divide other regions to obtain a large enough calculation area. The mesh size increases from the center to the outside, thereby improving the calculation efficiency and accuracy to a certain extent. The mesh division form of the three-dimensional finite-difference frequency-domain (FDFD) is shown in Fig. 2. The spatial positions of the electric and magnetic components are set on the grid, with the electric components located in the center of the edge of the hexahedron and the direction parallel to the tangent vector of the corresponding edge, and the magnetic components located in the center of the face of the hexahedron and the direction parallel to the normal vector of the corresponding plane [30]. Each electric field component is surrounded by four magnetic fields, each magnetic field component is surrounded by four electric fields, and the electromagnetic field component is staggered sampled and diffused to the surrounding area.

In terms of the selection of emission source, this author selects the electrical source commonly used in marine CSEM exploration as the emission source. The loading method of the electrical source is shown in Fig. 3. *Tx* is the emission source, whose loading position is the same as the spatial sampling position of the electric field component, and the direction of the emission current is the same as the direction of the electric field on the edge. *Rx* is a receiver, arranged along the axis of the electrical source, which can be used to record electromagnetic signals. J_{sx} is the x direction component of current density $\mathbf{J_s}$, and both J_{sy} and J_{sz} components are set to zero. During the loading process of the emission

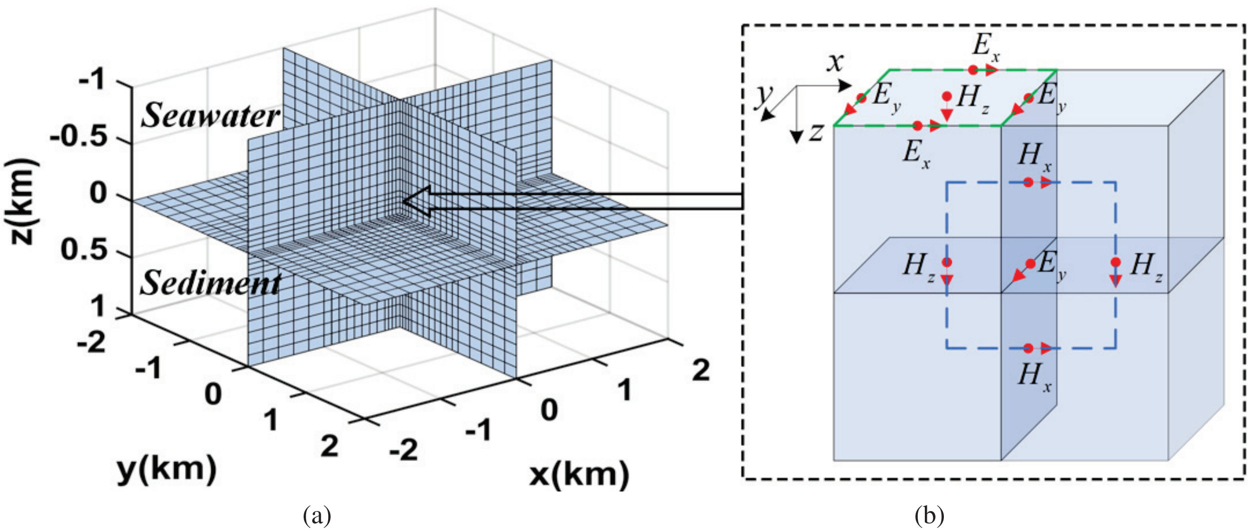

Fig. 2. Mesh settings of 3D FDFD: (a) non-uniform grid containing seawater and sediment layers and (b) spatial distribution of electromagnetic field components.

source, a current needs to be applied. Assuming the current intensity is 1 A, the current density $J_{sx} = 1/\Delta y \Delta z$, where Δy and Δz are the cell mesh sizes in the y and z directions.

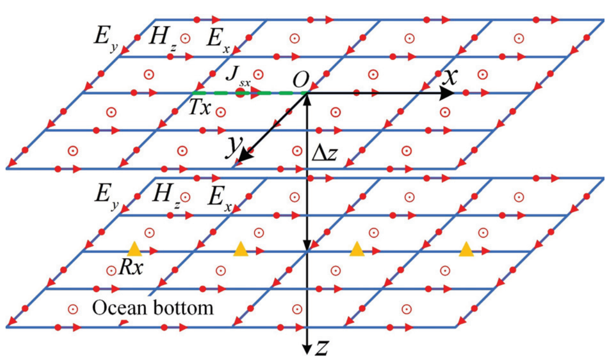

Fig. 3. Spatial position of the electrical source.

D. Solution of FDFD linear equations

According to the spatial distribution of electromagnetic field components and the results of emission source loading, this paper uses the first-order central difference method to discrete the frequency domain electromagnetic field component expression containing the GEMTIP model in the Cartesian coordinate system. In order to facilitate further derivation and calculation, the difference equations are converted into matrix form by using the difference operator matrix, refer to equation (5), replace the magnetic field component in the expression, and get an equation containing only electric field component [31]:

$$\begin{aligned}\boldsymbol{J}_{sx} = -\left[\frac{\delta_{hzdy}\delta_{exdy}}{(-i\omega\mu_0)} + \frac{\delta_{hydz}\delta_{exdz}}{(-i\omega\mu_0)} + \sigma_e\right]\boldsymbol{E}_x + \\ \left[\frac{\delta_{hzdy}\delta_{eydx}}{(-i\omega\mu_0)}\right]\boldsymbol{E}_y + \left[\frac{\delta_{hydz}\delta_{ezdx}}{(-i\omega\mu_0)}\right]\boldsymbol{E}_z\end{aligned}, \tag{6}$$

$$\begin{aligned}\boldsymbol{J}_{sy} = \left[\frac{\delta_{hzdx}\delta_{exdy}}{(-i\omega\mu_0)}\right]\boldsymbol{E}_x - \left[\frac{\delta_{hxdz}\delta_{eydz}}{(-i\omega\mu_0)} + \frac{\delta_{hzdx}\delta_{eydx}}{(-i\omega\mu_0)} + \sigma_e\right] \\ \boldsymbol{E}_y + \left[\frac{\delta_{hxdz}\delta_{ezdy}}{(-i\omega\mu_0)}\right]\boldsymbol{E}_z\end{aligned}, \tag{7}$$

$$\begin{aligned}\boldsymbol{J}_{sz} = \left[\frac{\delta_{hydx}\delta_{exdz}}{(-i\omega\mu_0)}\right]\boldsymbol{E}_x + \left[\frac{\delta_{hxdy}\delta_{eydz}}{(-i\omega\mu_0)}\right]\boldsymbol{E}_y - \\ \left[\frac{\delta_{hydx}\delta_{ezdx}}{(-i\omega\mu_0)} + \frac{\delta_{hxdy}\delta_{ezdy}}{(-i\omega\mu_0)} + \sigma_e\right]\boldsymbol{E}_z\end{aligned}, \tag{8}$$

where E_x, E_y, E_z, H_x, H_y and H_z are the column vectors of the electric field and the magnetic field respectively, δ_{ezdy}, δ_{eydz}, δ_{exdz}, δ_{ezdx}, δ_{eydx} and δ_{exdy} are the electric field difference operator matrices, representing the difference coefficients of the electric field in the x, y, z directions, and δ_{hzdy}, δ_{hydz}, δ_{hxdz}, δ_{hzdx}, δ_{hydx} and δ_{hxdy} are the magnetic field difference operator matrices, representing the difference coefficients of the magnetic field in the x, y, z directions, respectively. The difference operator matrix is a large sparse matrix, which differentiates adjacent electromagnetic field components by non-zero elements 1 and -1. σ_e is a diagonal matrix, and the diagonal element represents the medium conductivity of each edge, which is equal to the volume average of the medium conductivity of the four adjacent grids.

In order to directly solve the linear equations containing the GEMTIP model, the above governing equations are transformed into the form $\boldsymbol{MX} = \boldsymbol{N}$, and the matrix of each component can be written as:

$$\boldsymbol{M}=\begin{pmatrix} \boldsymbol{M}_{11} & \frac{\delta_{hzdy}\delta_{eydx}}{(-i\omega\mu_0)} & \frac{\delta_{hydz}\delta_{ezdx}}{(-i\omega\mu_0)} \\ \frac{\delta_{hzdx}\delta_{exdy}}{(-i\omega\mu_0)} & \boldsymbol{M}_{22} & \frac{\delta_{hxdz}\delta_{ezdy}}{(-i\omega\mu_0)} \\ \frac{\delta_{hydx}\delta_{exdz}}{(-i\omega\mu_0)} & \frac{\delta_{hxdy}\delta_{eydz}}{(-i\omega\mu_0)} & \boldsymbol{M}_{33} \end{pmatrix},$$

$$\boldsymbol{X}=\begin{pmatrix} \boldsymbol{E}_x \\ \boldsymbol{E}_y \\ \boldsymbol{E}_z \end{pmatrix}, \boldsymbol{N}=\begin{pmatrix} \boldsymbol{J}_{sx} \\ \boldsymbol{J}_{sy} \\ \boldsymbol{J}_{sz} \end{pmatrix}, \tag{9}$$

where $\boldsymbol{M}_{11}$, $\boldsymbol{M}_{22}$, and $\boldsymbol{M}_{33}$ are, respectively:

$$\boldsymbol{M}_{11}=-\frac{\delta_{hzdy}\delta_{exdy}}{(-i\omega\mu_0)}-\frac{\delta_{hydz}\delta_{exdz}}{(-i\omega\mu_0)}-\sigma_0\left\{1+\sum_{l=1}^{N}\left[f_l m_l\left[1-\frac{1}{1+(i\omega\tau_l)^{C_l}}\right]\right]\right\}. \tag{10}$$

$$\boldsymbol{M}_{22}=-\frac{\delta_{hxdz}\delta_{eydz}}{(-i\omega\mu_0)}-\frac{\delta_{hzdx}\delta_{eydx}}{(-i\omega\mu_0)}-\sigma_0\left\{1+\sum_{l=1}^{N}\left[f_l m_l\left[1-\frac{1}{1+(i\omega\tau_l)^{C_l}}\right]\right]\right\}. \tag{11}$$

$$\boldsymbol{M}_{33}=-\frac{\delta_{hydx}\delta_{ezdx}}{(-i\omega\mu_0)}-\frac{\delta_{hxdy}\delta_{ezdy}}{(-i\omega\mu_0)}-\sigma_0\left\{1+\sum_{l=1}^{N}\left[f_l m_l\left[1-\frac{1}{1+(i\omega\tau_l)^{C_l}}\right]\right]\right\}. \tag{12}$$

Since most of the elements in the difference operator matrix are zero, in order to improve computing efficiency and reduce memory consumption, this paper stores the difference operator matrix of electric field and magnetic field as a large sparse matrix, and directly solves the matrix equation $\boldsymbol{MX} = \boldsymbol{N}$ based on the built-in solver of MATLAB to calculate the column vectors of the electric field E_x, E_y, E_z. Then, the calculated results are put into the magnetic field component expressions, and the magnetic field H_x, H_y, H_z can be obtained.

III. ALGORITHM CORRECTNESS VERIFICATION

In order to verify the correctness and effectiveness of the above 3D modeling method, the marine CSEM response in the frequency domain of a typical 1D reservoir model is calculated and compared with the semi-analytical solution. As shown in Fig. 4, the emission source is an electrical source, 50 meters away from the seabed surface, and is towed forward by the exploration vessel. The emission current is 1 A, the emission frequency is 1 Hz. The receivers are arranged on the seabed and maintain the same z coordinates. Assume that the first layer is seawater layer, the thickness is 1 km, and the conductivity is 3.2 S/m. The second layer is the seabed sediment layer, the thickness is 1 km, the conductivity is 1 S/m. The third layer is the oil layer containing IP, the thickness is 0.2 km, the measured or empirical values of GEMTIP model parameters and inclusion grains are shown in Table 1 [32]. The conductivity of oil matrix is 0.005, and the parameters of sand cluster with saltwater layer and pyrite are indicated by subscripts 1 and 2, respectively. The size of the target area is 20 km×20 km×11 km and its coordinate range is (−10 km, 10 km) × (−10 km, 10 km) × (−1 km, 10 km). The size of the Dirichlet extension boundary is 40 km×40 km×22 km and its coordinate range is (−20 km, 20 km)×(−20 km, 20 km)×(−1 km, 21 km), which is also the entire numerical simulation area. The number of discrete grid cells is 76×76×39. The fine grid size of emission source and IP layer region is 100 m×100 m×50 m and 200 m×200 m×100 m, respectively. Other areas are divided by coarse grid. The grid terminates at the boundary where Dirichlet boundary conditions have been applied.

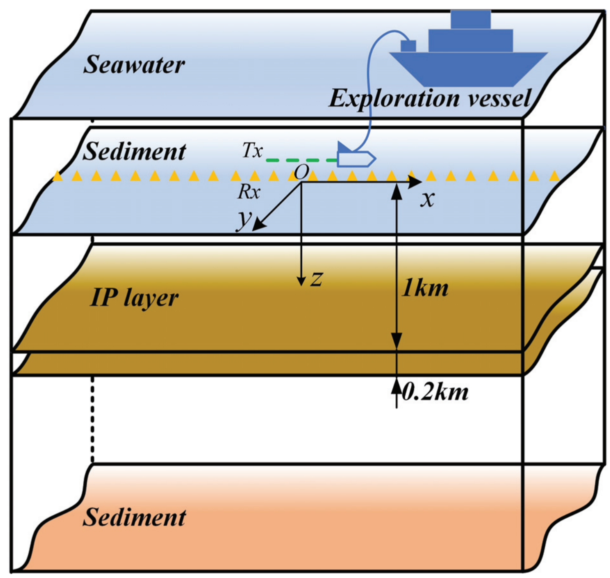

Fig. 4. Schematic diagram of 1D reservoir model.

Table 1: GEMTIP conductivity-relaxation model for subsea reservoirs

Variable of Sand Cluster	Unit	Value	Variable of Pyrite	Unit	Value
σ_1	S/m	1	σ_2	S/m	15
f_1	%	6	f_2	%	3
C_1	—	0.8	C_2	—	0.6
a_1	mm	0.5	a_2	mm	0.2
α_1	m^2 / (S·sec^{c_l})	0.5	α_2	m^2 / (S·sec^{c_l})	2

The 1D semi-analytical solution and the results of the forward modeling algorithm proposed in this paper are shown in Fig. 5. The solid blue line represents the 1D semi-analytical solution with IP, and the square represents the 3D numerical solution of the layered model with IP. The solid red line represents the 1D semi-analytical solution without IP, and the circle represents the 3D numerical solution of the layered model without IP. As can be seen from Fig. 5, the electromagnetic

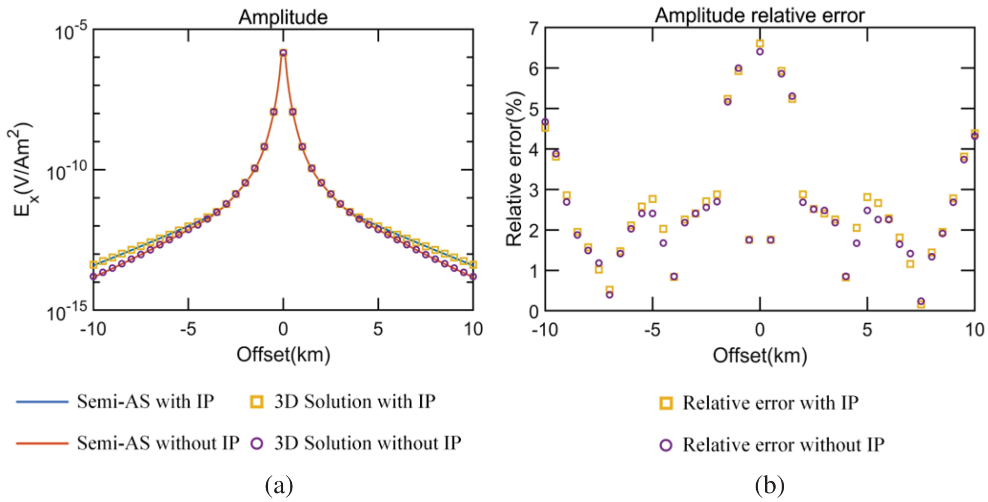

Fig. 5. Comparison of electromagnetic response and semi-analytical solution (semi-AS) of 1D reservoir model: (a) amplitude curve and (b) relative error curve.

response curves of the 3D simulation solution of the reservoir model with or without IP are basically consistent with those of the semi-analytical solution. The electromagnetic response E_x (unit: V/Am^2) in Fig. 5 is the normalized value of the electromagnetic signal acquired by the receiver to the electric dipole moment of the emission source, where the electric dipole moment is determined by the product of the emission current and the antenna length, i.e., V/m divided by Am [33]. The offset in Fig. 5 is the relative horizontal distance between the emission source *Tx* and the receiver *Rx*, which is measured in km. When the offset is between 2 km and 9 km, the amplitude relative error is less than 2.9% and 2.8%, respectively, indicating that the frequency-domain finite-difference algorithm based on the GEMTIP model has relatively high precision.

IV. ANALYSIS OF INDUCTION-POLARIZATION RESPONSE CHARACTERISTICS

A. 3D reservoir model

According to the research and discussion of reservoir IP mechanism in recent years, the IP effect will occur both in the reservoir itself and in the formation above it. In order to simulate the above rock and ore geological conditions, we first establish a 3D reservoir model. The settings of the transmitter and receiver are consistent with those in Fig. 4, the vacuum permeability μ_0 is $4\pi\times10^{-7}$ H/m, and the conductivity of the seabed sediments is 1 S/m. The location of the IP abnormal body is shown in Fig. 6, and its vertical distance from the z axis is 1 km. Tables 2 and 3 list IP parameters and geometry parameters of the reservoir model respectively. The variables t, d and s in Table 3 are the thickness, buried depth and geometrical size of the IP body. The size of the target area and the Dirichlet extension boundary are consistent with those in 1D reservoir model. The number of discrete grid cells is 68×68×49. The fine grid size of emission source and IP body region is also 100 m×100 m×50 m and 200 m×200 m×100 m, respectively. Other areas are divided by a coarse grid. Then, 3D numerical simulation of the reservoir models with different IP parameters and geometry parameters is carried out to analyze the marine CSEM induction-polarization response characteristics.

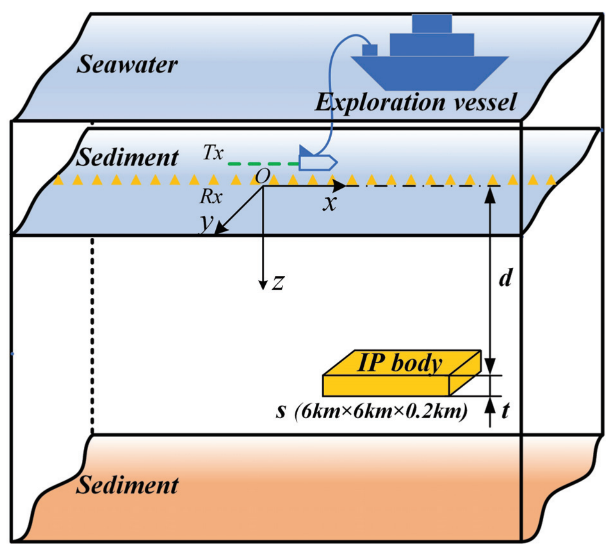

Fig. 6. 3D reservoir model.

In order to analyze the influence characteristics of IP parameters of reservoir model on the marine CSEM induction-polarization response, we set the matrix conductivity σ_0 as 0.001, 0.002, 0.005, and 0.01, the vol-

Table 2: IP parameters of 3D reservoir model

Variable	Unit	GEMTIP Model a	GEMTIP Model b	GEMTIP Model c	GEMTIP Model d
σ_0	S/m	0.001;0.002;0.005;0.01	0.005	0.005	0.005
σ_1	S/m	1	1	1	1
σ_2	S/m	15	15	15	15
f_1	%	5	2;5;7;9	5	5
f_2	%	3	3	3	3
C_1	—	0.8	0.8	0.2;0.5;0.8;1	0.8
C_2	—	0.6	0.6	0.6	0.6
a_1	mm	2	2	2	0.5;1;2;5
a_2	mm	0.2	0.2	0.2	0.2
α_1	m^2 / (S·sec^{c_l})	0.5	0.5	0.5	0.5
α_2	m^2 / (S·sec^{c_l})	2	2	2	2

Table 3: Geometry parameters of 3D reservoir model

Variable	Unit	Model 1	Model 2	Model 3
t	m	100;200;300;400	200	200
d	m	1000	1000;1100;1200;1300	1000
s	—	6 km×6 km×0.2 km	6 km×6 km×0.2 km	4 km×4 km×0.2 km; 5 km×5 km×0.2 km; 6 km×6 km ×0.2 km; 7 km×7 km×0.2 km

ume fraction f_1 as 0.02, 0.05, 0.07, and 0.09, the relaxation parameters C_1 as 0.2, 0.5, 0.8, and 1, and the grain radius a_1 as 0.5, 1, 2, and 5, respectively, according to the four models in Table 2, while keeping other parameters unchanged.

Figure 7 shows the marine CSEM induction-polarization response curves under different matrix conductivity, volume fraction, relaxation parameter and grain radius. It can be seen from Fig. 7 (a) that, with the increase of matrix conductivity σ_0, the variation amplitude of induction-polarization response gradually increases. As can be seen from Fig. 7 (b), when other parameters remain unchanged, the variation amplitude of induction-polarization response first increases and then decreases as the volume fraction f_1 increases. It can be seen from Fig. 7 (c) that the larger the relaxation parameter C_1 is, the variation amplitude of the induction-polarization response firstly increases and then decreases until it gradually becomes stable. As can be seen from Fig. 7 (d), when other parameters are unchanged, with the increase of grain radius a_1, the variation amplitude of induction-polarization response increases first and then decreases. As can be seen from Fig. 7, matrix conductivity has the greatest influence on the induction-polarization response results, followed by the volume fraction. Relaxation parameters and grain radius have relatively little influence.

In order to analyze the influence law of geometry parameters of reservoir model on the marine CSEM induction-polarization response, the thickness t is set as 100, 200, 300, and 400, the buried depth d is set as 1000, 1100, 1200, and 1300, the size s is set as 4 km×4 km×0.2 km, 5 km×5 km×0.2 km, 6 km×6 km×0.2 km and 7 km×7 km×0.2 km, and then forward modeling is carried out. The specific parameters are shown in Table 3. In the IP parameters, the matrix conductivity σ_0 is 0.005, the volume fraction f_1 is 0.05, the relaxation parameter C_1 is 0.8, the grain radius a_1 is 2, and the other parameters remain unchanged.

Figure 8 shows the marine CSEM induction-polarization response curves under different polarized layer thickness, buried depth and size. As can be seen from Fig. 8 (a), with the increase of the thickness t of the polarized layer, the amplitude of the induction-polarization response gradually increases, and the variation amplitude increases first and then becomes stable. As can be seen from Fig. 8 (b), when IP parameters, thickness and size of the polarized layer remain unchanged, the amplitude of the induction-polarization response gradually decreases with the increase of the buried depth d of the polarized layer. The variation amplitude first increases and then decreases. As can be seen from Fig. 8 (c), when IP parameters, thickness and buried depth of the polarized layer remain

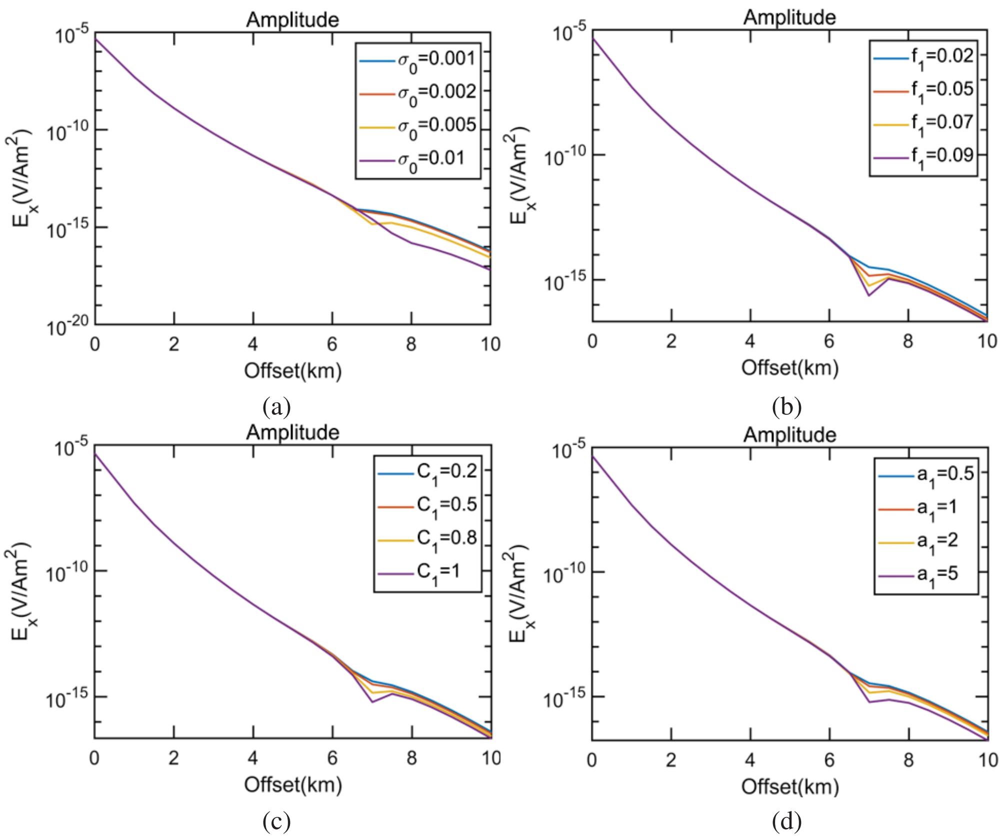

Fig. 7. Induction-polarization response curves of different IP parameters under reservoir polarization mode: (a) response curves of different matrix conductivity, (b) response curves of different volume fraction, (c) response curves of different relaxation parameter and (d) response curves of different grain radius.

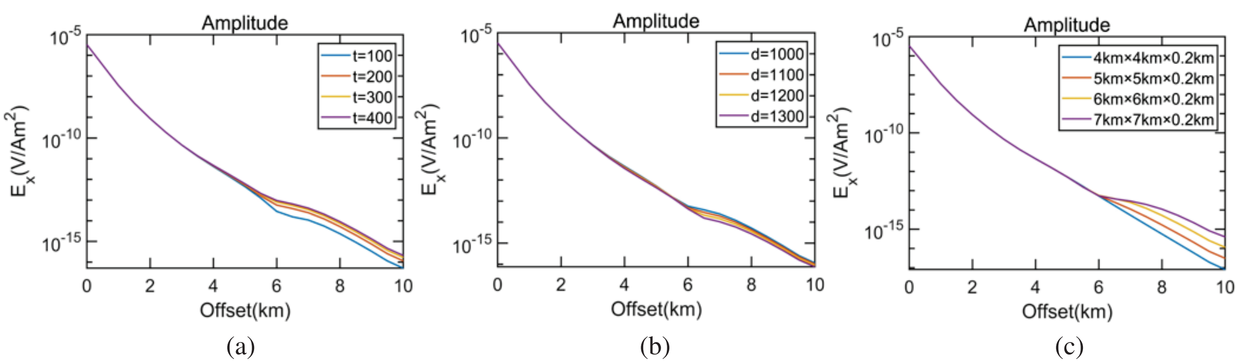

Fig. 8. Induction-polarization response curves of different geometry parameters under reservoir polarization mode: (a) response curves of different polarized layer thickness, (b) response curves of different polarized layer buried depth and (c) response curves of different polarized layer size.

unchanged, the amplitude of the induction-polarization response gradually increases with the increase of the size *s* of the polarized layer. The variation amplitude gradually increases until it becomes stable. It can be seen from Fig. 8 that the size of the polarized layer has the greatest influence on the marine CSEM induction-polarization response, followed by the thickness of the polarized layer. The influence of the buried depth of the polarized layer is relatively weak.

B. 3D secondary pyrite model

According to the above analysis, this section will design a 3D secondary pyrite model, which is composed of three-phase medium: matrix sedimentary rock, carbonates with saltwater layer and pyrite [34, 35], in which carbonates with saltwater layer and pyrite are "conductive grains" and sedimentary rocks are "matrix bodies". The settings of the transmitter and receiver are consistent with those in Fig. 6. Vacuum permeability μ_0 and submarine sediment conductivity are the same as above. The conductivity of the reservoir is 0.01 S/m and the size is 6 km×6 km×0.2 km. The IP abnormal body position in the pyrite polarization mode is shown in Fig. 9, and its vertical distance from the z axis is 1 km. Tables 4 and 5 list IP parameters and geometry parameters of the secondary pyrite model, respectively. The conductivity σ_0 of the matrix sedimentary rocks is 0.005, and the parameters of carbonates with saltwater layer and pyrite are indicated by subscript 1 and 2, respectively. The size of the target area, the Dirichlet extension boundary, the number of discrete grids, the fine grid size of emission source and IP layer region are consistent with those in 3D reservoir model. Subsequently, we carry out 3D forward modeling of polarization models with different IP parameters and geometry parameters, then analyze the influence law of the above parameters on the marine CSEM induction-polarization response.

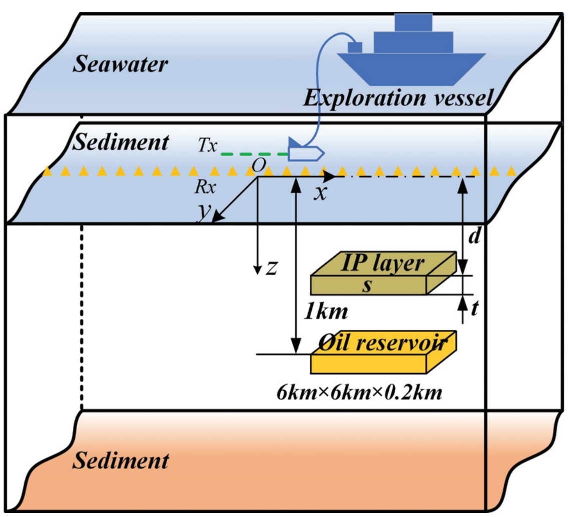

Fig. 9. 3D secondary pyrite model.

In order to analyze the influence characteristics and rules of IP parameters of secondary pyrite model on the marine CSEM induction-polarization response, we set the matrix conductivity σ_0 as 0.001, 0.002, 0.005, and 0.01. The volume fraction f_2 as 0.04, 0.08, 0.12, and 0.16, the relaxation parameter C_2 as 0.2, 0.5, 0.7, and 1, and the grain radius a_2 as 0.2, 0.5, 1, and 2, according to the four models in Table 4, while the other parameters are kept unchanged.

Figure 10 shows the marine CSEM induction-polarization response curves under different matrix conductivity, volume fraction, relaxation parameter and grain radius. As can be seen from Fig. 10 (a), with the increase of the matrix conductivity σ_0, the amplitude of the induction-polarization response gradually decreases, and the variation amplitude gradually increases until it becomes stable. As can be seen from Fig. 10 (b), when other parameters remain unchanged, the variation amplitude of induction-polarization response first increases and then decreases as the volume fraction f_2 increases. It can be seen from Fig. 10 (c) that the larger the relaxation parameter C_2 is, the variation amplitude of the induction-polarization response shows a trend of first increasing and then decreasing until it gradually becomes stable. As can be seen from Fig. 10 (d), when other parameters remain unchanged, with the increase of grain radius a_2, the variation amplitude of induction-polarization response also first increases and then decreases. As can be seen from Fig. 10, matrix conductivity has the greatest influence on the induction-polarization response results, followed by the volume fraction. Relaxation parameter and grain radius have relatively little influence.

In order to analyze the influence of geometry parameters on the marine CSEM induction-polarization response, the thickness t of the polarized layer is set as 100, 200, 300, and 400, the buried depth d is set as 100, 200, 300, and 400. The size s is set as 4 km×4 km×0.2 km, 5 km×5 km×0.2 km, 6 km×6 km×0.2 km, 7 km×7 km×0.2 km, and then forward modeling is carried out. The specific parameters are shown in Table 5. In the IP parameter, the matrix conductivity σ_0 is 0.005, the volume fraction f_2 is 0.08, the relaxation parameter C_2 is 0.8, the grain radius a_2 is 2, and the other parameters remain unchanged.

Figure 11 shows the marine CSEM induction-polarization response curves under different polarized layer thickness, buried depth and size. It can be seen from Fig. 11 (a) that, with the increase of the thickness t of the polarized layer, the amplitude of the induction-polarization response gradually increases and the variation amplitude first gradually increases and then becomes stable. As can be seen from Fig. 11 (b), when IP parameters, thickness and size of the polarized layer remain unchanged, the amplitude of the induction-polarization response gradually increases with the increase of the buried depth d of the polarized layer, and the variation amplitude first decreases and then increases. As can be seen from Fig. 11 (c), when IP parameters, polarized layer thickness and buried depth remain unchanged, the larger the polarized layer size s is, the amplitude of induction-polarization response gradually increases, and the variation amplitude gradually increases until it becomes stable. It can be seen from Fig. 11 that the size of the

Table 4: IP parameters of the 3D secondary pyrite model

Variable	**Unit**	**GEMTIP Model e**	**GEMTIP Model f**	**GEMTIP Model g**	**GEMTIP Model h**
σ_0	S/m	0.001;0.002;0.005;0.01	0.005	0.005	0.005
σ_1	S/m	0.5	0.5	0.5	0.5
σ_2	S/m	15	15	15	15
f_1	%	5	5	5	5
f_2	%	8	4;8;12;16	8	8
C_1	—	0.6	0.6	0.6	0.6
C_2	—	0.8	0.8	0.2;0.5;0.7;1	0.8
a_1	mm	0.2	0.2	0.2	0.2
a_2	mm	2	2	2	0.2;0.5;1;2
α_1	m^2 / (S·sec^{c_l})	0.4	0.4	0.4	0.4
α_2	m^2 / (S·sec^{c_l})	2	2	2	2

Table 5: Geometry parameters of the 3D secondary pyrite model

Variable	**Unit**	**Model 4**	**Model 5**	**Model 6**
t	m	100;200;300;400	200	200
d	m	300	100;200;300;400	300
s	—	6 km×6 km×0.2 km	6 km×6 km×0.2 km	4 km×4 km×0.2 km; 5 km ×5 km×0.2 km; 6 km×6 km ×0.2 km; 7 km×7 km×0.2 km

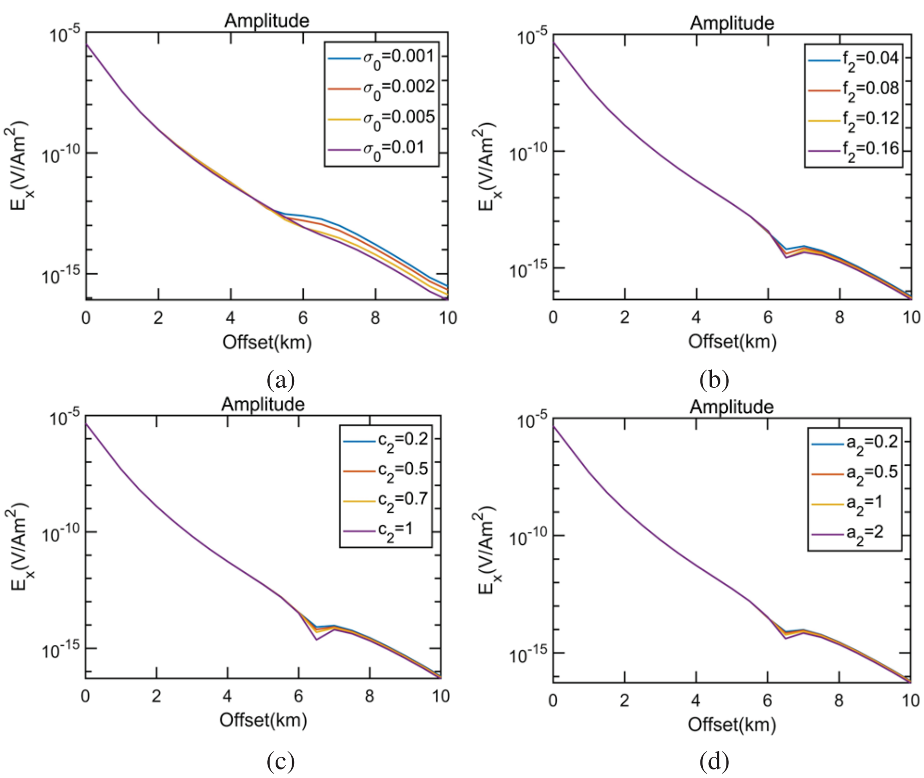

Fig. 10. Induction-polarization response curves of different IP parameters under pyrite polarization mode: (a) response curves of different matrix conductivity, (b) response curves of different volume fraction, (c) response curves of different relaxation parameter and (d) response curves of different grain radius.

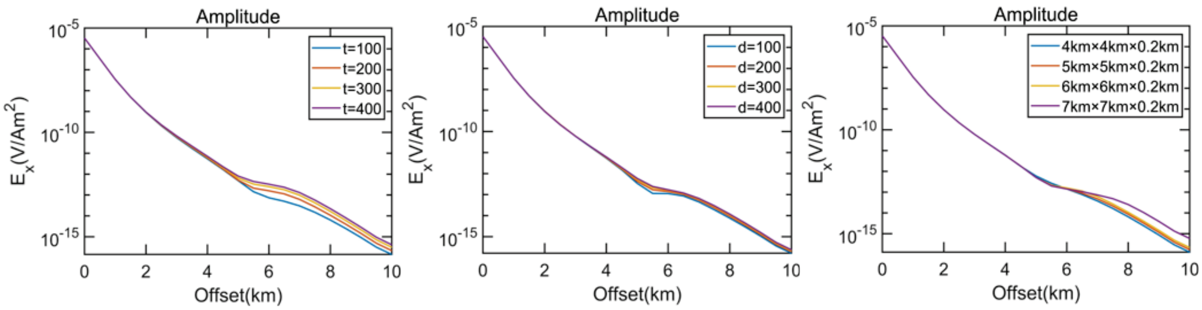

(a) (b) (c)

Fig. 11. Induction-polarization response curves of different geometry parameters under pyrite polarization mode: (a) response curves of different polarized layer thickness, (b) response curves of different polarized layer buried depth and (c) response curves of different polarized layer size.

polarized layer has the greatest influence on the marine CSEM induction-polarization response results, followed by the thickness of the polarized layer. The influence of the buried depth of the polarized layer is relatively small.

V. CONCLUSION

In order to analyze the influence of physical properties and geometric characteristics of submarine reservoir and secondary pyrite on marine CSEM field, this paper introduces the GEMTIP model, adopts the FDFD method to calculate the induction-polarization response of reservoir and secondary pyrite model, and studies the influence characteristics of IP parameters and geometric parameters on the induction-polarization response under different polarization modes. Results show that the matrix conductivity of IP parameters in the reservoir self-polarization mode has the greatest influence on the induction-polarization response results, the volume fraction has the second influence, and the relaxation parameter and grain radius have relatively little influence. In addition, compared with the polarized layer thickness and buried depth, the polarized layer size of geometry parameters has more obvious influence on the induction-polarization response results. The effect of IP parameters and geometry parameters in the secondary pyrite polarization mode on the induction-polarization response is similar to that of the reservoir self-polarization mode. Therefore, the numerical calculation method of marine CSEM IP effect based on GEMTIP model proposed in this paper can provide a new tool for quantitative analysis of the influence of rock and ore structure, composition and fluid content on its conductive characteristics. The research is of great significance and value for understanding the relationship between submarine multiphase composite medium and electromagnetic wave propagation.

ACKNOWLEDGMENT

The authors would like to thank the reviewers and the editors for their valuable comments. This research was financially supported by the National Key Research and Development Program of China (Grant Number 2022YFC2807904).

REFERENCES

[1] K. A. Weitemeyer, S. Constable, and A. M. Tréhu, "A marine electromagnetic survey to detect gas hydrate at Hydrate Ridge, Oregon," *Geophys. J. Int.*, vol. 187, no. 1, pp. 45-62, June 2011.

[2] S. Constable, "Ten years of marine CSEM for hydrocarbon exploration," *Geophysics*, vol. 75, no. 5, pp. 75A67-75A81, Oct. 2010.

[3] S. Constable, "Review paper: Instrumentation for marine magnetotelluric and controlled source electromagnetic sounding," *Geophys. Prospect.*, vol. 61, pp. 505-532, Jan. 2013.

[4] S. Hölz, A. Swidinsky, M. Sommer, M. Jegen, and J. Bialas, "The use of rotational invariants for the interpretation of marine CSEM data with a case study from the North Alex mud volcano, West Nile Delta," *Geophys. J. Int.*, vol. 201, no. 1, pp. 224-245, Jan. 2015.

[5] H. B. Chen, T. L. Li, H. Y. Shi, H. Wang, and S. P. Li, "An edge-based finite element method for 3D marine controlled-source electromagnetic forward modeling with a new type of second-order tetrahedral edge element," *Int. J. Appl. Electrom.*, vol. 57, no. 3, pp. 217-233, May 2018.

[6] M. W. Dunham, S. Ansari, and C. G. Farquharson, "Application of 3D marine controlled-source electromagnetic finite-element forward modeling to hydrocarbon exploration in the Flemish Pass Basin offshore Newfoundland, Canada," *Geophysics*, vol. 83, no. 2, pp. WB33-WB49, Apr. 2018.

[7] J. H. Wang, B. Li, L. P. Chen, and Z. H. Wang, "Theoretical analysis and experimental measurements of electromagnetic radiation from a horizontal electric dipole in shallow sea," *Electromagnetics*, vol. 37, no. 6, pp. 398-410, Apr. 2017.

[8] L. Slater and D. Glaser, "Controls on induced polarization in sandy unconsolidated sediments and application to aquifer characterization," *Geophysics*, vol. 68, no. 5, pp. 1547-1558, Oct. 2003.

[9] C. Ulrich and L. Slater, "Induced polarization measurements on unsaturated, unconsolidated sands," *Geophysics*, vol. 69, no. 3, pp. 762-771, June 2004.

[10] Z. X. He and X. B. Wang, "Oil/gas detection by electromagnetic survey," *Oil Geophys. Prospect.*, vol. 42, no. 1, pp. 102-106, Feb. 2007.

[11] P. C. Veeken, P. J. Legeydo, Y. A. Davidenko, E. O. Kudryavceva, S. A. Vanov, and A. Chuvaev, "Benefits of the induced polarization geoelectric method to hydrocarbon exploration," *Geophysics*, vol. 74, no. 2, pp. B47-B59, Apr. 2009.

[12] D. Z. Wang, S. S. Yan, Z. J. Dong, X. D. Tan, Z. Li, and Y. H. Liu, "IP effect on marine CSEM based on two polarization modes of oil/gas reservoir," *Prog. Geophys. (in Chinese)*, vol. 30, no. 3, pp. 1304-1314, 2015.

[13] Y. W. Huang, "3D forward modeling and response analysis of the controlled source electromagnetic signal with IP effect," M.S. thesis, School of Geophysics and Measurement-Control Technology, East China University of Technology, Nanchang, Jiangxi, China, June 2017.

[14] W. Q. Liu, P. R. Lin, Q. T. Lu, Y. Li, and J. H. Li, "Synthetic modelling and analysis of CSEM full-field apparent resistivity response combining EM induction and IP effect for 1D medium," *Explor. Geophys.*, vol. 49, no. 5, pp. 609-621, May 2017.

[15] X. Z. Ding, Y. G. Li, and Y. Liu, "Influence of IP effects on marine controlled-source electromagnetic responses," *Oil Geophys. Prospect.*, vol. 53, no. 6, pp. 1341-1350, Dec. 2018.

[16] R. Mittet, "Electromagnetic modeling of induced polarization with the fictitious wave-domain method," *SEG Technical Program Expanded Abstracts*, pp. 979-983, Aug. 2018.

[17] K. J. Xu and J. Sun, "Induced polarization in a 2.5D marine controlled source electromagnetic field based on the adaptive finite-element method," *Appl. Geophys.*, vol. 15, no. 2, pp. 332-341, June 2018.

[18] J. Li, Z. He, and N. Feng, "Induced polarization effects of 3D frequency domain MCSEM responses using finite volume method," *Int. J. Appl. Electrom.*, vol. 61, no. 4, pp. 491-507, May 2019.

[19] N. Qiu, Z. X. Luo, Q. C. Fu, Z. Sun, Y. J. Chang, and B. R. Du, "Identification of induced polarization of submarine hydrocarbons in marine controllable source electromagnetic exploration," *Front. Earth. Sc-Switz.*, vol. 10, pp. 1-24, Jan. 2023.

[20] M. S. Zhdanov, "Generalized effective-medium theory of induced polarization," *Geophysics*, vol. 73, no. 5, pp. 197-211, Oct. 2008.

[21] L. Fu, "Induced polarization effect in time domain: Theory, modeling, and applications," M.S. thesis, Department of Geology and Geophysics, The University of Utah, Salt Lake City, UT, USA, Dec. 2011.

[22] X. L. Tong, L. J. Yan, and K. Xiang, "Modifying the generalized effective-medium theory of induced polarization model in compacted rocks," *Geophysics*, vol. 85, no. 4, pp. 245-255, Aug. 2020.

[23] C. R. Phillips, "Experimental study of the induced polarization effect using Cole-Cole and GEMTIP models," M.S. thesis, Department of Geology and Geophysics, The University of Utah, Salt Lake City, UT, USA, Dec. 2010.

[24] M. S. Zhdanov, V. Burtman, and A. F. Marsala, "Carbonate reservoir rocks show induced polarization effects, based on generalized effective medium theory," in *Extended Abstracts of 75th EAGE Conference & Exhibition*, pp. 1-5, June 2013.

[25] Y. J. Chang, T. Tohniyaz, and H. Y. Wang, "Influence factors of frequency-dependent coefficient with GEMTIP model," *Oil Geophys. Prospect.*, vol. 53, no. 5, pp. 1103-1109, Oct. 2018.

[26] V. Burtman, H. Y. Fu, and M. S. Zhdanov, "Experimental study of induced polarization effect in unconventional reservoir rocks," *Geomaterials*, vol. 4, no. 4, pp. 117-128, Oct. 2014.

[27] M. S. Zhdanov, V. Burtman, M. Endo, and W. Lin, "Complex resistivity of mineral rocks in the context of the generalised effective-medium theory of the induced polarisation effect," *Geophys. Prospect.*, vol. 66, no. 4, pp. 798-817, May 2018.

[28] V. Burtman and M. S. Zhdanov, "Induced polarization effect in reservoir rocks and its modeling based on generalized effective-medium theory," *Resource-Efficient Tech.*, vol. 1, no. 1, pp. 34-48, July 2015.

[29] H. Klingbeil, K. Beilenhoff, and H. L. Hartnagel, "FDFD full-wave analysis and modeling of dielectric and metallic losses of CPW short circuits," *IEEE T. Microw. Theory*, vol. 44, no. 3, pp. 485-487, Mar. 1996.

[30] Y. Kane, "Numerical solution of initial boundary value problems involving maxwell's equations in

isotropic media," *IEEE Trans. Antennas Propag.*, vol. 14, no. 3, pp. 302-307, May 1966.

[31] Y. J. Ji, H. S. Liu, Y. B. Yu, and X. J. Zhao, "3-D modelling and analysis of superparamagnetic effects in ATEM based on the FDFD," *Geophys. J. Int.*, vol. 231, no. 2, pp. 1252-1267, June 2022.

[32] V. Burtman, A. V. Gribenko, and M. S. Zhdanov, "Advances in experimental research of induced polarization effect in reservoir rocks," *SEG Technical Program Expanded Abstracts*, pp. 2475-2479, Oct. 2010.

[33] S. Constable and L. J. Srnka, "An introduction to marine controlled-source electromagnetic methods for hydrocarbon exploration," *Geophysics*, vol. 72, no. 2, pp. WA3-WA12, Apr. 2007.

[34] S. Z. Zhang, Y. X. Li, J. P. Zhou, X. W. Nie, A. C. Zhou, and G. D. Yang, "Induced polarization (IP) method in oil exploration – the cause of IP anomaly and it's relation to the oil reservoir," *Chinese J. Geophys.*, vol. 29, no. 6, pp. 597-614, Nov. 1986.

[35] B. K. Sternberg, "A review of some experience with the induced polarization/resistivity method for hydrocarbon surveys: Successes and limitations," *Geophysics*, vol. 56, no. 10, pp. 1522-1532, Oct. 1991.

Chunying Gu (Graduate Student Member, IEEE) received the M.S. degree from the College of Mechanical and Vehicle Engineering, Hunan University, Changsha, China, in 2011. She is currently pursuing the Ph.D. degree in detection technology and automation from Jilin University, Changchun, China. Her research interests include 3D marine controlled-source electromagnetic (CSEM) modeling and data processing.

Suyi Li (Member, IEEE) received her M.Sc. and Ph.D. degrees both from Jilin University in 2002 and 2009, respectively. From 2008 to 2009, she studied at the University of Illinois at Urbana-Champaign as a joint Ph.D. Now she is a professor in Jilin University. Her main research interests include computer applications and digital signal processing.

Silun Peng received the Ph.D. degree from the College of Automotive Engineering, Jilin University, Changchun, China, in 2014. He is currently a deputy senior engineer with Jilin University. His research interests include, but are not limited to, computer applications, digital signal processing and hardware system design.

Research on Electromagnetic Interference of Liquid Crystal Display Screen on Low-medium Speed Maglev Trains

Yutao Tang, Xin Li, and Chao Zhou

Institute of Electronic and Electrical Engineering
Civil Aviation Flight University of China, Guanghan 618307, China
835578907@qq.com, lixin@cafuc.edu.cn, zc_cafuc@163.com

***Abstract* –** Low-medium speed maglev trains might suffer from electromagnetic interference (EMI) during operation, which is specifically manifested as a blurred image on the liquid crystal display (LCD) screens of the passenger information system (PIS). In order to study the characteristics of the EMI, firstly, the working principle of PIS is analyzed in response to the fault phenomenon of the LCD screens. Possible interference sources are studied. Research results indicate that the leakage magnetic field generated by the transverse end effect of linear motors is the main interference source causing LCD screen faults. Secondly, the coupling mechanism of the EMI is analyzed. Results show that the transverse end effect can cause an increase in the ground potential of the LCD screen casing, resulting in a blurred image on the LCD screen. Finally, the EMI suppression method by suspending and grounding the LCD screen is proposed and its feasibility is verified. In this paper, we comprehensively study the EMI of LCD screens, which provides a theoretical basis for solving the tangible faults of maglev trains.

***Index Terms* –** Coupling mechanism, electromagnetic interference, interference suppression, transverse end effect.

I. INTRODUCTION

The layout of electrical and electronic equipment in low-medium speed maglev trains (speeds of 80 km/h to 100 km/h) are complex. Moreover, the electromagnetic coupling relationship between cables, equipment, and vehicle body is also complicated [1]. Therefore, maglev trains are highly likely to generate electromagnetic interference (EMI) problems, which impact the electronic equipment of trains, such as the liquid crystal display (LCD) screen of the passenger information system (PIS) [2]. Thus, it is important to study the EMI of low-medium speed maglev trains.

Existing research is not comprehensive. Some researchers have conducted research on the electromagnetic environment of urban rail transit [3–5]. Electromagnetic noise around the maglev train was tested and the frequency range of the noise and its impact on the communication system of nearby high-speed trains was determined in [6–8]. EMI source and related models of low-medium speed maglev trains was studied in [9–13]. In response to the interference problem of LCD screens of the PIS, Wen Zheng and others briefly described the excitation sources of electromagnetic radiation (EMR) generated by the LCD screen and analyzed the interference coupling mechanism and fault reasons of it [14, 15]. Chen and Zhou proposed a method for estimating electromagnetic compatibility (EMC) products by analyzing the current spectrum of LCD screen driver power supplies [16]. The EMI problem of LCD screens on subways was studied, and interference suppression schemes were proposed in [17, 18]. The above studies mostly focus on LCD screens on subways. There is limited research on EMI of equipment for low-medium speed maglev trains.

This paper focuses on a fault case of LCD screens in the PIS of low-medium speed maglev trains and studies the EMI of the LCD screen. Firstly, the driving principle of the LCD screen in PIS is analyzed based on the working principle of PIS. Secondly, the interference source and its coupling mechanism are researched, and it is found that the transverse end effect of the linear motor is the main interference source causing LCD screen faults. In addition, the induced voltage generated in the closed circuit between the LCD screen and the control system is simulated and calculated. Thirdly, a classification study is conducted on the suppression methods of the EMI. Finally, an EMI suppression scheme by using diodes in forward and reverse series connection for LCD screen suspension grounding is proposed and verified. The research results of this paper can provide a theoretical basis for solving EMI faults in LCD screens on low-medium speed maglev trains.

II. FAULT ANALYSIS OF LCD SCREENS

A. Working principle of LCD screens

The PIS on the low-medium speed maglev train is computer-based and utilizes a network platform to display real-time dynamic information to passengers through LCD screens. It includes information on

Submitted On: August 23, 2024
Accepted On: December 12, 2024
https://doi.org/10.13052/2024.ACES.J.391210

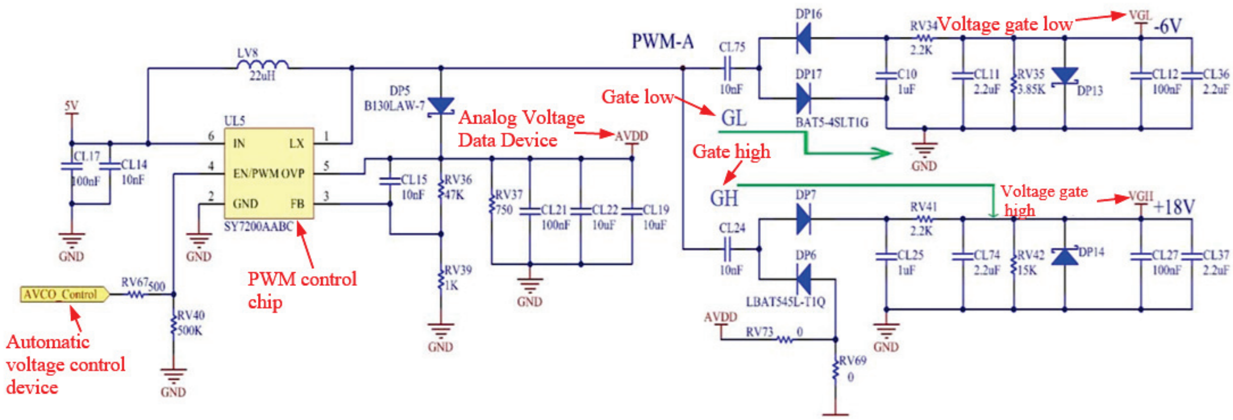

Fig. 1. Driving circuit of an LCD screen.

emergency situations and guiding passengers to evacuate. Therefore, the LCD screens must clearly display relevant information to ensure normal operation and safety.

The driving circuit of the LCD screen and the values of its resistance, inductance, and capacitance are shown in Fig. 1. The power supply ranges of each voltage in the drive circuit are shown in Table 1.

Firstly, the automatic voltage control device (AVCO) provides the corresponding working voltage to the PWM control chip to output a PWM square wave matrix. When point PWM-A is at a high level, the DP17 in the GL circuit is conductive and CL75 is charged by point A, causing the voltage on the left side of GL to rise to the value of the analog voltage data device (AVDD). When point A is at a low level, the voltage on the right side of GL becomes the negative value of AVDD. Secondly, DP16 is conductive, and the voltage is divided by RV34 and RV35, making the value of the voltage gate low (VGL) equal to -6 V. When the PWM pulse wave at point A is in its initial cycle, CL24 in the GH circuit is charged through DP6. Due to the fast-charging speed, the voltage difference between the left and right sides of GH during low pulse cycles is equal to the value of AVDD. When point A is at high voltage, due to the voltage difference on both sides of CL24 not being able to suddenly change, the voltage on the right side of GH becomes twice the voltage value of AVDD. At this point, DP7 is conducting and the voltage is distributed between RV41 and RV42, making the voltage gate low (VGH) equal to 18 V. The above principle is to achieve LCD screen imaging by controlling the voltage values on both sides of GH and GL.

Table 1: Power supply range of each voltage in the LCD screen drive circuit

Name	Circuit Voltage	VGH	VGL	AVDD
Power Range (V)	5	15∼22	-6∼10	8∼12

B. Overview of fault

During the operation of the low-medium speed maglev train, the LCD screen of the PIS may have unclear screen images, which are manifested as thin lines, flickers, or snowflakes in the displayed images. Figure 2 is a simplified model of a maglev train, where MC1 and MC2 are carriages with drivers.

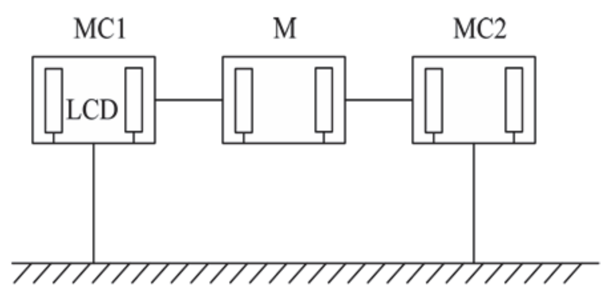

Fig. 2. Simplified model of a maglev train.

It can be seen that the train has a total of three carriages, each equipped with two LCD screens. The outer shells of the LCD screens are grounded through the vehicle body.

Based on the working principle of LCD screens and combined with the complex electromagnetic environment of the low-medium speed maglev train, we now study interference sources and their coupling methods.

III. ANALYSIS OF EMI COUPLING MECHANISM ON LCD SCREENS

A. Analysis of interference sources

EMI sources of low-medium speed maglev trains include collector shoes, linear motors, suspension electromagnets, train metal casings, and power and lighting systems [19]. The interference sources and their causes are shown in Table 2. The EMI generated by ① mainly affects the electromagnetic environment outside the train, and the EMR generated by ② and ⑤ is very weak. Therefore, those three sources have almost no impact on the LCD screen.

Table 2: Interference sources and their causes of EMI

	Source	Cause
①	Collector shoes	Spark discharge generated by friction and instantaneous poor contact
②	Train metal casings	EMR caused by reflection
③	Driving system	Strong magnetic field generated by linear motors
④	Suspension system	Strong magnetic field generated by suspended electromagnets
⑤	Power and lighting systems	EMR at the inlet and outlet of wires

The suspension system consists of three modules: coil, magnetic yoke, and track [20]. Its simulation model is shown in Fig. 3.

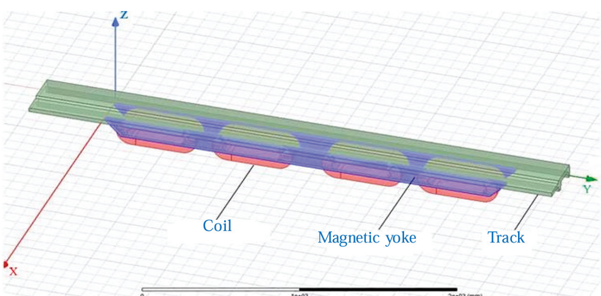

Fig. 3. Simulation model of the suspension system.

By simulating the suspension system, the magnetic induction intensity of the coil, track, and yoke can be obtained separately, as shown in Figs. 4, 5, and 6, respectively.

Figures 4, 5, and 6 show that the DC magnetic field of the suspension system is relatively large in the magnetic yoke and the middle of the track. In order to study the EMI of the suspension system, the relationship between the magnetic induction intensity of the above two positions and distance can be studied. The research results are shown in Fig. 7.

According to the simulation results, when the distance from the suspension electromagnet exceeds 400 mm, the magnetic induction intensity will be very weak.

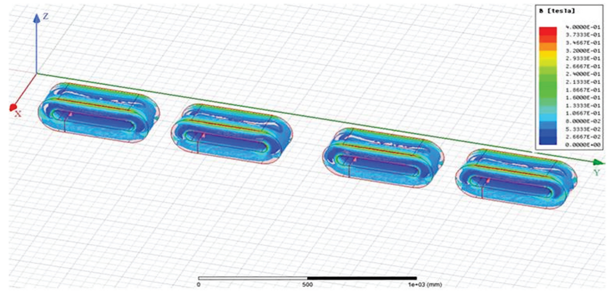

Fig. 4. Distribution of magnetic induction intensity of the coil.

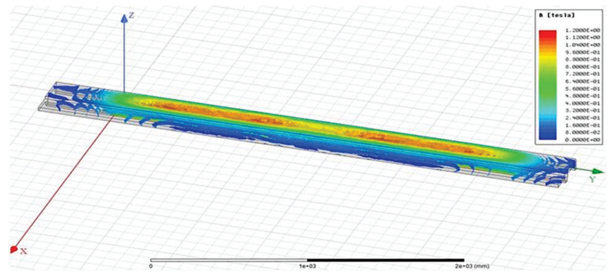

Fig. 5. Distribution of magnetic induction intensity of the track.

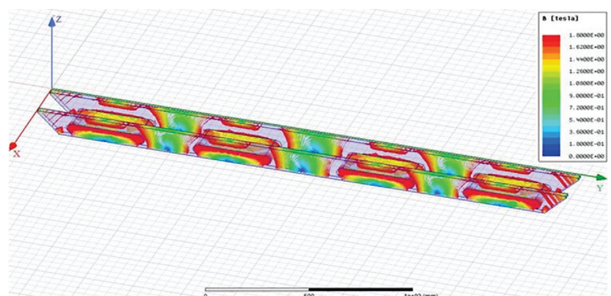

Fig. 6. Distribution of magnetic induction intensity of the magnetic yoke.

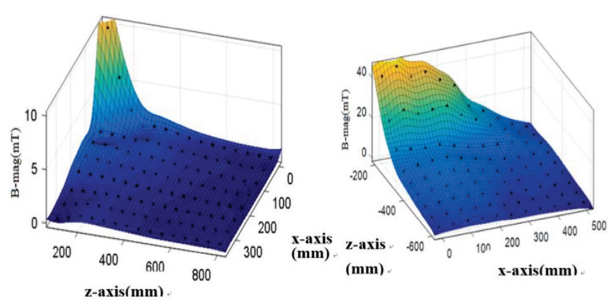

Fig. 7. Simulation diagram of magnetic induction intensity changing with distance.

Most electronic devices on maglev trains are more than 0.65 m away from the suspension electromagnet. Thus, the impact of EMI generated by ④ on the LCD screen can be ignored. Because the cables for the electronic equipment of the train are laid under the carriage, and the distance between the carriage bottom and the linear motor is very close (about 650 mm), this paper will focus on studying the impact of EMI generated by the driving system ③ on the LCD screens.

B. Magnetic field analysis of linear motors

In the ideal model of a linear motor, the primary of the motor is region 1 (Reg. 1), the air gap between the primary and secondary of the motor is region 2 (Reg. 2), the secondary of the motor is region 3 (Reg. 3), and the part below the secondary is region 4 (Reg. 4). In the following equations, the subscripts x, y, and z represent the x-direction, y-direction, and z-direction. The subscripts 1, 2, 3, and 4 represent Reg. 1, Reg. 2, Reg. 3, and Reg. 4, respectively.

Assuming there is no free charge, the vector magnetic potential $\boldsymbol{A}$ of the linear motor is [20]:

$$\nabla^2 \boldsymbol{A} = \mu\gamma\left[\frac{\partial \boldsymbol{A}}{\partial t} - v \times (\nabla \times \boldsymbol{A})\right], \tag{1}$$

where μ and γ are the magnetic permeability and electrical conductivity, respectively. $\boldsymbol{v}$ is the speed of magnetic field movement.

Assuming $\boldsymbol{A}$ is in the z-direction:

$$\boldsymbol{A}_z \boldsymbol{A}(y)\, e^{j(\omega t - \beta x)}, \tag{2}$$

where ω is the angular frequency and β is the phase constant.

Because $\partial^2 \boldsymbol{A}_z / \partial x^2 = -\beta^2 A_z$, equation (1) can be rewritten as:

$$\frac{\partial^2 \boldsymbol{A}_z}{\partial y^2} \boldsymbol{A}_z \beta^2 (1 + \frac{j\mu\gamma s v_s}{\beta}), \tag{3}$$

where v_s is velocity of the air gap magnetic field generated in the Reg. 1, and s is the slip ratio.

The boundary conditions are:

$$\begin{cases} y = 0,\ B_{y3} = B_{y2} \\ y = h,\ H_{x3} = H_{x4} \\ y = h,\ B_{x3} = B_{x4} \\ y \to \infty,\ \boldsymbol{A}_4 = 0 \end{cases}, \tag{4}$$

where h is the thickness of Reg. 3, and B and H are the magnetic induction intensity and magnetic field intensity, respectively.

Let us assume:

$$\alpha^2 = \beta^2 (1 + \frac{j\mu\gamma s v_s}{\beta}). \tag{5}$$

According to equations (3-5) and $\nabla \times \boldsymbol{A} = \boldsymbol{B}$, the magnetic induction intensity $\boldsymbol{B}_3$ of Reg. 3 can be solved:

$$\boldsymbol{B}_3 = \frac{\boldsymbol{B}_m \alpha}{j\beta\Delta}\left[\sinh\alpha(y-h) - \frac{\mu\beta}{\mu_0\alpha}\cosh\alpha(y-h)\right] e^{j(\omega t - \beta x)} \boldsymbol{k}_x + \frac{\boldsymbol{B}_m}{\Delta}\left[\cosh\alpha(y-h) - \frac{\mu\beta}{\mu_0\alpha}\sinh\alpha(y-h)\right] e^{j(\omega t - \beta x)} \boldsymbol{k}_y, \tag{6}$$

where $\boldsymbol{B}_m$ is the amplitude of the air gap magnetic field, and $\boldsymbol{k}_x$ and $\boldsymbol{k}_y$ is the unit vector of x-direction and y-direction. Then:

$$\Delta = \cosh\alpha h + \frac{\mu\beta}{\mu_0\alpha}\sin\alpha h. \tag{7}$$

Based on the above analysis, the magnetic field of each region of the linear motor can be obtained, and the distribution of its magnetic field will be simulated next.

There are five linear motors on both sides of each carriage of the maglev train The parameters of the linear motors are shown in Table 3.

Table 3: Parameters of the linear motor

Name	Data	Name	Data
Current	300 A	Excitation frequency	120 Hz
Core height	120 mm	Gap between the bottom of the train and the track	13 mm
Polar distance	225 mm	Winding form	Stacked
Number of conductors per slot	6	Thickness of steel reaction plate	4 mm
Thickness of aluminum reaction plate	20 mm	Core thickness	220 mm

Based on the dimensional data shown in Table 3, a model of the linear motor is established in ANSYS Maxwell 3D simulation software. Firstly, when selecting materials, the iron cores on the primary and secondary sides are made of silicon steel sheets (Model: DW465-50), and the material of the reaction plate is aluminum. Secondly, add three-phase current excitation (phase current: 300 A; excitation frequency: 120 Hz) to the primary winding of the linear motor. We then assign mesh operation (on selection: maximum element length 1.5 mm; inside selection: maximum element length 2 mm). Finally, the magnetic field strength and magnetic induction strength of the linear motors can be simulated and calculated as shown in Fig. 8.

As shown in Fig. 8, there is magnetic field leakage in the end winding of the linear motor. The magnetic field strength between the motor winding of the linear motor and the air gap is 5×10^4 A/m. The closer it is to the end, the stronger the magnetic field.

In order to further investigate the interference caused by the leakage magnetic field generated by the end winding of the linear motors, a metal conductor, having a length of 800 mm and a diameter of 4.5 mm, is set horizontally along the X-axis in the simulation model

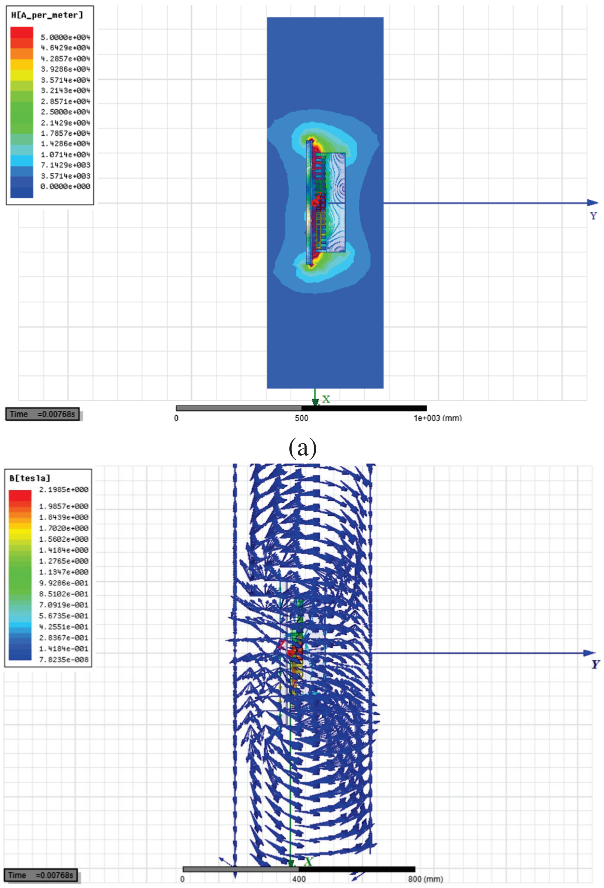

(a)

(b)

Fig. 8. Simulation results of a linear motor: (a) simulation results of magnetic field strength and (b) simulation results of magnetic induction intensity.

of a linear motor. The influence of the magnetic field of the linear motor on the equipment will be manifested through the inductive terminal voltage of the conductor. Changing the distance between the conductor and the linear motor can reflect the strength of the magnetic field of the linear motor at different positions. The simulation results are presented in Fig. 9.

As shown in Fig. 9, the closer the conductor is to the linear motor, the greater the induced voltage. When the distance changes along the Z-axis, the maximum induced voltage is 161.52 mV. When the distance changes along the Y-axis, the maximum induced voltage is 353.02 mV. Based on simulation outcomes, when the five linear motors operate simultaneously, taking the worst-case scenario into account, induced voltage at a distance of 650 mm from the linear motor is approximately 3.4 V, which will give rise to certain interference to the wire. In conclusion, the leakage magnetic field produced by the linear motor is the main interference source of the LCD screen malfunction.

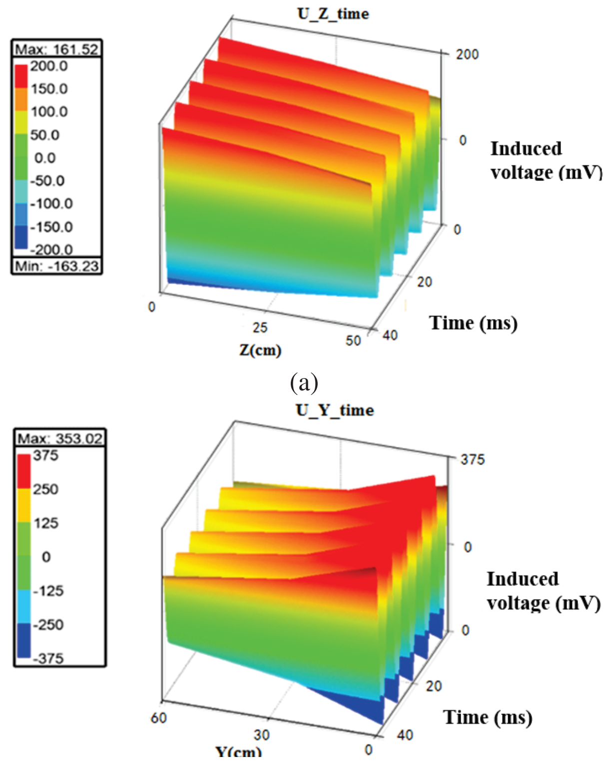

(a)

(b)

Fig. 9. Diagram of the variation of induced voltage with distance from the linear motor: (a) diagram of the variation of induced voltage with Z-axis distance and (b) diagram of the variation of induced voltage with Y-axis distance.

C. Analysis of the interference coupling mechanism

A simple model of an LCD screen and the linear motor of a low-medium speed maglev train is presented in Fig. 10. There are two LCD screens in one carriage, located at points A and B. There are five linear motors on each side, which convert DC 1500 V into three-phase AC power via the traction converter.

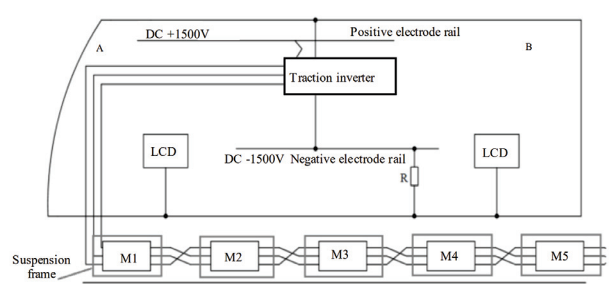

Fig. 10. Simplified diagram of an LCD screen and a linear motor.

The secondary of the linear motor of the maglev train is wider than the primary, leading to the phenomenon of magnetic flux diffusion on the upper and lower sides and resulting in alteration of the air gap magnetic field. Since the train LCD screen control system cable is mainly longitudinally wired along the bottom of the car, when the linear motor passes through a large current, the magnetic field will influence the closed circuit composed of the adjacent equipment. Hence, the horizontal end effect of the linear motor of the maglev train is the main interference factor causing a malfunction of the LCD screen.

When a large current passes through the linear motor, the magnetic field generated by the lateral end effect will induce a magnetic flux in the circuit consisting of the LCD screen and the control system located 650 mm away from the linear motor. This will subsequently generate an induced voltage at the LCD screen port. The induced voltage will cause the ground potential of the LCD screen housing to rise, resulting in a fault. The inductive coupling model of the LCD display subjected to linear motor EMI is presented in Fig. 11. The device on the left is the casing of the LCD display, and Z_S represents its equivalent impedance. The device on the right is the casing of the LCD screen control system, and Z_L represents its equivalent impedance.

These two devices are connected by cables laid under the train, forming a common grounding circuit that is 8 m long and 0.4 m wide. The induced voltage U_N generated by the magnetic field of the linear motor in the closed circuit of the LCD screen control system is:

$$U_{\mathrm{N}} = -\frac{d}{d_t}\int_S \boldsymbol{B} d\boldsymbol{S}, \tag{8}$$

where $\boldsymbol{B}$ is the magnetic induction intensity of a linear motor and $\boldsymbol{S}$ is the area of a closed circuit.

A simulation model of the magnetic field generated by the combined action of five linear motors passing through the circuit consisting of the LCD screen and the control system is depicted in Fig. 12. The length of the linear motors is approximately 10 m, the length of the closed circuit is about 8 m, and the width is nearly 0.4 m. The simulation result of the magnetic field strength of one of the linear motors is shown in Fig. 13.

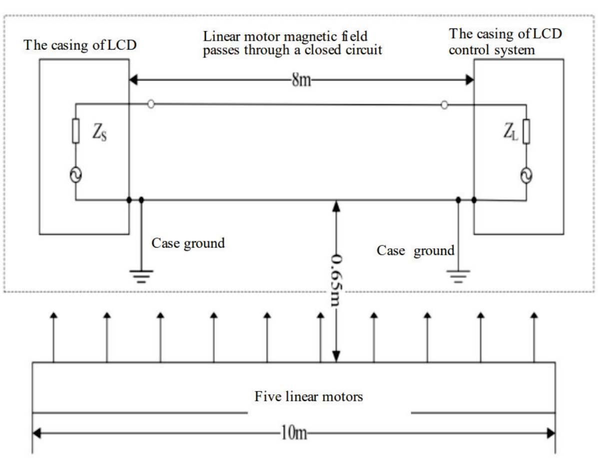

Fig. 11. Schematic diagram of an LCD screen affected by the EMI of a linear motor.

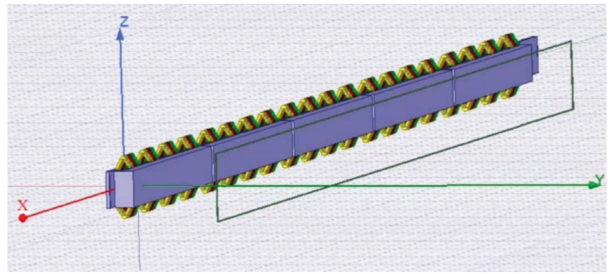

Fig. 12. Simulation model of linear motor and closed circuit.

As depicted in Fig. 13, the magnetic field strength between the primary winding of the linear motor and the secondary aluminum plate is extremely high, attaining 1.026×10^5 A/m, which generates the driving force to propel the train. When five linear motors operate concurrently, the leakage magnetic field resulting from the lateral end effect induces voltage within the closed circuit formed by the LCD screen casing and the control system, illustrated in Fig. 14.

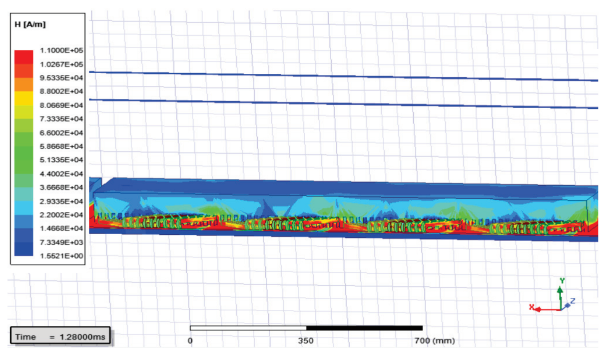

Fig. 13. Simulation diagram of magnetic field strength.

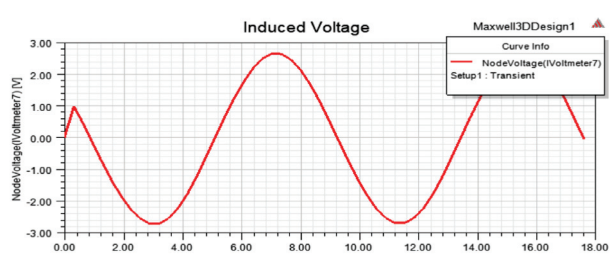

Fig. 14. Graph of induced voltage on a closed circuit.

Based on simulation outcomes, the peak value of the induced voltage produced by the magnetic field resulting from the joint operation of five linear motors within a closed circuit is approximately 2.7 V.

The connection cable between the LCD screen and the control system is arranged along the card slot at the bottom of the train. The card slot is fabricated from steel material with a shielding coefficient k of 0.45 [21]. Therefore, based on the actual situation, the induced voltage U of the closed circuit should be corrected to:

$$U = k \bullet U_{\mathrm{N}} \tag{9}$$

After correction, the peak value of the induced voltage U generated by the magnetic field of the five linear motors acting together on the closed circuit is about 1.215 V. Therefore, the grounding potential of the LCD screen is raised by 1.215 V by simulation calculation.

A digital oscilloscope model GDS-2302A is used to measure the ground voltage of the LCD screen housing on site. The average speed of the train was 100 km/h and the effective value of phase current flowing in the motor was 300 A during the measurements. The test results are shown in Fig. 15. The test results show that peak voltage is below 1.4 V. The induced voltage value calculated by simulation is very close to the actual measured value. It further indicates that the malfunction on the LCD screen is mainly caused by the leakage magnetic field generated by the transverse end effect of the linear motors.

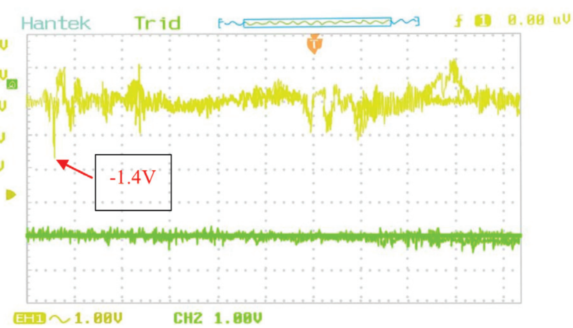

Fig. 15. Interference waveform of an LCD screen.

IV. RESEARCH ON SOLUTIONS TO MALFUNCTIONS

In order to solve the fault of the LCD screen caused by the unbalanced grounding potential of the LCD screen casing, this paper uses TVS diodes to suspend the grounding of the LCD screen. Its working principle is that when the circuit is running normally, the TVS is in a high impedance state and does not affect normal operation of the LCD screen. When an abnormal overvoltage emerges in the circuit and attains breakdown voltage, the TVS quickly switches from the off state to the on state. This provides a conductive path for instantaneous current, while also controlling overvoltage within a safe range (within normal operating voltage and maximum clamp voltage), thus protecting the circuit of the equipment. When the abnormal overvoltage vanishes, the TVS returns to the cutoff state.

The maximum voltage for the operation of the LCD screen is 22 V. Consequently, the TVS diode model P6KE24A is chosen, which has a reverse breakdown voltage of 25 V and a maximum clamping voltage of 33 V. Because the EMI encountered by LCD displays is AC interference, it is necessary to connect two TVS diodes in opposite directions in series to suspend the grounding of LCD screen.

As depicted in Fig. 16, two P6KE24A TVS diodes are connected in series at the signal grounding screw hole of the LCD display screen. The TVS diode is connected to the LCD screen casing through a signal grounding screw and suspended for grounding. Subsequently, an

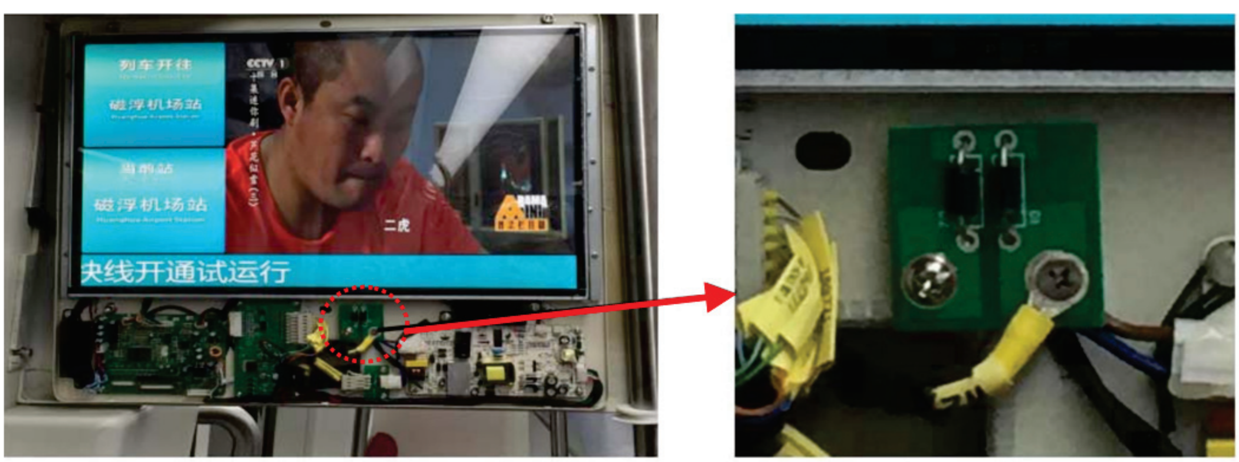

Fig. 16. Implementation diagram of suppression measures.

oscilloscope is used to measure the ground voltage of the LCD screen housing on site, and the test results are shown in Fig. 17.

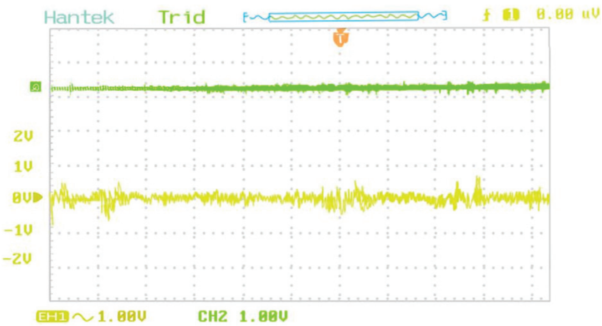

Fig. 17. Interference waveform of the LCD screen after adding suppression measures.

Comparing Figs. 15 and 17, it can be seen that the induced voltage is significantly suppressed after the TVS diode is connected in series. After using this method, the malfunction of the LCD screen disappeared.

V. CONCLUSION

The malfunction of an LCD screen on a low-medium speed maglev train is studied in this paper. The conclusions are as follows:

(1) The leakage magnetic field generated by the end winding of the linear motor is the cause of LCD screen failure.

(2) The leaked magnetic field will generate induced voltage in the closed circuit connected between the LCD screen and the control system by inductive coupling, thereby generating EMI on it.

(3) The technique of utilizing two TVS diodes in series to suspend and ground the LCD display screen is an effective method for suppressing EMI.

ACKNOWLEDGMENT

The authors would like to thank the editors and anonymous reviewers for their insightful comments. This paper is supported by the Natural Science Foundation of Sichuan, China (NO. 2024NSFSC0866) and the Fundamental Research Funds for the Central Universities (No. PHD2023-005).

REFERENCES

[1] S. Niska, "A major source of faults in Swedish railway," *International Journal of Perform Ability Engineering Electromagnetic Interference*, vol. 5, no. 2, pp. 187-196, 2009.

[2] H. Wang and W. Xue, "Development and application of the railway transportation management information system," *Applied Mechanics and Materials*, vol. 26, no. 1, pp. 1848-1851, 2013.

[3] J. Hu, "Analysis of characteristics of traction power supply system for medium and low speed maglev vehicles," *Electric Locomotives & Mass Transit Vehicles*, vol. 26, no. 4, pp. 33-34, 2003.

[4] B. Tellini, M. Macucci, and R. Giannetti, "Conducted and radiated interference measurements in the line-pantograph system," *IEEE Transactions on Instrumentation and Measurement*, vol. 50, no. 6, pp. 1661-1664, 2001.

[5] Y. Tang, F. Zhu, H. Lu, and X. Li, "Analysis and suppression of EMI for traction control unit speed sensors of CRH380BL electric multiple unit," *Applied Computational Electromagnetics Society Journal*, vol. 33, no. 5, pp. 553-560, 2018.

[6] Y. Wu, "Test and research on electromagnetic interference of maglev vehicle," *Railway Signaling & Communication*, vol. 44, no. 2, pp. 24-26, Feb. 2008.

[7] B. Wei, K. Yu, and Y. Duan, "Study on the electromagnetic interference of low medium speed maglev on high speed railway GSM-R communication," *Railway Signaling & Communication*, vol. 51, no. 7, pp. 48-52, 2015.

[8] H. Qi, "Analysis of electromagnetic environment in the operation of middle and low speed maglev vehicle," *Electric Drive for Locomotives*, pp. 62-65, May 2012.

[9] G. Yang and Z. Zhao, "Comparative study on several typical rail transit operation control systems," *Journal of the China Railway Society*, vol. 31, no. 1, pp. 82-87, 2009.

[10] Y. Chen and X. Tian, "The development of the linear induction motor," *IEEE Transactions on Newcomen Society*, vol. 67, no. 1, pp. 185-205, 2014.

[11] W. Xu, "System-level efficiency optimization of a linear induction motor drive system," *IEEE Transactions on Electrical Machines and Systems*, vol. 3, no. 3, pp. 285-291, 2019.

[12] R. Luo, J. Wu, and Z. Li, "Research on the electromagnetic interference of the environment space where the levitation gap sensor of the medium and low speed maglev vehicle is located," *Instrument Technique and Sensor*, vol. 67, no. 1, pp. 1-6, Nov. 2018.

[13] J. Ding, X. Yang, and Z. Long, "Structure and control design of levitation electromagnet for electromagnetic suspension medium speed maglev vehicle," *IEEE Transactions on Vibration and Control*, vol. 25, no. 6, pp. 1179-1193, 2019.

[14] W. Zheng, W. Hu, and L. Zhou, "Design of passenger information system suitable for medium and low speed maglev vehicle," *Electric Locomotives & Mass Transit Vehicles*, vol. 37, no. 2, pp. 22-25, 2014.

[15] Z. Liang, J. Zhu, and J. Zhang, "Research and improvement of green TFT-LCD," *Chinese Journal of Liquid Crystals and Displays*, vol. 34, no. 4, pp. 354-360, 2019.

[16] M. Chen and F. Zhou, "The design and implementation of a low cost 360-degree color LCD display system," *IEEE Transactions on Consumer Electronics*, vol. 37, no. 2, pp. 735-739, 2011.

[17] S. Kim and H. Choi, "Application of cascode level shifter for EMI reduction in LCD driver IC," *IEEE Transactions on Electronics Newsweekly*, vol. 3, no. 1, pp. 321-325, 2015.

[18] L. Su, X. Yang, and X. Li, "Research on the mechanism and improvement of high-temperature reliability crosstalk of automotive TFT-LCD devices," *Journal of Optoelectronics*, vol. 39, no. 2, pp. 123-126, 2019.

[19] Z. Hu and Y. Wu, "Environmental impact analysis and protective measures of Harbin rail transit phase project," *Journal of Environmental Science and Management*, vol. 32, no. 8, pp. 81-84, 2007.

[20] Y. Chen, "Typical electromagnetic interference of vehicle PIS system coupling mechanism and suppression study," M.S. thesis, Southwest Jiaotong University, Chengdu, China, 2021 [in Chinese].

[21] TB/T 1678-1997, *Railway Industry Standard of the People's Republic of China: Professional Terminology for Communication Protection of AC Electrified Railway*. Beijing: China Railway Press, 1997.

Yutao Tang was born in Sichuan Province, China, in 1991. She received the Ph.D. degree in electrical engineering at Southwest Jiaotong University, Chengdu, China, in 2021. She is currently a Lecturer in the Institute of Electronic and Electrical Engineering, Civil Aviation Flight University of China. Her research interests include electromagnetic environment test and evaluation, and electromagnetic compatibility analysis and design.

Xin Li received the Ph.D. degree in electrical engineering from Southwest Jiaotong University, Chengdu, China.

He is currently a research associate in the Civil Aviation Flight University of China, Chengdu, China. His current research interests include electromagnetic compatibility analysis, evaluation, transmission line analysis, rail traffic, civil unmanned aerial vehicles, and navigation technology research.

Chao Zhou was born in AnHui, Province, China, in 1980. He received his Ph.D. degree from University of Electronic Science and Technology of China in 2013. He is working in Civil Aviation Flight University of China, where he is currently a professor, deputy dean of the Institute of Electronic and Electrical Engineering, master tutor, and head of the UAV team. His current research interests include civil unmanned aerial vehicles and civil aviation electromagnetic environment effects.